SAPIENZA
UNIVERSITÀ DI ROMA

Synthesis and characterization of short peptide-based hydrogel composites for antibacterial and environmental applications

Faculty of Mathematics, Physics, and Natural Sciences
Department of Chemistry Ph.D. in Chemical Sciences – XXXVII Cycle

Roya Binaymotlagh
ID number 2026492

Supervisor
Prof. Cleofe Palocci

Ph.D. Coordinator
Prof. Paola D'Angelo

A thesis submitted in partial fulfillment of the requirements for the degree of Doctor of Philosophy in Chemical Sciences

January 2025

Synthesis and characterization of short peptide-based hydrogel composites for antibacterial and environmental applications
Ph.D. thesis. Sapienza – University of Rome

Author's email: roya.binaymotlagh@uniroma1.it

This page is intentionally left blank

Abstract

Peptide-based hydrogels have attracted increasing attention for biological applications and diagnostic research due to their impressive features including biocompatibility and biodegradability, injectability, mechanical stability, high water absorption capacity, and tissue-like elasticity. Furthermore, peptide hydrogels can be used as carriers in drug and gene delivery since, given their porous structure, they allow the entrapment of different molecules (such as drugs, nucleic acids and metal nanoparticles) with antibacterial activity. Nanoparticles in the hydrogel are normally used as nanofillers and nano crosslinkers. In order to obtain hydrogel nanocomposites, a variety of organic or inorganic nanoparticles known as nanofillers are mixed in the hydrogel matrix, and this results in very high enhancement of both internal and external properties of the conventional hydrogel matrix. The combination of organic/inorganic components in the hydrogle network lead to extremely modified chemical and physical, biological, swelling, and releasing properties.

In this Ph.D. thesis, we developed a hydrogel by the self-assembly of a short peptidic sequence, the hydrogelator Fmoc-Phe_3, enzymatically synthesized in water by a lipolytic enzyme, starting from L-Phenylalanyl-L-phenylalanine (Phe_2) and an N-(9-Fluorenylmethoxycarbonyl)-L-phenylalanine (Fmoc-Phe). The formed tripeptide molecules (Fmoc-Phe_3) self-assemble in water into a three-dimensional fibrous structure. We focused our attention on the synthesis and characterization of novel peptide-based hydrogel composites containing metal and metal oxide nanoparticles such as silver (Ag), titania (TiO_2), and magnetic (γ-Fe_2O_3) NPs, due to their potential antibacterial and environmental applications. On this basis we employed silver salts to develop an *in situ* one-pot approach for preparing AgNPs inside of the peptide hydrogels using a photochemical synthesis, without any toxic reducing agents. In this study the effect of "green" reducing agents as honey on both the mechanical stability of the hydrogel composite and as capping agent for the AgNPs was investigated. The structure and morphology of the nanohybrids were characterized with different techniques such as FESEM, UV-Vis, DLS, SAXS, and XPS. Moreover, the antibacterial properties of these composites were investigated on a laboratory strain and a clinical isolate of *Staphylococcus aureus*. Results demonstrated that honey increased both the swelling ability and mechanical stability of the hydrogel. In addition, those hydrogel composites containing honey showed monodispersed AgNPs. Finally, a higher antibacterial effect of AgNPs in the hybrid was observed in the presence of honey.

Regarding titania nanoparticles (TiO_2NPs), we used commercial ones in the anatase phase and impregnated the peptide hydrogels with them. Two different concentrations of NPs were hired to see the effect of concentration on different parameters of the peptide hydrogel such as toughness and swelling abilities. In addition, the effect of ultrasound waves on the dispersion of the NPs inside of the peptide hydrogels, along with its effect on the synthesized composite like mechanical stability and water absorbance was studied. The results demonstrated that increasing the concentration of the NPs along with the sonication can increase the mechanical stability of the hydrogel significantly but the swelling ability obeys the reverse trend, which may be related to the cross-section caused by the NPs. The antibacterial tests against laboratory *Staphylococcus aureus* strain and two Methicillin-Resistant *S. aureus* (MRSA) clinical isolates demonstrated that after encapsulation of the NPs inside of the hydrogels, their toxicity increased significantly in the presence and absence of UV light.

Maghemite NPs modified with Polyacrylic acid (γ-Fe_2O_3@PAA), were synthesized successfully and characterized using various techniques such as FESEM, UV-Vis, DLS, TEM, and XPS. The results showed that PAA can increase both the monodispersity of the NPs and their stability. After impregnation of peptide hydrogels with γ-Fe_2O_3@PAA NPs, their environmental application for the adsorption of heavy metal ions like Cr(III), Ni(II), and Co(II) and some dyes such as methyl orange (MO), methylene blue (MB), and rhodamine 6G (Rh6G) was studied. The results of the removal studies demonstrate that the encapsulation of γ-Fe_2O_3NPs in peptide hydrogels in the presence of an external magnetic field increases the adsorption efficiency of the hydrogel matrix for the metal ions and desired dyes tested in this study by more than 50% for each.

Table of contents

List of abbreviations

The following table describes the significance of various abbreviations and acronyms used throughout the thesis. Standard acronyms used once in the text are not in this list.

Abbreviation	Meaning
AgNPs	Silver nanoparticles
AgNPs-SDS	Silver nanoparticles coated with sodium dodecyl sulfate
AgNPs-3MPS	Silver nanoparticles coated with 3MPS
AgNPs/hgel	Silver nanoparticles impregnated in hydrogel
AgNPs/hgel-honey	Silver nanoparticles impregnated in hydrogel
ATR	Attenuated total reflectance
DLS	Dynamic light scattering
EDS	Energy dispersive X-ray spectroscopy
FESEM	Field emission scanning electron microscopy
FT-IR	Fourier transform infrared
γ-Fe_2O_3NPs	γ-Fe_2O_3-polyacrylic acid (PAA) nanoparticles
Fmoc-Phe	(Fluorenylmethoxycarbonyl-phenylalanine)
γ-Fe_2O_3NPs@HG	γ-Fe_2O_3NPs embedded in peptide hydrogel
hgel	Hydrogel
hgel/AgNPs-SDS	Hydrogel impregnated with AgNPs-SDS
hgel/AgNPs-3MPS	Hydrogel impregnated with AgNPs-3MPS
hgel-TiO_2NPs	Hydrogel impregnated with TiO_2NPs
HG	Fmoc-Phe_3 hydrogel
ICP-AES	Inductively coupled plasma-atomic emission spectrometer
MB	Methylene blue
MO	Methyl oragne
3MPS	3-Mercapto-1-propanesulfonate
MNPs	Magnetic nanoparticles
MRSA	Methicillin-resistance *s. aureus*
MIC	Minimum inhibitory concentration
NPs	Nanoparticles
$NaBH_4$	Sodium borohydride
Phe2	Phenylalanine dipeptide
PAA	Polyacrylic acid
Rh6G	Rhodamine 6G
SAXS	Small-angle X-ray scattering (SAXS)
S. aureus	*Staphylococcus aureus*
SDS	Sodium dodecyl sulfate
TiO_2NPs	Titanium(IV) dioxide nanoparticles
XPS	X-ray photoelectron spectroscopy

1. Introduction

1.1. Hydrogels, properties, and their classification

Hydrogels are a class of interesting biomaterials exhibiting unique structures and properties and a very high potential for medical, therapeutic, and diagnostic applications[1]. The term hydrogel appeared first in the literature in 1896 by Bemmelen. These biomaterials consist of two components: a solid phase and a liquid phase, *i.e.* water. The solid phase is generally a polymeric network or a supramolecular structure given by the self-assembly of less complex structures. The liquid phase (water) is trapped in the meshes of the three-dimensional solid phase network. Its amount can reach 99% of the weight of the entire material[2]. A schematic representation of the hydrogel mesh structure is shown in **Figure 1.1**[3].

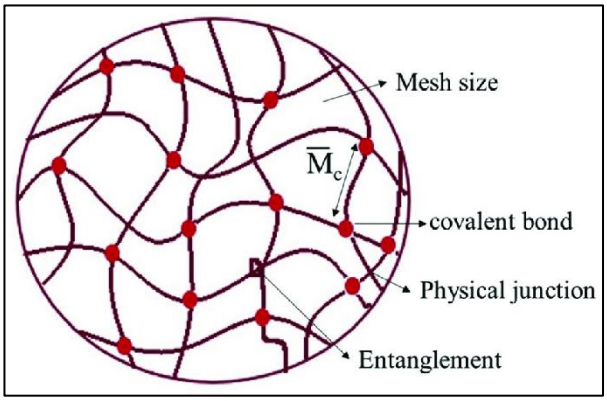

Figure 1.1. Structure of a hydrogel at molecular level[3].

Hydrogels can be classified according to the nature of the cross-links present in the three-dimensional lattice[4].

1. physical, weak, reversible bonds (entanglement between chains, physical interactions such as hydrogen bonds, ionic interactions, Van der Waals forces, hydrophobic interactions, π-π aromatic stacking); which are reversible and can be altered by environmental (physical) changes (e.g., temperature) or chemical changes (e.g. pH) and do not produce any modification in the chemical structure[5,6]. Some natural polymers capable of forming physical hydrogels are proteins, such as collagen and gelatin, and polysaccharides, such as alginate and agarose[7]. Self-assembling hydrogels belong to the group of physical hydrogels[8].

2. Covalent, irreversible bonds present in chemical hydrogels. Crosslinking can be achieved by adding crosslinking agents. In this case, the resulting material has excellent mechanical properties

and good stability[9]. The use of chemical hydrogels in biomedical applications is hampered by the use of toxic cross-linkers during their preparation and by the reduced possibility of manipulating them. In **Figure 1.2** different classification criteria of the hydrogels are represented[10].

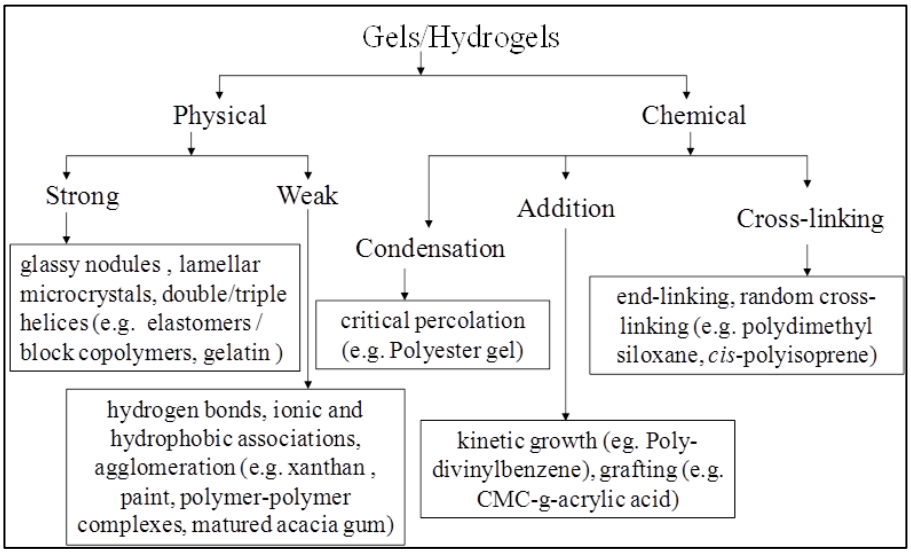

Figure 1.2. Classification of the hydrogels[10].

An interesting class of hydrogels consists of those based on peptides, which are biological macromolecules composed of amino acids covalently linked together by peptide bonds[11]. Self-assembling peptides are a particular class of molecules characterized by the ability to spontaneously organize themselves into ordered and stable structures, in conditions of thermodynamic equilibrium, thanks to the formation of non-covalent bonds (hydrogen bonds, ionic bonds, hydrophobic interactions, Van der Waals forces) between the side chains of the amino acids of which they are composed[12]. These intra- and inter-molecular interactions allow the peptide to organize itself into secondary (α-helix and β-sheet) and tertiary (fibers and fibrils) structures[13]. The self-assembly process is based on the interaction of pre-existing components (parts of a disordered system), which, under certain conditions, create a new complex (ordered) structure. **Figure 1.3** shows the process by which peptide hydrogelators self-assemble to form the fibrous network of the hydrogel[14].

Self-assembly is due to both the nature of the individual amino acids and their position in the sequence. It is therefore possible to obtain a certain secondary structure by choosing and suitably arranging the amino acids. Furthermore, self-assembly depends on various factors external to the intrinsic structure of peptides, such as pH, time, temperature, and concentration[15]. Interest in these peptides has increased due to their capacity to self-aggregate into aqueous solution, which allows it to form 2D and 3D structures (the hydrogels). In recent years, the possibility of obtaining stable hydrogels using short peptides has emerged with molecular weight (short peptides). These, when

found in water under specific conditions pH, and temperature, can act as hydrogelators[16,8]. They self-assemble into supramolecular structures, such as nanofibres, which, thanks to physical entanglements, give rise to the lattice, which constitutes the solid phase of hydrogels. During this process, the water is trapped inside the mesh of the 3D network.

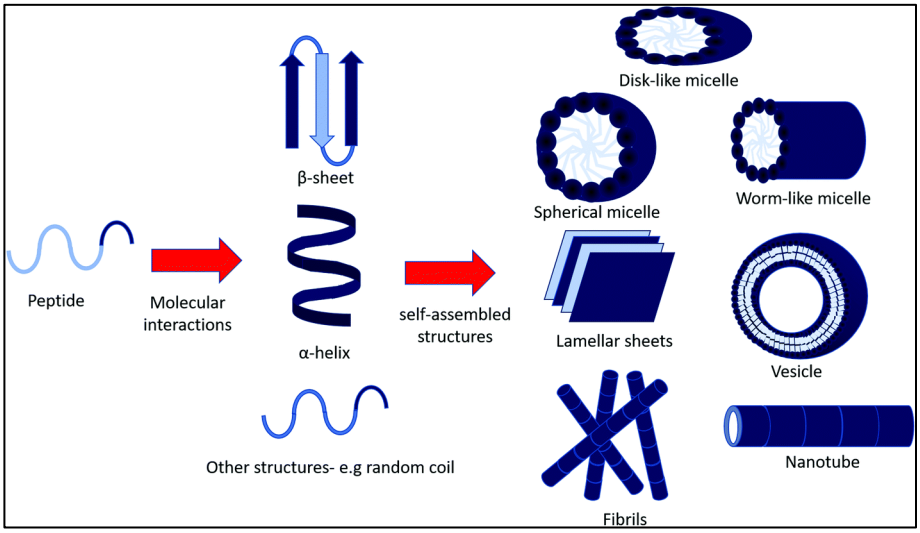

Figure 1.3. Self-assembly process of peptide hydrogelators[14].

It recently was found that using self-assembling short peptides with an aromatic moiety in the chain lateral generates more stable hydrogels with a denser fibrillar network[164]. This is due to interactions of π-π stacking which are formed between the aromatic side chains of the peptides and which they therefore stabilize the secondary structure[166]. Hence, the amino acid phenylalanine (Phe) and tyrosine (Tyr), which have benzyl and phenyl groups in the side chain, are good candidates for making stable hydrogels.

It has been verified that the Fluorenyl-methoxycarboxylic group (Fmoc), used as a protecting agent for -NH_2 in the amino acids during the synthesis of the hydrogel, thus contributing to the formation of physical bonds in the gel texture[165,166]. The Fmoc group (**Figure 1.4**) contains aromatic rings that give π-π stacking with other aromatic rings present in the system. This positively affects the self-assembly of peptide hydrogels[17].

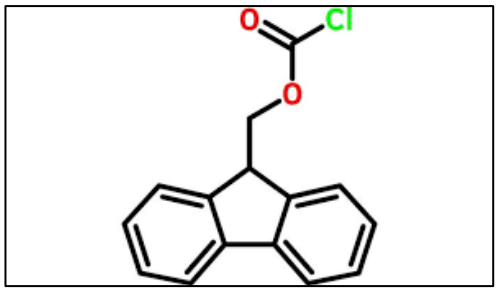

Figure 1.4. Structure of Fluorenyl-methoxycarbonyl chloride (Fmoc-Cl)[17].

An interesting approach for the synthesis of self-assembling hydrogelators involves the use of lipolytic enzymes (lipases) of microbial origin, enzymes capable of catalyzing the formation of the peptide bond between the substrates[18,19,20].

Lipases are enzymes belonging to the enzymatic class of the triacylglycerol hydrolases (EC 3.1.1.3). In nature, lipases hydrolyze the ester bonds in triglycerides in fatty acids, diglycerides, monoglycerides, and glycerol working on the interface between the aqueous phase, where the enzyme is soluble, and the lipidic phase of the substrate[21]. All lipase, regardless of the organism, have the same structural element, a central β sheet given by parallel filaments alternating with an α helix. This structure is known as α/β hydrolase fold[22].

In the active site, there is the catalytic triad, which is well preserved in most lipolytic enzyme families, of which the amino acid composition is known. The amino acid order in the catalytic triad is Ser-Asp-His, where serine is the essential nucleophilic residue for catalysis[23].

Some lipases present the catalytic site covered by a superficial handle known as a "flap" or "lid". The lid can have two conformations: closed and open. In the closed conformation, the lid makes the active site inaccessible for every substrate. The lid rotation leads to the open conformation and makes it accessible to the substrate of the active site[173].

Lipases are enzymes very diffused and some of their catalytic properties depend on the microorganism which they come from. Lipases from microorganisms are generally highly employed in biocatalysis because they are easily purified and present a low substrate specificity. An organism that produces thermostable extracellular lipases and proteases is the bacterium *Pseudomonas fluorescens*[171]. In particular the high conformational stability makes these lipases good candidates to catalyze reactions for biotechnological applications.

Peptide hydrogels are often used for applications in the biomedical sector due to their biocompatibility, biodegradability and ability to give rise to biomimetic structures (i.e. capable of mimicking some properties of extracellular matrices)[24]. Furthermore, the self-assembly eliminates the use of toxic chemical cross-linking agents during the preparation phase to allow the system to gel[152]. Hydrogels are used in various fields of regenerative medicine thanks above all to their ability to trap water, which makes them, in some ways, very similar to human tissue[25]. Precisely for this reason, they are widely used in tissue engineering[176]. Thanks to the ease of realization of hydrogels and the possibility of modifying their structure, it is possible to create scaffolds with specific physical and chemical properties based on the type of application required. Furthermore, hydrogels can be used as carriers in drug and gene delivery, since, given their porous structure, they allow the trapping inside of bioactive molecules (such as drugs, nucleic acids, and metal nanoparticles with antibacterial activity)[164,26].

The diffusion coefficient of the trapped drug depends on the porosity of the hydrogel, i.e. on the size of the meshes and the degree of cross-linking: larger mesh sizes allow a more rapid diffusion of the molecules present inside them (**Figure 1.5**). By modulating the structure of the hydrogel, drug release can be controlled[27].

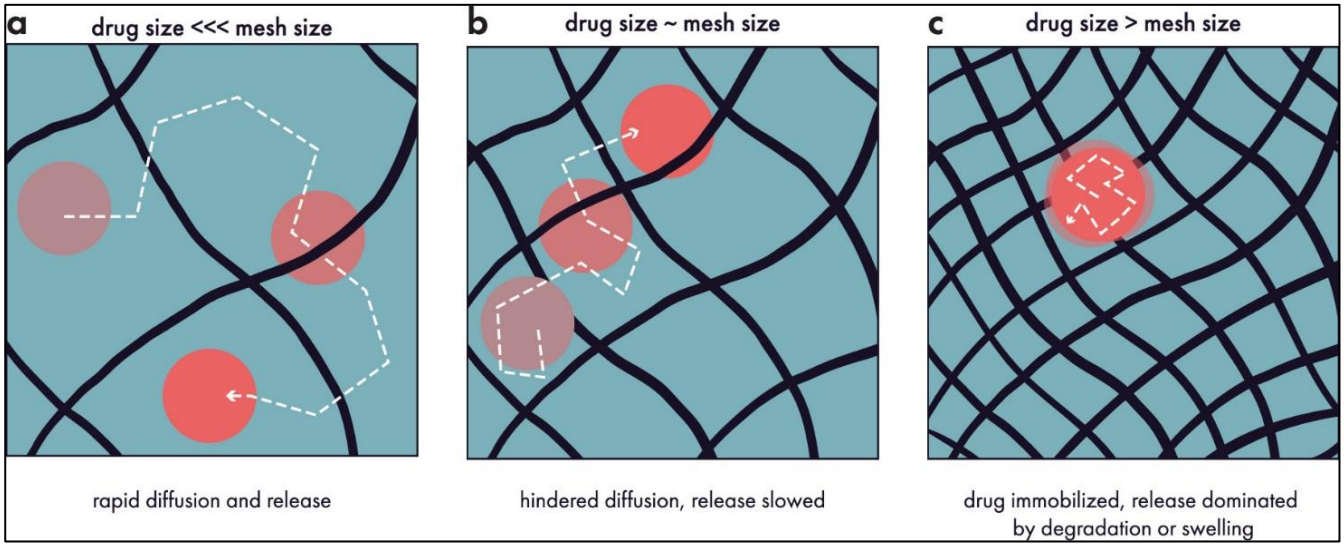

Figure 1.5. Diffusion of the drug from the hydrogel as a function of the mesh size of the lattice[27].

1.2. Nanoscience and nanotechnology

Nanoscience involves studying materials at the atomic, molecular, and macromolecular scales. It is a highly multidisciplinary science that arises from the combination of quantum mechanics, supramolecular chemistry, materials science, and molecular biology[28].

Nanotechnology is a branch of applied science and technology that relies on notions and methods deriving from nanoscience for the design, synthesis, characterization and application of nanoscale materials[29]. The first reference to nanotechnologies, dates back to 1959, when the American physicist Richard P. Feyman, in his speech remembered as "There's plenty of space at the bottom", made considerations about the possibility of building machines at the molecular level and directly manipulating matter at the atomic scale[30].

The charm of nanotechnologies lies in the fact that, in the passage from the macroscopic to the nanoscopic universe, the chemical-physical, optical, electronic and magnetic properties change. In this way, it is possible to manufacture materials and systems with completely new properties compared to those relating both to massive substances and to isolated molecules or atoms. This change is because nanostructured materials, compared to macroscopic ones, have a high percentage of surface atoms, which strongly influence their characteristics and behaviors[31].

Nanoparticles (NPs) are colloidal particles formed by atomic or molecular aggregates with dimensions in the order of nanometers (1-100 nm)[32]. Their small size allows them to exhibit new and significantly improved physical, chemical, and biological properties. Two types of approaches for the synthesis of nanomaterials can be distinguished:

1. Top-down approach: reducing the dimensions of structures down to the nanometric scale using physical methods;

2. Bottom-up approach: using small components, normally molecules or their aggregates, as "building blocks" and controlling their assembly to create nanomaterials. These techniques are based on the nucleation and subsequent growth of nanostructures[5].

Currently, the Top-down techniques are the most consolidated, while the Bottom-up, to which they are associated with the higher expectations, are still in the development stage. In terms of chemical composition they can be divided into:

1. Nanoparticles of an organic nature: polymers, liposomes, micelles, dendrimers, nanotubes carbon.

2. Inorganic nanoparticles: metallic (eg gold or silver), based on metal oxides, silica, semiconductor materials (quantum dots), magnetic. **Figure 1.6** shows different types of nanoparticles.

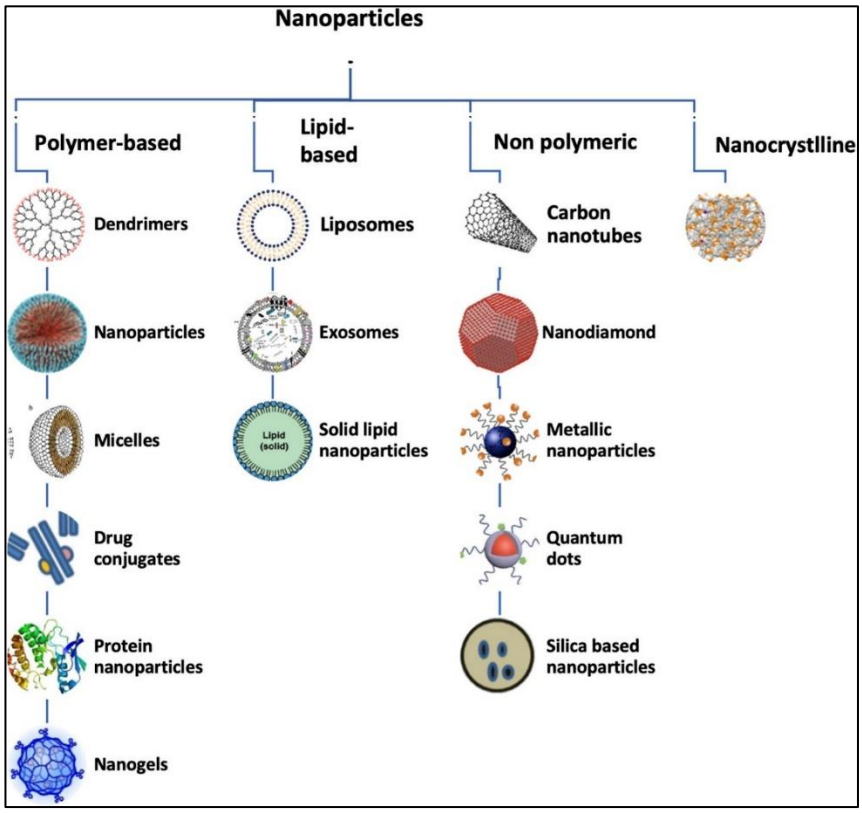

Figure 1.6. Different types of nanoparticles[33].

These nanostructures can exhibit different morphologies, such as nanospheres, nanorods, nanotubes and nanofilms. Furthermore, the surface can be functionalized with specific ligands, which increases its versatility[6].

Some of the countless current or potential applications of nanotechnology in science and technology are illustrated below.

1. Textile industry

Fabricating of fabrics containing nano-sized particles or fibers allows for improved properties without a significant increase in weight, thickness, or stiffness. Some examples of the application of nanomaterials in this field are the use of nano-fibers to make water-resistant trousers and stainless materials or the use of silver nanoparticles with a bactericidal action to make anti-odor clothing[34].

2. Environment

The use of nanostructured catalysts allows the transformation of a greater quantity of chemical substances simultaneously, as they have a greater surface area to interact with them. This type of high-performance catalyst can be used to transform the polluting vapors that escape from cars or industrial plants into harmless gases, consequently improving air quality[35]. Furthermore, nanotechnologies are being exploited to reduce industrial water pollution. For example, nanoparticles through certain chemical reactions are able to convert contaminating substances and make them harmless[36].

3. Chemical sensors

Carbon nanotubes, zinc oxide nanowires or palladium nanoparticles can be used as sensing elements in nanotechnology sensors. The operating principle is based on the change of the electrical characteristics, such as resistance or capacity, of the sensitive element following the interaction with the substance to be measured by the sensor. Having a high surface area, nanosensors allow detecting even very low concentrations of the investigated substance[37].

4. Nanomedicine

Nanoparticles are particularly used in the biomedical sector as their dimensions are comparable to those of biological systems and this allows direct interaction with these systems[38]. In particular they are used in:

4.1. Diagnostics

Current in vitro diagnostic techniques present various criticalities, such as long analysis times, high costs, inaccurate results, the need to use complex instruments, and therefore to rely on specialized personnel. Such techniques, therefore, do not allow for a quick and easy point-of-care diagnosis[39].

The use of nanostructured materials in biosensors has recently attracted the attention of researchers thanks to their peculiar and advantageous properties. The high surface area to volume ratio of nanomaterials allows for greater interactions between the target and the sensor, making a more reliable sensing technique[40]. Furthermore, nano-sized materials have unique electrochemical, optical, and mechanical properties that help strengthen biological signaling and transduction mechanisms and enhance signal amplification[41,42,43]. Additional benefits include the ability to develop systems that are smaller in size, useful in point-of-care testing, improved accuracy and selectivity, the ability to use smaller sample quantities to obtain a response, and, in most cases, reduced maintenance costs[44,45]. Nanotechnology-based biosensors have recently found wide use for the detection of the Sars-CoV-2 virus. About in vivo diagnostics, nanoparticles are considered highly sensitive and reliable sensing agents, able to mark the site of disease (nanoimaging) and monitor the therapy process[46].

4.2. Antibacterial activities

Some nanoparticles, such as silver, and titania are toxic to bacteria and not to human cells, although their mechanism of action is not yet fully known. This application is currently very important, as bacterial resistance to antibiotics is a constantly growing phenomenon[8,47].

4.3. Drug delivery and gene delivery

The term Drug Delivery System (DDS) refers to the branch of pharmaceutical technology that deals with the encapsulation, transport, and release of drugs in a target site (organ or tissue). Nanomaterials have attracted enormous interest in this area in recent years[48,49,50]. The first DDS to use nanoparticles as drug carrier was developed in 1978 and consisted of a liposome[22]. Gene delivery, on the other hand, consists of the transport of exogenous genetic material (DNA or RNA). This must then be released into the host cell to allow it to induce gene expression[51].

Many advantages make nanocarriers very interesting in the delivery of bioactive molecules[52]:

1. Protection of the bioactive molecule contained in the nanoparticles from premature degradation;
2. Greater efficiency in reaching the target site;
3. Control of the release of the trapped bioactive molecule, by varying the pH conditions
4. Temperature of the surrounding medium;
5. Reduction of side effects, such as toxicity and the development of resistance to drugs, since nanoparticles allow a reduction for administered drug necessary for treatments;
6. Greater ability to bypass biological barriers thanks to their dimensions in the order of nanometres, favoring cellular uptake.

On the other hand, nanoparticles circulating in the bloodstream to the target site may undergo elimination by the Mononuclear Phagocytic System (MPS), also called the reticuloendothelial system (RES), before the target site is reached. To address the problem, nanoparticles can be functionalized with coating agents, such as PEG, resulting in better circulation times and an increase in the therapeutic efficiency of the drug[53]. Once the site of interest has been reached, the nanoparticles will be able to adhere to the target cells, penetrate inside them, and release the loaded substances.

The materials chosen for the construction of nanocarriers must meet certain requirements, such as biocompatibility, biodegradability (to avoid accumulation phenomena), non-toxicity, and stability. They also need to be cheap and easily available[54,27]. Currently, the research is focused on the modulation of the basic properties of nanoparticles, i.e. size, surface properties, and stability, to obtain an ideal transport system.

The main types of NPs used for the delivery of bioactive compounds are as follows:

1. Polymeric nanoparticles: thanks to the various advantages they possess, polymeric nanoparticles represent the most proposed nanocarriers for the conveyance and direction of bioactive molecules[55,56,57]. In fact, they are biodegradable, biocompatible, and versatile as they are able to trap a wide range of therapeutic agents[58]. Compared to other colloidal carriers, they have greater chemical-physical stability and a better ability to modulate the release[59].

2. Inorganic nanoparticles: Of all the NPs, inorganic NPs (quantum dots, metallic NPs, etc) are among those that are most abundantly produced and used commercially[60]. They are being used as therapeutic agents because of their anticancer and antimicrobial activities. They can be used to create antimicrobial nanocomposite films[61]. Silver, gold, zinc oxide (ZnO), and titanium oxide (TiO_2) NPs are the examples of inorganic nanoparticles whic can be used in cosmetics because of their excellent drug delivery system, skin whitening and moisture retention properties[62].

3. Liposomes: Liposomes are self-assembled (phospho)lipid-based drug vesicles that form a bilayer (uni-lamellar) and/or a concentric series of multiple bilayers (multilamellar) enclosing a central aqueous compartment[63]. Their similar nature to the human cell membrane makes them biocompatible and are the most used nanocarriers in drug delivery[64,65,66].

4. Dendrimers: they are macromolecules formed by monomeric or oligomeric units containing a series of ramifications, which extend from a central nucleus. The empty area present within the structure, the extent of the ramifications, the possibility of functionalizing the terminal groups, the ease of preparation and the control of the dimensions offer great potential for the delivery of drugs[67].

Other examples of application of nanoparticles are illustrated in **Figure 1.7**.

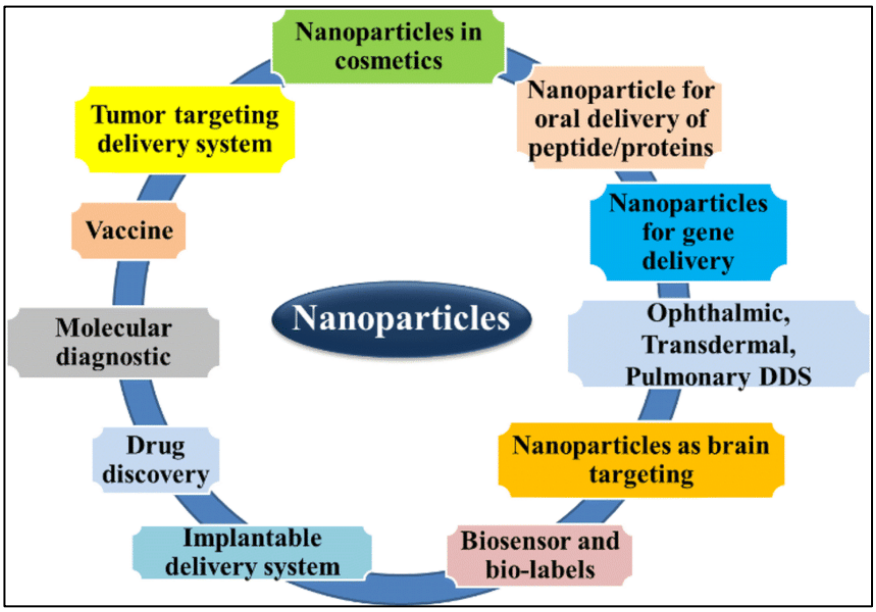

Figure 1.7. Present and future applications of nanoparticles[68].

1.3. Silver nanoparticles, synthesis, properties, and their applications

Silver nanoparticles (AgNPs) are among the most widely used nanostructured materials in the biomedical field thanks to the antibacterial properties of silver. This is usually used in the Ag^+ ionic form, as the $AgNO_3$ nitrate salt, to induce antimicrobial activity, but in recent years, research has shifted its focus to silver in the form of nanoparticles[69]. In fact, AgNPs are more reactive and therefore have a greater antibacterial activity as there is an increase in the surface available to be exposed to microbes (high surface/volume (S/V) ratio typical of nanomaterials)[70]. The antibacterial properties of AgNPs are influenced by various factors, among which there are the surface chemical characteristics, the size (as the size decreases, the S/V ratio increases and therefore the antibacterial properties improve), the concentration, the shape, the presence of capping agents, the state of agglomeration, the rate of dissolution, the reactivities in solution, the rate of ion release and the type of reducing agent used for their synthesis[71]. Furthermore, the antibacterial activity of AgNPs also depends on the type of microorganism against which they act and, specifically, on the thickness and composition of its cell wall[72,73].

Although silver nanoparticles have been shown to be effective against over 650 microorganisms, including Gram-positive bacteria (Bacillus, Clostridium and various Cocci), Gram-negative (Escherichia, Pseudomonas and Salmonella), fungi and viruses, the mechanism of action is not yet fully understood[74].

However, some mechanisms of antimicrobial action have been identified (**Figure 1.8**):[75,76,77]

1. AgNPs are able to adhere to the bacterial cell wall and induce a morphological variation of the membrane, which leads to an alteration of its permeability and transport mechanisms. This results in rupture of the cell wall. The adhesion process is due to the electrostatic attraction created between the positively charged AgNPs and the negatively charged cell membrane.

2. AgNPs are able to penetrate inside the cell, above all by endocytosis, and therefore to damage its intracellular structures, such as mitochondria, vacuoles, and ribosomes. Also, once in the cell:

3. They interact with DNA, altering its normal replication.

4. They deactivate vital enzymes of the bacterium, thanks to the interaction that is formed between Ag+ ions released by the AgNPs and the thiol, amine, and phosphate groups present in these enzymes (high affinity of the Ag^{+} for biomolecules).

5. Destabilize the enzymes of drug-resistant microorganisms, interfering with their ability to use oxygen for metabolic activities.

6. AgNPs induce the formation of free radicals (such as ROS) which are toxic to the bacterial cell they meet. The cell is subjected to oxidative stress, which causes damage to its membrane.

7. AgNPs affect the regulation of signal transduction in bacteria by dephosphorylation action on tyrosine residues. This action leads to the inhibition of transduction and subsequent growth arrest.

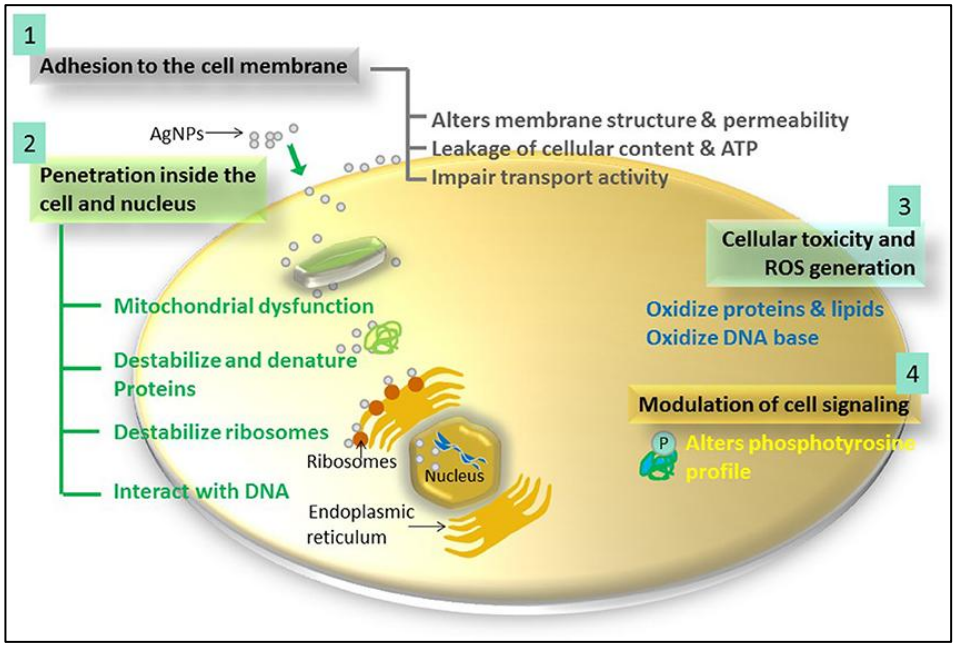

Figure 1.8. Representation of the four main mechanisms of antimicrobial action of AgNPs[78].

In addition to the mechanisms illustrated above, AgNPs are capable of modulating the immune system of humans through the induction of inflammatory responses that further inhibit microbial active.

The knowledge of the chemical reactions that take place on the surface of AgNPs and their interactions with the environment in which they are located has allowed us to better understand the mechanism of antibacterial action. Among the observed phenomena, there is aggregation, dissolution, redox photoreactions, and release or absorption of silver species and ions (**Figure 1.9**).

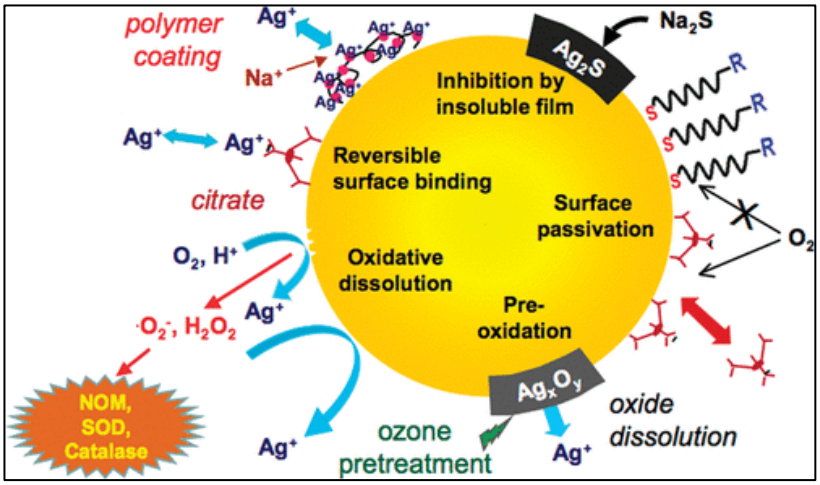

Figure 1.9. Reactions taking place on the surface of AgNPs[79].

It was understood that silver performs the real antibacterial action when it is in the form of Ag^+ ion (oxidation state = +1). Therefore, the AgNPs consisting of Metallic Ag have an antibacterial activity when they release Ag^+ ions in solution. Instead, the core of the nanoparticle, consisting of metallic Ag atoms with an oxidation state equal to zero, acts as a reservoir for the release of new Ag^+ ions.

Silver nanoparticles, are used in different sectors (**Figure 1.10**), such as in the biomedical, food, and other industrial fields, both in pure form and in combination with other materials thanks to their unique chemical-physical properties[80,81]. The applications of silver nanoparticles are innumerable; they are used in household products, for health, as antibacterial agents[82], in medical device coatings, in optical sensors[83,84], in the field of cosmetics, as anticancer agents[57], in the pharmaceutical and textile industries, in the diagnostics and orthopedics[85]. The most interesting applications are certainly those in the biomedical sector, in which the antibacterial, antifungal, antiviral, anti-inflammatory, antitumor, and antiangiogenic properties of AgNPs are exploited[86,87,88]. Silver-based nanomaterials are powerful tools used by nanomedicine to overcome the increasingly widespread problem of antibiotic resistance.

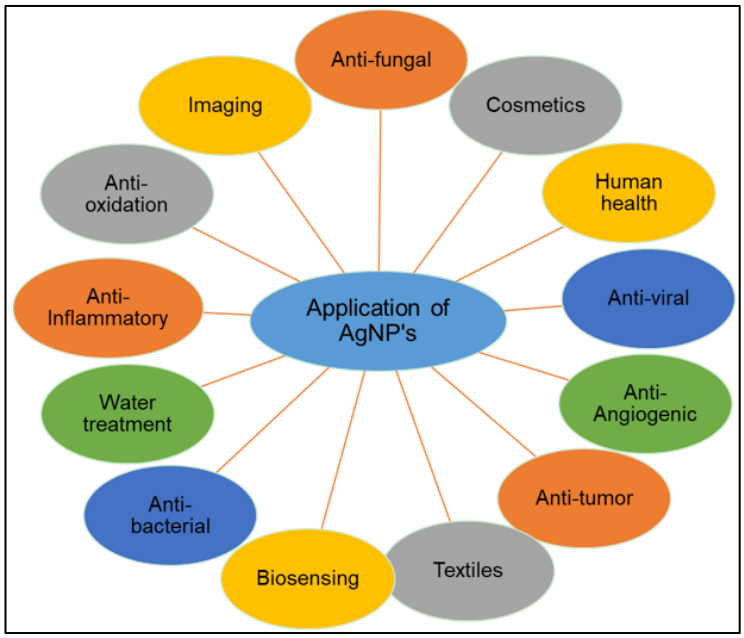

Figure 1.10. Some applications of AgNPs[89].

The synthesis of AgNPs can be achieved through conventional (physical and chemical) and innovative (biological) methods. Due to low efficiency of physical methods, such as laser ablation[90] and metallic evaporation[91], chemical synthesis is generally preferred[92]. The simplest method for the chemical synthesis of silver nanoparticles consists of the reduction in the liquid or organic phase of a silver precursor by a compound reducing agent, for example, sodium borohydride or sodium citrate. The three components required for the reaction are:

1. Metallic precursor (in this case $AgBF_4$ or $AgNO_3$);
2. Reducing agent (eg $NaBH_4$ or sodium citrate);

The major problems that could be encountered using physical and chemical methods for the synthesis of AgNPs are related to the high cost and the use of toxic chemicals that can represent a possible biological and environmental risk[93]. Furthermore, these nanoparticles can be used in the biomedical field and therefore must meet precise standards of final purity[68]. To overcome these problems, innovative methods of biological synthesis have been developed in recent years, which are more sustainable and less harmful to the individual and the environment[94]. These methods, compared to the chemical-physical ones, also allow a simpler control of the size, shape, and distribution of the silver nanoparticles obtained. For example, currently, some of the most widely used methods involve the use of bacteria, fungi, and plant extracts[95]. These are generally bottom-up approaches, in which reduction or oxidation reactions take place by microbial enzymes or photochemical components of plants[96].

The most accepted mechanism for the biosynthesis of AgNPs in vivo foresees in a first step the trapping of Ag^+ ions on the cell surface of microorganisms (fungi or bacteria), followed by the

reduction of Ag^+ to Ag^0 through the action of specific enzymes, such as nitrate reductase[97]. The reduction is NADPH-dependent and the nitrate is converted to nitrite by electron transfer to the silver ion (from Ag^+ to Ag^0). This synthetic mechanism has been observed in the bacterium *Bacillus licheniformis*[98] and in the fungus *Fusarium oxysporum*[99]. Compared to bacteria, fungi are able to produce higher quantities of AgNPs due to the synthesis of the higher amount of enzymes involved in this synthesis[100]. Finally, biological methods also include those that use microalgae, plants belonging to the class of chlorophytes, which in recent years have been increasingly used in science and technology[101]. Their use is advantageous, as they require mild conditions (light and water) for growth, have reduced growth times, and are capable of producing compounds that are useful on an industrial level. Therefore, recently, synthesis protocols of silver, gold, zinc, and iron nanoparticles have been developed which involve the use of microalgae[102].

Another approach that has recently been developing in the synthesis of silver nanoparticles involves the replacement of classic chemical reducing agents, such as $NaBH_4$, with simple sugars. Among these, those sugars with the greatest reducing activity are monosaccharides[103]. For sugar to have reducing activity, it must exist in an open chain form with an aldehyde or ketone group, in the case of an aldose or a ketone respectively. The reducing function is performed by the carbonyl group, which transfers the electrons to another species, for example to Ag^+, oxidizing itself in turn. Various works have been reported in the literature in which the reduction of silver salt takes place by carbohydrates, especially glucose, fructose, and lactose[104,105,106]. A very similar approach to using carbohydrates for a silver salt reduction involves the use of complex natural matrices containing reducing sugars, such as honey[20]. It is a complex water-based matrix containing about 200 substances, especially the monosaccharides fructose and glucose.

In addition to its traditional use in the food sector, honey has been widely used thanks to its therapeutic effects. For centuries, it has found application in the traditional medicine of the ancient Egyptian, Greek, and Indian populations. Currently, in modern medicine, honey is widely used especially for its antioxidant and antimicrobial power[82]. It is used in the production of medications for its ability to stimulate cytokines, in the treatment of viral infections (including those in the gastrointestinal tract), and in the treatment of ophthalmic disorders, such as conjunctivitis or corneal problems[107]. Honey not only performs a reducing action against the Ag^+ ion but also is involved in the stabilization of the obtained nanostructures. Its stabilizing action is most likely due to the peptide component present in its matrix[82].

The AgNPs obtained with this completely green innovative methodology have more promising characteristics than those produced with a chemical method: the obtainable dimensions are a few

tens of nanometers, the stability of the colloid is several months and their antibacterial activity is preserved[82].

1.4. Titania nanoparticles, synthesis, properties, and their applications

Nanocrystalline Titanium dioxide (TiO_2) is a well-known semiconductor with photocatalytic activities, having great potential as a self-cleaning and self-disinfecting material in many applications. TiO_2 has been used broadly for killing different groups of microorganisms including bacteria, fungi, and viruses because it has high photoreactivity, broad-spectrum antibiosis, and chemical stability[108,109,110,111]. TiO_2 NPs decompose organic compounds by the formation and constant release of hydroxyl radicals and superoxide ions when exposed to non-lethal ultraviolet (UV) light, which is highly efficient in inhibiting the growth of methicillin-resistant *Staphylococcus aureus* (MRSA)[112]. This potent oxidizing power of TiO_2 NPs can be used against bacteria and other organic substances[113,114,115]. Regarding their industrial importance, the global market size of TiO_2NPs was estimated to be $1.1 billion in 2021 and predicted to reach 2.5 million tons by 2025[116,117]. In the biomedical fields, TiO_2NPs are frequently studied for photodynamic therapy,[118,119] drug delivery,[120] antimicrobial applications,[121,122] biosensors,[123] and tissue engineering[124]. **Figure 1.11** shows some current and future applications of TiO_2NPs. For all these mentioned applications, an appropriate surface modification of TiO_2NPs is required to improve their physicochemical properties and biological effects and, more importantly, decrease their potential toxicity in mammalian cells[125]. The surface modification not only prevents the agglomeration of TiO_2NPs but also provides the possibility for further functionalization/conjugation., and is forecasted to have a compound annual growth rate of 6.5% until 2026, with annual production.

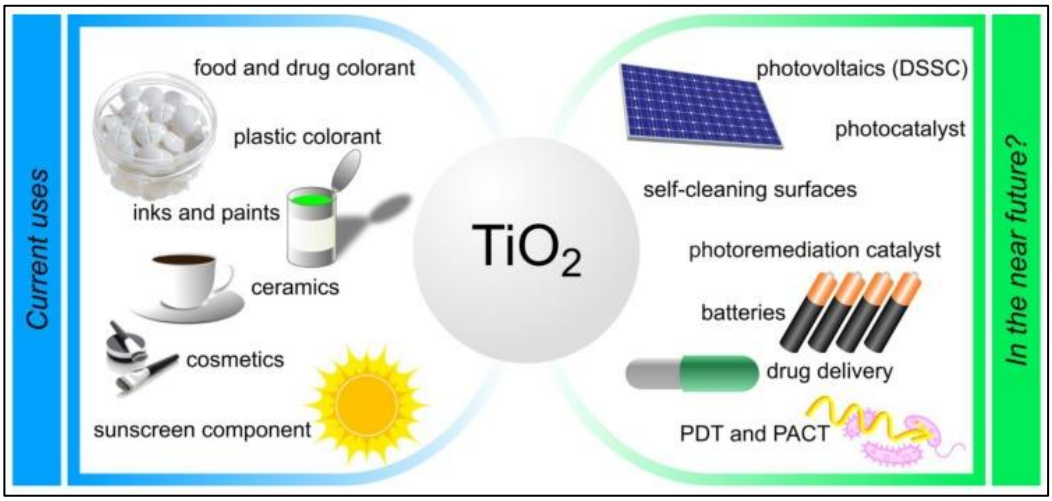

Figure 1.11. Current applications and potential future use of TiO_2. PDT, photodynamic therapy; PACT, antimicrobial photodynamic therapy; DSSC, dye-sensitized solar cell[126].

The relevant titanium dioxide is a semiconductor-based material with an energy gap of 3.23 eV for anatase and 3.06 eV for rutile polymorph[127,128]. If the molecule absorbs a photon with energy higher or equal to that value, it passes to an excited state and can produce negative electrons in the conduction band, leaving positively charged holes in the valence band. Free electrons may attack surrounding oxygen and water molecules to form ROS, including superoxide ($O_2^{\bullet-}$), hydrogen peroxide (H_2O_2), and hydroxyl radical ($OH^{\bullet}$) (**Figure 1.12**)[129]. These forms of oxygen are highly unstable in biological systems and react with the cell components causing apoptotic or necrotic cell death. It has also been proven that TiO_2NPs inhibit efflux-mediated multidrug resistance[105]. Due to the nature of TiO_2NPs when dispersed in aqueous solutions, in most cases, they tend to form agglomerates[130,131]. These forms have a decreased surface area and thus reveal also lower photoactivity. In addition to the biological activity of TiO_2NPs, sedimentation may lower their concentration and interfere with the reproducibility of the results, as well as prevent the steady dosage. Therefore, stable formulations of NPs anchored to supporting materials would be of great significance. Various materials have been tested as scaffolds such as glass, activated carbon, silica material, and polymeric materials[132133]

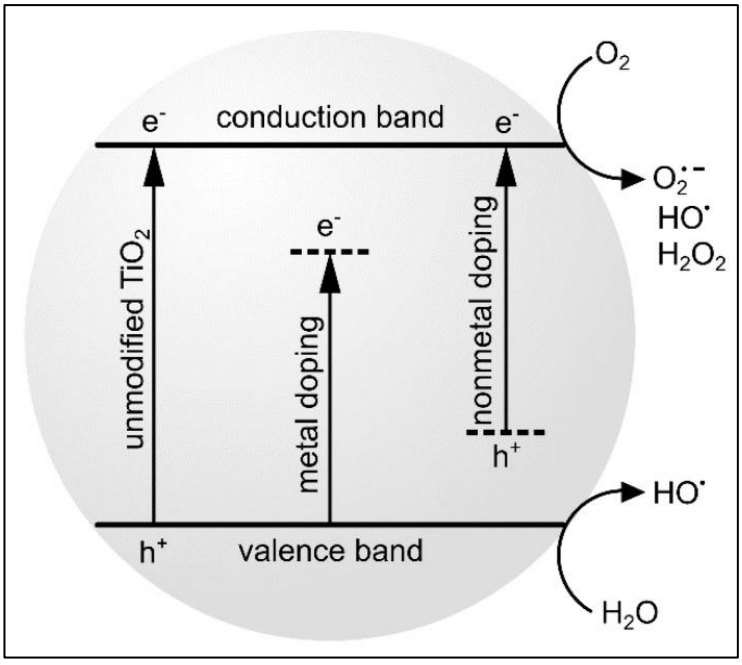

Figure 1.12. Simplified mechanism of reactive oxygen species generation by TiO_2[105].

The antimicrobial activity of nanoparticles is highly influenced by several intrinsic factors such as their morphology, size, chemistry, source, and nanostructure[134,135]. Specifically, the antimicrobial activity of TiO_2NPs is greatly dependent on the photocatalytic performance of TiO_2, which depends strongly on its morphological, structural, and textural properties[136]. Titanium dioxide produces amorphous and crystalline forms and primarily can occur in three crystalline polymorphous:

anatase, rutile, and brookite. Studies on synthesis have stated that the crystalline structure and morphology of TiO_2NPs are influenced by process parameters such as hydrothermal temperatures, starting concentration of acids, *etc*.[137]. The crystal structures and the shape of TiO_2NPs are both the most important properties that affect their physicochemical properties, and therefore their antimicrobial properties[138]. Regarding the crystal structures, anatase presents the highest photocatalytic and antimicrobial activity. Some works have shown that anatase structure can produce $OH^{\cdot}$ radicals in a photocatalytic reaction. TiO_2 is a thermally stable and biocompatible chemical compound with high photocatalytic activity and it has presented good results against bacterial contamination[139]. **Table 1.1** presents some research including the antimicrobial capacity of TiO_2NPs[140].

Table 1.1: TiO_2 nanoparticles against different microorganisms and their antimicrobial activities[116].

Microorganism	NPs	Results
Methicillin-resistant *Staphylococcus aureus*[141]	Fe_3O_4-TiO_2 core/shell magnetic NPs	The survival ratio [%] of bacteria decreased from 82.40 to 7.13%.
Staphylococcus saprophyticus[117]	Fe_3O_4-TiO_2 core/shell magnetic NPs	The survival ratio [%] of bacteria decreased from 79.15 to 0.51%.
Streptococcus pyogenes[142]	Fe_3O_4-TiO_2 core/shell magnetic NPs	The survival ratio [%] of bacteria decreased from 82.87 to 4.45%.
Escherichia coli [143]	TiO_2 nanotubes ~ 20 nm	97.53% of reduction
Staphylococcus aureus[119]	TiO_2 nanotubes ~ 20 nm	99.94% of reduction
Bacillus subtilis[144]	TiO_2 NPs co-doped with silver (19–39 nm)	1% Ag-N-TiO_2 had the highest antibacterial activity with antibacterial diameter reduction of 22.8 mm
Mycobacterium smegmatis[145]	Cu-doped TiO_2NPs ~20 nm	The percentage of inhibition was around 47%
Pseudomonas aeruginosa[146]	TiO_2 NPs 10–25 nm	Although it was not completely euthanized, their survival was significantly inhibited.
Shewanella oneidensis MR-1[121]	Cu-doped TiO_2 NPs ~20 nm	The percentage of inhibition was around 11%

Titanium dioxide nanoparticles (TiO_2NPs) are one of the most studied materials in the area of antimicrobial applications due to their particular abilities, such as bactericidal photocatalytic activity, safety, and self-cleaning properties. The mechanism referred to the antimicrobial action of TiO_2 is commonly associated to reactive oxygen species (ROS) with high oxidative potentials produced under band-gap irradiation photo-induces charge in the presence of O_2[147]. ROS affects bacterial cells by different mechanisms leading to their death. Antimicrobial substances with broad-spectrum activity against microorganisms (Gram-negative and Gram-positive bacteria and fungi) are of particular importance to overcome the MDR (multidrug resistance) generated by traditional antibiotic site-specific.

The main photocatalytic characteristic of TiO_2 is a wide band gap of 3.2 eV, which can trigger the generation of high-energy electron–hole pair under UV-A light with a wavelength of 385 nm or lower[122]. As mentioned above for bulk powder, TiO_2NPs have the same mechanism based on the ROS generation with the advantage of being at nanoscale. This nanoscale nature implies an important increase in surface area-to-volume ratio that provides maximum contact with environment water and oxygen[148] and a minimal size, which can easily penetrate the cell wall and cell membrane, enabling the increase of intracellular oxidative damage.

Bacteria have enzymatic antioxidant defense systems like catalases and superoxide dismutase, in addition to natural antioxidants like ascorbic acid, carotene, and tocopherol, which inhibit lipid peroxidation and the effects of ROS radicals such as $OH_2^{\bullet-}$ and $OH^{\bullet}$. When those systems are exceeded, a set of redox reactions can lead to the death cell by the alteration of different essential structures (cell wall, cell membrane, DNA, *etc.*) and metabolism routes[149]. In the following sections, several ways that cellular structures were affected in the presence of TiO_2 NPs will be described. In order to understand the genome responses of bacteria to TiO_2-photocatalysis, some biological approaches related to the expression of genes encoding to defense and repair mechanism of microorganisms will explained below. Different mechanisms and processes of antimicrobial activity of TiO_2 NPs are represented as a global scheme in **Figure 1.13**.

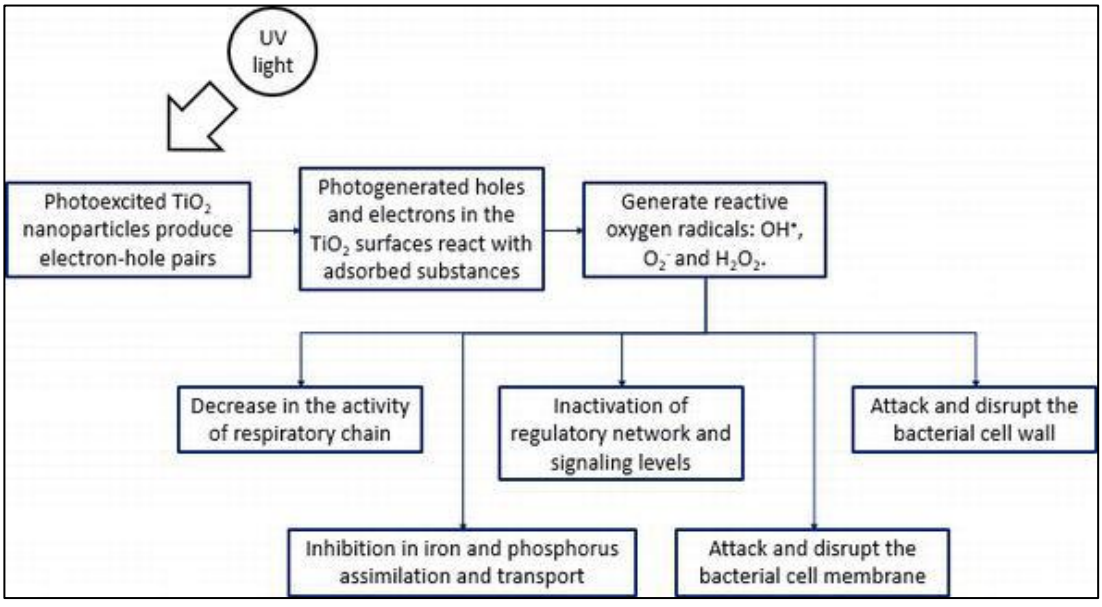

Figure 1.13. Scheme of main antimicrobial activity-based processes[149].

1.5. Magnetic nanoparticles, synthesis, properties, and their applications

Magnetic nanoparticles (MNPs), a nanoscale material, with unique magnetic properties, have been widely used in different fields such as biomedical, energy, engineering, and environment applications. The MNPs have become an area of intensive research in recent decades because of

their unique and distinguished properties which make their potential application in biomedicine, catalysis, agriculture, and the environment[150,151,152,153,154]. The MNPs are formed from different metal elements (either alone or in composites) and their oxides with magnetic characteristics[155]. Properties like high surface area, metal-rich moieties, and tunable structures make MNPs nanomaterials of great interest with broad applications in environmental, biomedical, catalysis, drug delivery, and bioimaging. Their tuning properties of shape and size have made them a hot topic in the past decades. The physicochemical properties of MNPs are different from their parental bulky material in terms of large specific surface area, which makes them more superparamagnetic[156].

The past decade has witnessed extensive research in the development of different approaches for the synthesis of MNPs. Different synthetic methods have been developed to obtain MNPs of desired size, morphology, stability, and biocompatibility. The most common methods include the ball milling method, coprecipitation, thermal decomposition, hydrothermal, microemulsion, sol-gel method, and biological method to produce MNPs. A graphical illustration of MNPs prepared through various routes (physical, chemical, and biological) is given in **Figure 1.14**[157].

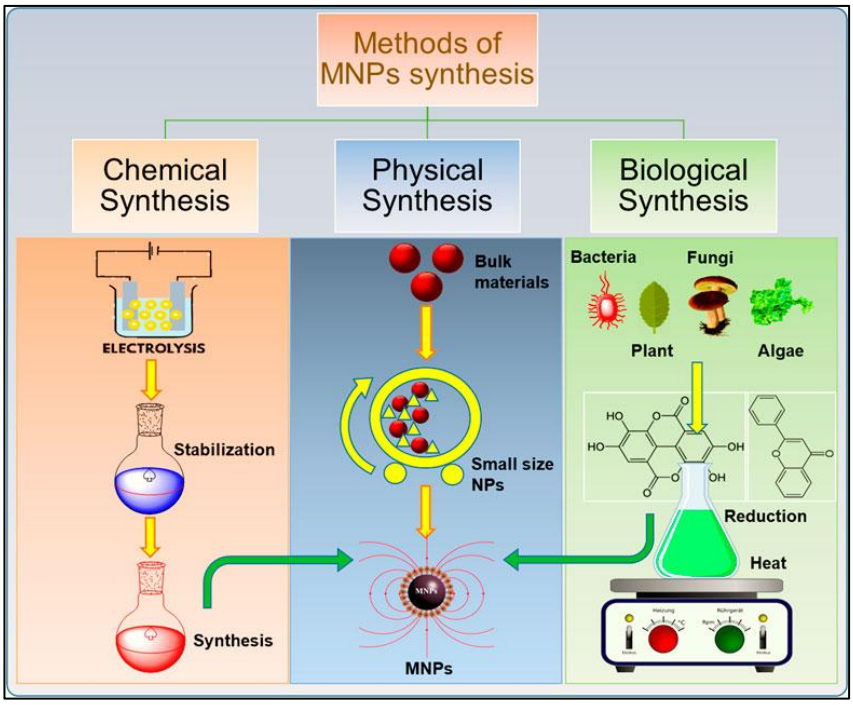

Figure 1.14. Schematic illustration of the synthesis of magnetic nanoparticles (MNPs) with different methods[157].

Coprecipitation is the most commonly used method for producing MNPs of controlled size and magnetic properties[158]. It includes the use of less harmful materials and procedures and is widely practiced in biomedical applications[159]. The synthesis of MNPs through coprecipitation is very convenient and facile when we need nanocrystals in large quantities. This method is very common for the production of NPs of controlled size with good magnetic properties. During the process of coprecipitation, different factors like pH, metal ions, and their concentrations, the nature of salt, the

reaction temperature can affect the composition of MNPs, particle size, and shape[160]. The MNPs synthesis through coprecipitation is quite simple to obtain uniformly dispersed small-size NPs[161]. Moreover, this method is preferred because of its simplicity but, sometimes it is difficult to control the shape of MNPs via coprecipitation.

The MNPs in the past decade have gained great attention because of their promising results in various fields. MNPs with super-magnetic properties, unique size, shape, high surface area, and volume ratio, and biocompatibility make their application more promising. Due to these properties, it has attracted more researchers from different fields. In this review, we have summarized the applications of MNPs in some well-known fields such as biomedicine, biosensing, environment, agriculture, and catalysis. Some of the applications of MNPs are shown in **Figure 1.15**.

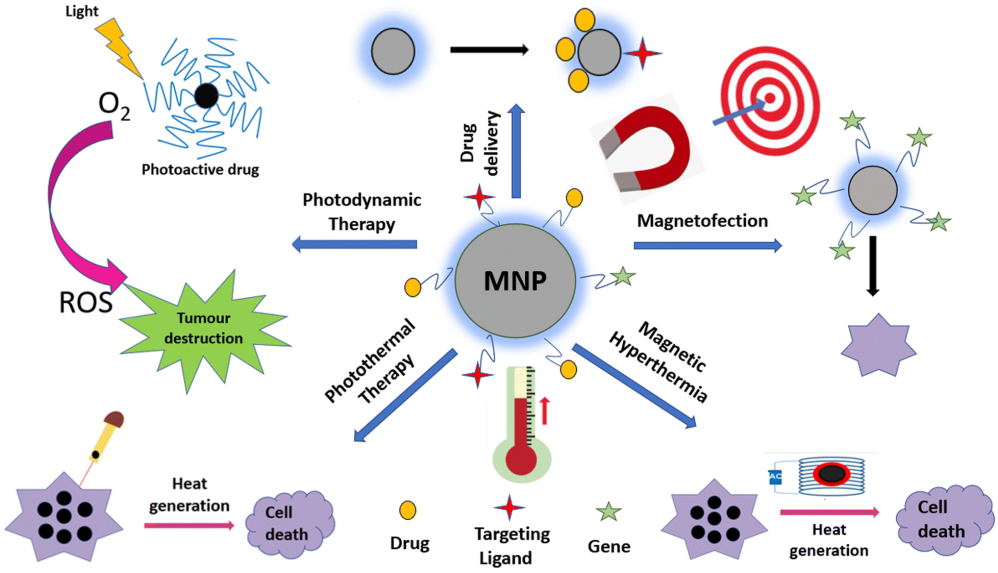

Figure 1.15. Schematic illustration of applications of magnetic nanoparticles (abbreviated as MNP)[161].

Nowadays magnetic nanoparticles, particularly nano zero-valent iron (nZVI), magnetite (Fe_3O_4) and maghemite (γ-Fe_2O_3) nanoparticles, and their applications in water treatment are an important field of research. They have a capacity for metal uptake from water thanks to some peculiar properties:

1. High surface to volume ratio; as explained above, which implies fast kinetics for contaminant removal[162].

2. Magnetism; a very useful property and, compared to sophisticated membrane filtration, a more cost effective method to separate nanoparticles from water[163].

3. Ability for surface modification, by covering the particles with inorganic shells or by attaching organic molecules to them. These properties may be used to stabilize the particles in order to

prevent their oxidation but also to provide them with specific functionalities, for example, to make them selective in ion uptake[164].

4. Low toxicity; Iron is a micronutrient, a substance essential for grow and survival in low amounts. However it can have adverse effects on living organisms at high concentrations.

5. Low price; Considering these nanoparticles can be synthesized using mainly iron salts, their price is limited, especially if compared with that of other types of nanomaterials, for example, gold nanoparticles.

Iron oxide is naturally abundant in nature in the forms of magnetite, Fe_3O_4 and maghemite, γ-Fe_2O_3. Hematite (α-Fe_2O_3) shows weak, size-dependent magnetism while maghemite shows strong ferromagnetism[165]. The performance of magnetic nanoparticles in removing contaminants depends on the removal mechanisms applied. The mechanism of heavy metals removal by magnetic nanoparticles can proceed through different processes such as adsorption, reduction, and co-precipitatin (**Figure 1.16**).

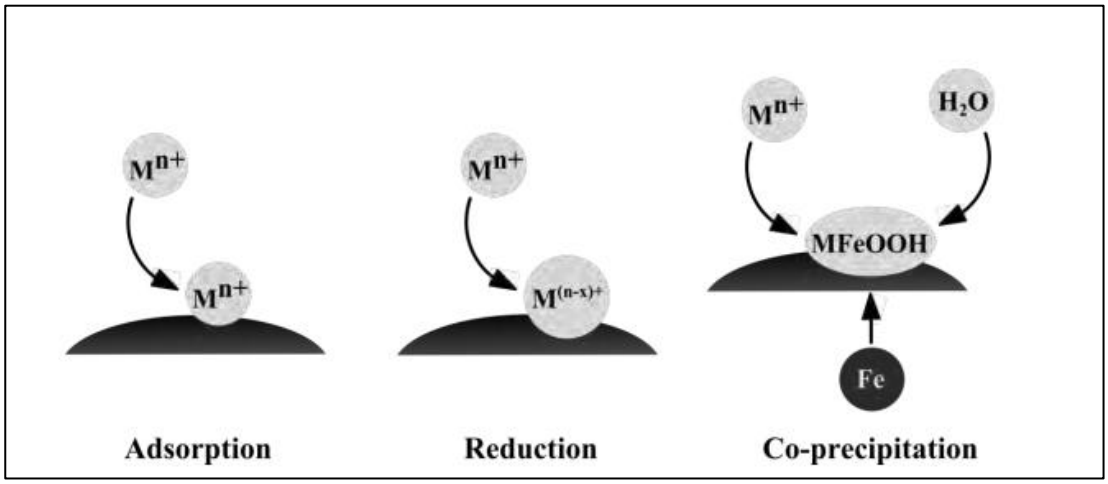

Figure 1.16. Different removal mechanisms used by magnetic nanoparticles[166].

Magnetite nanoparticles remove heavy metals by both physical and chemical adsorption based mechanisms, while maghemite particles usually give only physical adsorption. This is demonstrated also by the low desorption of metals at high pH that occurs when applying magnetite. Instead, adsorption by γ-Fe_2O_3 nanoparticles does not involve chemical reaction as demonstrated by the unchanged crystallite structure after metal removal. Electrostatic interactions are the cause of pollutant removal by maghemite nanoparticles. The removal performance of magnetite and maghemite nanoparticles is highly pH-dependent. At pH values below the zero point of charge (pHzpc), also called isoelectric point (IEP), the surface of iron oxide nanoparticles is positively charged and therefore attracts negatively charged pollutants such as Cr (IV) and As (V)[138].

Magnetic nanoparticles are susceptible to air oxidation and are easily aggregated in aqueous systems[167]. Thus, for the application of these nanoparticles in various potential fields the stabilization of the iron oxide particles by surface modification is desirable. The magnetic structure of the surface layer, which is usually greatly different from that in the core of the nanoparticles, can have a notable effect on the magnetic properties of nanoparticles[168] . The control of the size and the polydispersity are also very important because the properties of the nanocrystals strongly depend upon the dimension of the nanoparticles. It is interesting to mention that only magnetite particles with size of less than 30 nm have a large surface area and exhibit super paramagnetic properties that make them prone to magnetic fields. They do not become permanently magnetized without an external magnetic field to support them[169]. These properties are highly useful in the development of novel separation processes[170].

1.6. Objective of the work

Metal-based nanoparticles are the most popular inorganic nanoparticles and represent a promising solution against the resistance to traditional antibiotics. Not only do they use mechanisms of action that are completely different from those for traditional antibiotics, exhibiting activity against bacteria that have already developed resistance, but they also target multiple biomolecules compromising the development of resistant strains. In addition, The use of nanoparticles (NPs) for environmental applications is a current trend. Among various types of NPs, metallic NPs are widely used for environmental applications. Greener synthesis of NPs is preferred over chemical and physical methods as it is an eco-friendly, cost-effective, and sustainable approach.

One of the most interesting objectives from a scientific point of view is the search for new tools, capable of counteracting bacterial infections, which do not involve the use of antibiotics. In fact, more and more often pathogenic microorganisms have recently developed a resistance against the antibiotic drugs currently available on the market. According to a recent study commissioned by the British government, it is estimated that in 2050, antibiotic resistance will be responsible for over 10 million deaths a year, becoming the first cause of death to the world, even surpassing cancerous diseases.

In this context, innovative bio and nanotechnological approaches that exploit material nanostructures with antimicrobial properties, such as AgNPs and TiO_2NPs, to fight bacterial infections, bypassing the increasingly widespread problem of antibiotic resistance have been studied and developed.. The use of AgNPs, and TiO_2NPs with a high surface/volume ratio, greatly increases the already known bactericidal action of these NPs. Therefore such systems of Nano-sized metal/metal oxide-based represent a remarkable tool potential in the treatment of bacterial infections, such as those caused by *Staphylococcus aureus* and two Methicillin-Resistant *S. aureus* (MRSA) in patients with skin ulcers.

To further increase the efficacy and stability of these nanoparticles such as antimicrobial tools it is cost-effective to take advantage of the Drug Delivery Systems (DDS) capable of trap these bioactive substances, deliver them to the target site, and release them in a manner controlled over time. Hydrogels are promising biomaterials as delivery systems controlled: they consist of a three-dimensional lattice swollen with water in which it is possible trap bioactive substances, such as silver and titania nanoparticles. The composites developed consist of hydrogels based on short polypeptide chains (Fmoc-Phe_3) containing silver or titania or magnetic nanoparticles. The tripeptide Fmoc-Phe3, which constitutes the fibers of the three-dimensional network, was obtained for the biosynthetic route by means of a catalyzed, aqueous-phase reverse hydrolysis reaction by the

enzyme lipase from Pseudomonas fluorescents. The yield of this enzymatic reaction was already evaluated by HPLC in our group .

For the in situ synthesis of silver nanoparticles, we added silver salts to the hydrogelators and after hydrogel formation, exposure of the composite to the sunlight resulted in silver nanoparticles, which were observable by color changing. In another step, we introduced honey, which contains reducing polysaccharides, which accelerates the NPs reduction, and increases the yield while exposing it to the sunlight. It was investigated that honey also has a positive effect on the tensile strength and swelling ability of the composite. We also investigated the reduction ability of glucose as a green reducing agent and compared the stability and antibacterial activity of the glucose-reduced composites with NaBH4 as a traditional and chemical reducing agent.

Regarding the TiO_2NPs, they were bought commercially and added to the hydrogelators. We investigated the photo-antibacterial activity of these NPs against a laboratory Staphylococcus aureus strain and two Methicillin-Resistant S. aureus (MRSA) clinical isolates. We used two concentrations of titania to investigate the effect of concentration on swelling ability and mechanical stability. In addition, ultra sound waves also introduced to see its effect on the mentioned parameters of the hydrogel and the degree of dispersity of NPs inside of the hydrogels.

Moreover we investigated the use of γ-Fe_2O_3 as magnetic nanoparticles (MNPs) encapsulated with peptide hydrogels for the removal of heavy metal ions such as Cr^{3+}, Co^{2+}, and Ni^{2+} and some dyes like methyl orange (MO), methylene blue (MB) and rhodamine 6G (Rh6G) from water. In fact, heavy metals can easily bind to proteins, nucleic acids, and small metabolites in living organisms resulting in an alteration or loss of biological function and/or perturbation of the metal control site in the organism. Certain heavy metals in water are extremely toxic and non-biodegradable. Once they enter the food chain, they have the ability to accumulate at low concentrations in living organisms, with the potential to cause adverse effects such as damage to the nervous system, kidney failure, and cancer.

Co-precipitation method was used for the preparation of γ-Fe_2O_3-polyacrylic acid nanoparticles (γ-Fe_2O_3NPs-PAA) in collaboration with Prof. Frattodi's research group at the Department of Chemistry of Sapienza University. The already synthesized magnetite NPs in different concentrations were added to the hydrogelators to investigate their ability to entrap heavy metal ions (Cr^{3+}, Co^{2+}, and Ni^{2+}) from water in the presence and absence of external magnetic field.

2. Results

2.1. Preparation of the hydrogel composites containing AgNPs with antibacterial properties

On the basis of protocols optimized in previous works[171,172], we focused on developing a one-pot synthesis that could simultaneously allow the lipase-triggered formation of the $FmocPhe_3$ hydrogelator as well as the light-assisted reduction of Ag^+ ions into AgNPs. We were able to observe successful hydrogel formation after incubation at 30 °C for about 30 min. For the formation of AgNPs that are accompanied by a change in color of the hydrogel containing them, light exposure was necessary (**Figure S1 and S2 in Appendix A**). In this step, the synthesis of peptide-based hydrogel composites containing photo-generated silver nanoparticles (AgNPs) was obtained in the presence and absence of honey(Commercially prepared Miele Millefiori) as a coating agent for Ag NPs and tensile strength enhancer for the hydrogel (**Figure 2.1**).

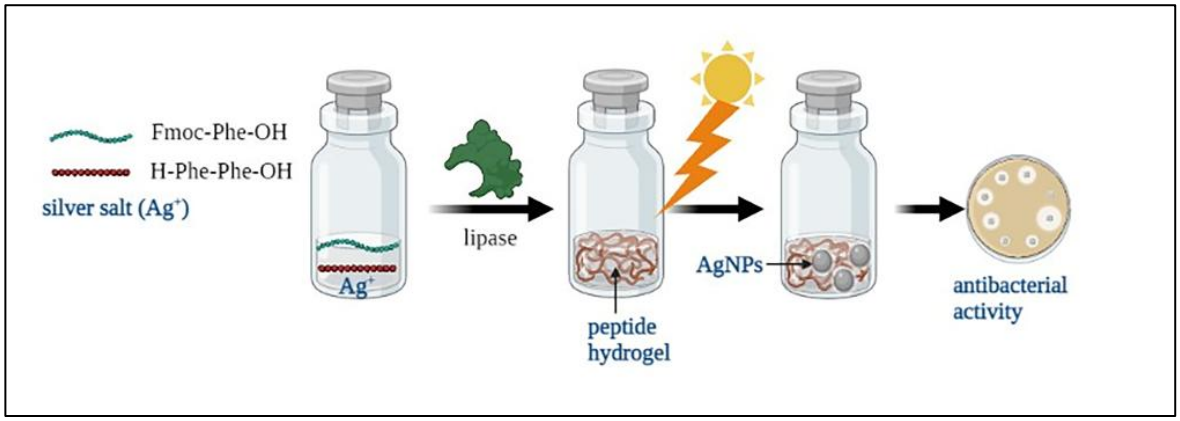

Figure 2.1. Illustration of in situ synthesis of AgNPs within peptide hydrogels using sunlight.

To investigate the effect of honey on composites, two different sets of experiments were performed, in the presence and absence of honey. To this aim, UV-Vis spectroscopy was used to study the plasmon band of in situ prepared AgNPs at different sunlight exposure times, with or without honey. As can be seen in **Figure 2.2a**, the light-assisted reduction of Ag^+ ions inside the hydrogel results in a broad plasmon band centered around 475 nm, indicating the presence of large and heterogeneous particles, ascribable to the absence of any stabilizer in the reaction medium. On the other side, the second experiment, carried out in the presence of honey, exhibits a significant blue shift with respect to the first experiment (**Figure 2.2b**). This indicates the strong size quenching effect of honey for the AgNPs/hgel system. For both results, spectra reveal that the intensity of the absorption peaks increases with the exposure time. More importantly, **Figure 2.2b** demonstrates that the rate of AgNPs formation is increased by the presence of honey probably due to the presence of mild reducing agents in honey such as reducing sugars[173].

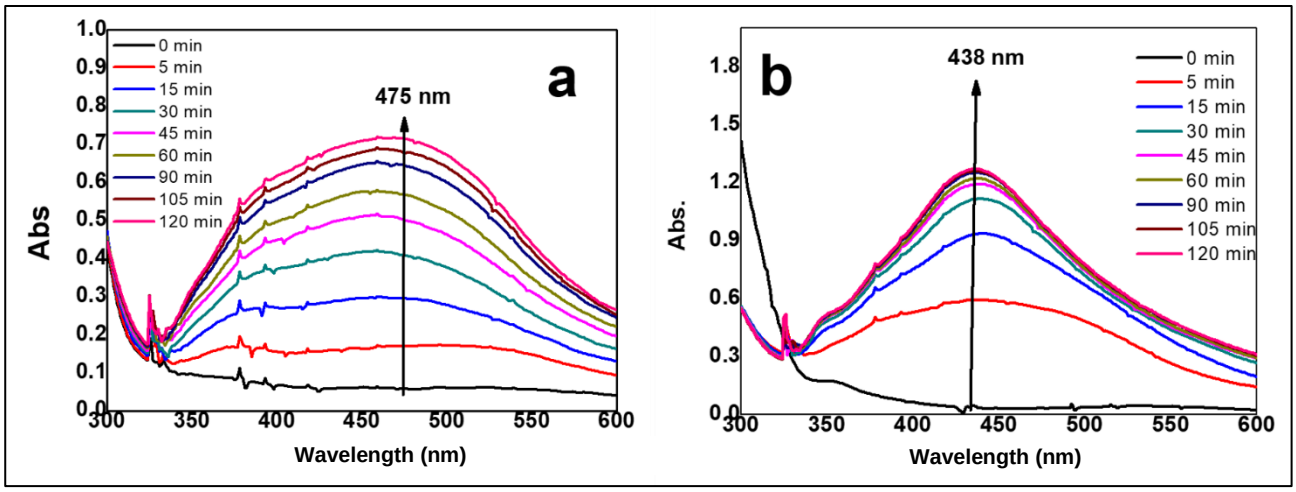

Figure 2.2. UV-Vis spectra of (a) AgNPs/hgel; (b) AgNPs/hgel-honey prepared at different irradiation times under sunlight exposure.

The formation of AgNPs in the presence of sunlight might be due to the fact that the aromatic residues of the peptide may allow radical generation, since they absorb UV light at 257 nm, which is similar to the wavelength of irradiation light. This hints at the fact that UV irradiation of the peptide may generate radicals that are necessary for Ag^+ reduction[174]. Moreover, after approximately 90 min, the intensity reaches a plateau, suggesting that NPs formation has completed.

In order to quantify the reduction of Ag^+ ions and Ag^0 formation, we analyzed samples with ICP-OES technique. Theoretically, there would be 20.00 ppm of Ag^0 inside the sample solutions if the sunlight required by our protocol could successfully reduce the entire amount of Ag^+ precursors used in the synthesis. However, the results of ICP-OES showed the presence of only 5.9 ± 0.1 ppm of silver inside the diluted solutions. Since the unreacted silver ions had been filtered out of the suspensions before the measurements, we calculated the reaction yield for the formation of AgNPs, by dividing the theoretical value to the obtained value from ICP-OES measurements, which was 29.5%. This suggests that the use of honey does not have any significant effect on NPs yield (data not shown).

Moreover we approached dynamic light scattering measurements to measure the size and degree of poly-dispersion of AgNPs produced with and without the honey. **Figrue 2.3a** shows the size distribution of the AgNPs/hgel system, supporting the presence of two populations in this experiment with an average diameter of 66 ± 25 and 122 ± 48 nm for AgNPs in these conditions. This is consistent with the UV-Vis spectra obtained, which showed a broad plasmon band supporting the observed poly-dispersity (see previous section, **Figure 2.2**). However, in the presence of honey (**Figure 2.3b**), the particles dimensions are more homogeneous compared to the first system, and only one population is observed in these conditions, with a mean particle size of

164 ± 63 nm and a PDI of 0.3 demonstrating monodispersed AgNPs, confirming the stabilizing effect of honey on the size of AgNPs, which is consistent with the UV-Vis data.

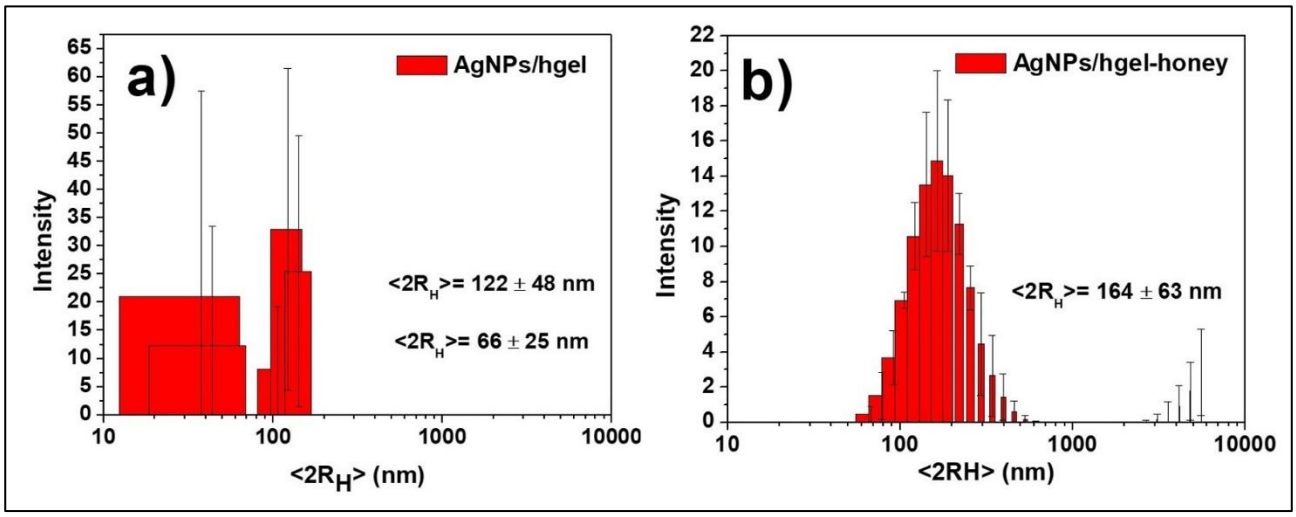

Figure 2.3: Hydrodynamic diameter distributions of (**a**) AgNPs/hgel; (**b**) AgNPs/hgel-honey measured by DLS.

The morphology of the hgel, AgNPs/hgel and AgNPs/hgel-honey was investigated by SEM technique. **Figure 2.4A** shows the three-dimensional fibrillar network of the hgel. The length of the fibrils constituting the network is several micrometers and their width is 100–150 nm. On the other hand, SEM micrographs reported in **Figure 2.4B,C** show the AgNPs/hgel and AgNPs/hgel-honey samples. The presence of AgNPs covered by fibers is evident, suggesting the incorporation of AgNPs within the hydrogel fibrillar network in both samples. Regarding the SEM images obtained for AgNPs in the absence and presence of honey (**Figure 2.4B–D** respectively), greater aggregation is shown when the synthesis is carried out without honey. It can be deduced that honey itself would increase the degree of stabilization and particle size reduction of AgNPs.

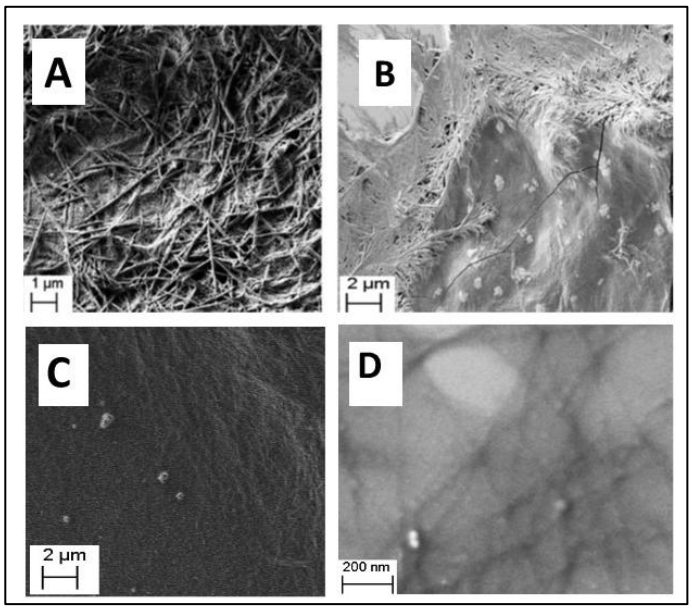

Figure 2.4. FESEM images of (**A**): hgel; (**B**): AgNPs/hgel; (**C**,**D**): AgNPs/hgel-honey.

To further investigate the nature of Ag species within the hydrogel, XPS analyses were conducted on the pristine hydrogel (hgel) (control experiment, not shown) and on the AgNPs/hgel sample obtained from photochemical reduction of $AgNO_3$, with the spectra of the latter shown in **Figure 2.5**. In spectrum (a) of **Figure 2.5**, the C 1s photoionization region is reported, which shows three main contributions attributed to the more representative chemically in equivalent C atoms in the Fmoc-(L-Phe)$_3$ backbone: (i) aromatic and aliphatic C atoms at 284.8 eV (red curve); (ii) C atoms at 286.5 eV, presumably associated to the -NH-C(H)-C(O)-NH- fragment; (iii) amidic C in the -C(O)-NH- fragment at 288.2 eV, with small contributions from -C(O)O- (carboxylate) and -NH-C(O)O- (carbamate) fragments[175]. The N 1s spectrum (**Figure 2.5b**) shows a single contribution at 399.9 eV, perfectly compatible with an amidic N atom[176], while possible residuals of NO_3^- can be excluded. The presence of Na was also detected (**Figure 2.5c**), yet the Na 1s electrons displayed a binding energy of 1077 eV, higher than that usually detected in sodium salts (~1072 eV)[186]. This shift may stem from possible aggregates of NaCl resulting from the NaOH/HCl treatment during preparation, which induce a partial electrostatic charging under the X-ray beam. The presence of AgNPs was ascertained by recording the photoelectron spectrum in the region of Ag 3d (**Figure 2.5d**). In this case, a spin-orbit split doublet appears (ΔE_{so} = 6.0 eV) with components in the area ratio 6:4, as expected for j'' = 5/2 and j' = 3/2 total angular momentum values. According to peak-fitting results, two chemical components contribute to this signal, a predominant one at 367.5 eV and another at 368.1 eV (j'' = 5/2 components). These features can be assigned to Ag(I) (dark cyan curve in **Figure 2.5d**) and Ag(0) (magenta curve in **Figure 2.5d**), respectively, in accordance with the literature[187]. The presence of a majority Ag(I) component calls for the formation of a shell of oxidized silver around the metal core of the NPs. The low intensity of Ag metal signal is probably due to the attenuation of electrons from the inner core of the NP, while the outer shell signal is enhanced.

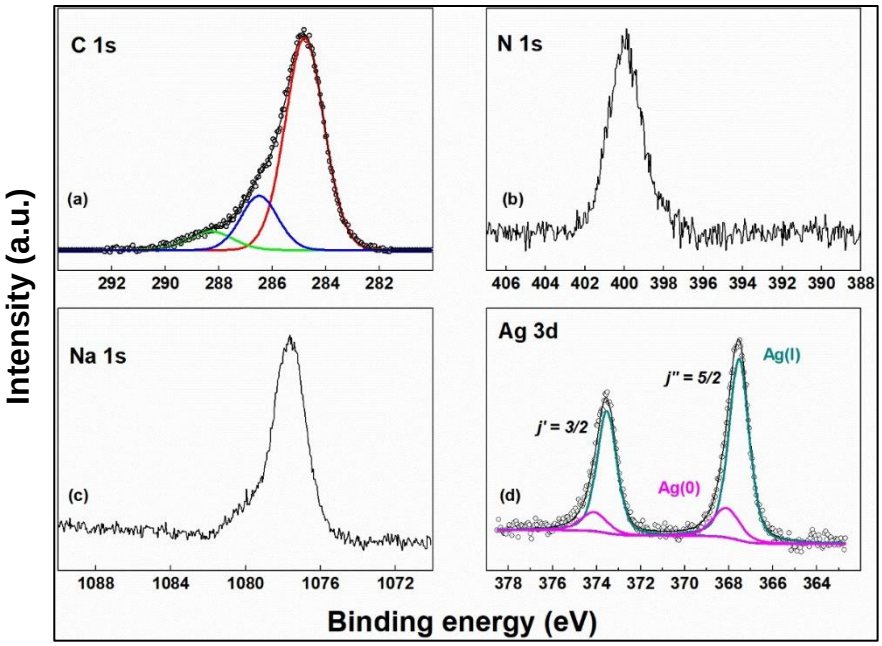

Figure 2.5. XPS spectra of Fmoc-(L-Phe)$_3$ hydrogel + Ag^+ in the regions of (**a**) C 1s, (**b**) N 1s, (**c**) Na 1s, (**d**) Ag 3d.

To study the structural features of hgel, AgNPs/hgel, and AgNPs/hgel-honey, the SAXS profiles for these three samples were collected. For the AgNPs/hgel system, two replicates were analyzed, and one sample was prepared two weeks before the analysis. As can be seen in **Figure 2.6**, the data of the AgNPs/hgel (1) (red) and the AgNPs/hgel (2 w) (purple) show overall the same profile indicating a good stability over time and reproducibility of the process of sample preparation, leading to the same structure at the investigated length-scales (1–100 nm).

We can mention that the visual appearance of the samples results slightly inhomogeneous at a macroscopic scale, showing regions with a more intense red color probably related to a higher local concentration of AgNPs; therefore, for SAXS data collection we tried to sample the regions of capillaries with an intense color. All samples show isotropic scattering patterns even if the pre-formed gels were injected into borosilicate capillaries with a long needle syringe and then shaken to fill the bottom. The data of the pristine hydrogel (hgel, black dots) show the profile of fibrillar structures[177], having a cross-section with a radius of gyration of approximately 3 nm and an overall maximum diameter of around 8–10 nm as also deduced by the pair distance distribution function (**Figure 2.6b**). For $q < 0.2$ nm^{-1} the slope deviates from the q^{-1} predicted for rod-like objects towards more negative values (towards −2) and this could be interpreted as due to the branched fibrillar network (the fibrils cannot be seen as individual rods anymore at larger length scales compared to their cross-sections). The SAXS profile obtained for the AgNPs/hgel is in the q-range > 0.4 nm^{-1} almost superimposable to that of the hydrogel sample, suggesting that the fibrillar cross section is not perturbed. However, additional scattering signal and oscillations can be seen in the lower q. We could attribute these to the Ag nanoprecipitated structures within the hydrogel and

considering the impossibility of seeing a Guinier region for these inhomogeneities we could estimate that their size is above 100 nm.

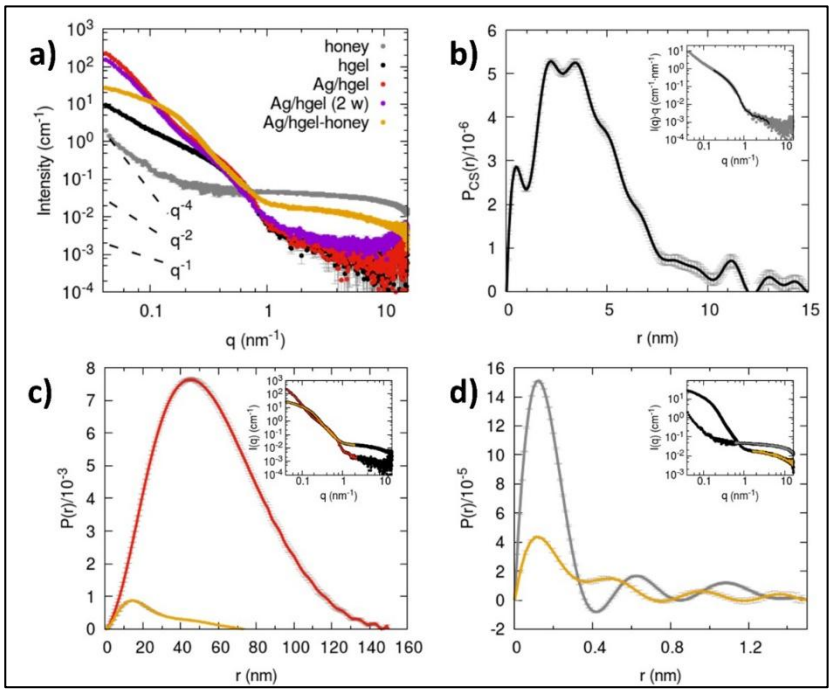

Figure 2.6. (**a**) SAXS profiles of honey, hgel, AgNPs/hgel, and AgNPs/hgel-honey. Characteristic power laws are reported for reference; (**b**) pair distance distribution function of the cross section $P_{CS}(r)$ obtained for the hgel sample (fit in the inset). (**c**) Pair distance distribution functions P(r) obtained for the Ag/hgel and Ag/hgel-honey samples (fits in the inset). (**d**) P(r) obtained for the honey and Ag/hgel-honey samples considering the high q portion of the data (q > 1 nm^{-1}) (fits in the inset).

For the AgNPs/hgel obtained in the presence of honey, the SAXS curve shows marked differences from the AgNPs/hgel sample both in the low *q* (<0.4 nm^{-1}) and the higher *q* (>1 nm^{-1}); in the latter region a signal related to some inhomogeneities with a radius of gyration smaller than 0.2 nm is detected. We hypothesize this high *q* scattering signal comes from honey molecular components like small oligosaccharides, since a sample of diluted honey at the same concentration used for the AgNPs/hgel synthesis also shows a similar contribution, corresponding to even smaller sizes (overall < 0.4 nm, **Figure 2.6d**). Regarding the shape of the SAXS profile in the low *q*, we can comment that for the AgNPs/hgel-honey sample it shows a lower slope and much lower intensity than the AgNPs/hgel sample, suggesting smaller structures (diameters of approximately 30 nm) are formed by the Ag nanoprecipitation in the presence of honey (**Figure 2.6c**). We could relate this observed difference to the difference in visual appearance between the Ag-gels obtained without and with honey (opaque with larger precipitates vs. transparent with smaller precipitates), which are related to light scattering phenomena, the UV-Vis absorption data, and the SEM micrographs.

The rheological properties of hydrogel materials play a pivotal role in defining their application potential, so their evaluation is of crucial importance. The goal of this analysis is to understand how the presence of AgNPs synthesized in situ affects the viscoelastic behavior of the hydrogels, by

measuring G’ (elastic modulus) and G” (viscous modulus). As shown in **Figure 2.7**, the AgNP/hgel had the lowest storage modulus. These results suggested that incorporating AgNPs inside the matrix decreased mechanical strength, due to providing porousity inside of the hydrogelsRegarding the AgNPs/hgel-honey composite, there is a significant increase in both G’ and G” moduli and therefore a marked improvement in mechanical properties can be seen. The complex biological matrix of honey, which acts as a stabilizer for AgNPs, may itself interact with the peptide components in the hydrogel, forming further crosslinks and consequently making the gel stronger.

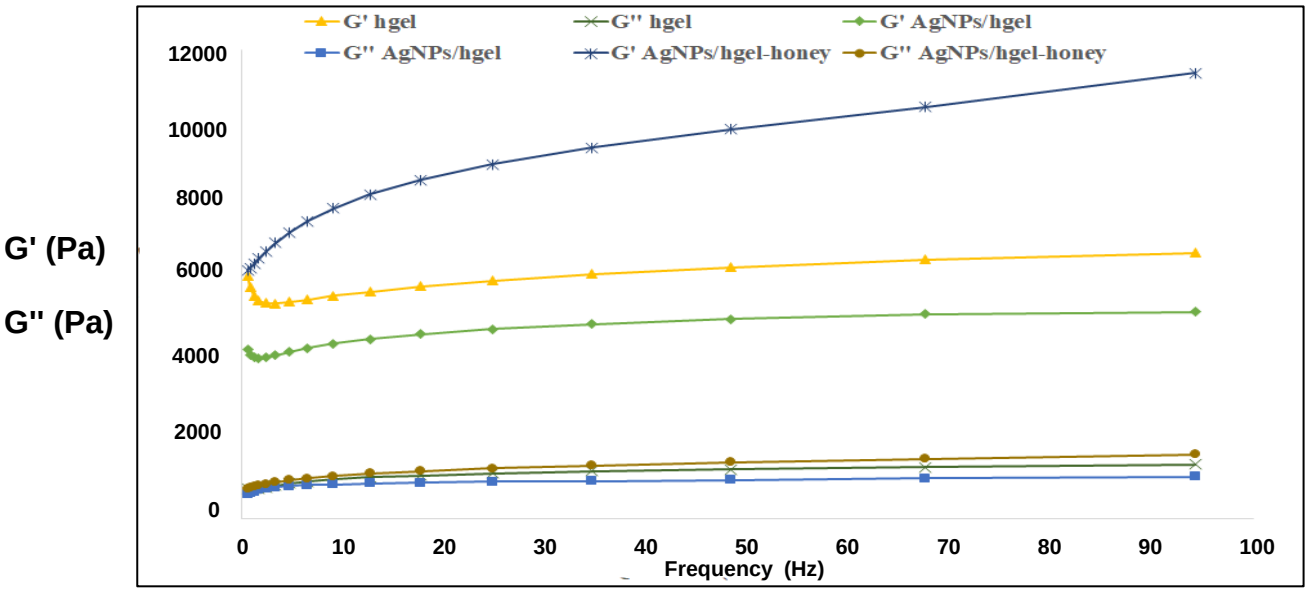

Figure 2.7. Frequency sweep of hgel, AgNPs/hgel and AgNPs/hgel-honey samples.

The swelling ability of AgNPs/hgel and AgNPs/hgel-honey samples was measured and compared with that of the hgel (**Table 2.1**). The results reveal that AgNPs/hgel showed higher swelling behavior in comparison to the hgel. The enhancement in swelling behavior of AgNPs/hgel might be related to the presence of AgNPs in different sizes and surface charges, that resulted in the penetration of a higher amount of water molecules in order to counterbalance the built up osmotic pressure[178]. However, this swelling enhancement also might be related to the formation of AgNPs inside of the hgel matrix that expands the hydrogel network and consequently more water absorption[189]. Regarding the AgNPs/hgel-honey, it increased the swelling behavior the most which is related to its hygroscopic features[179].

Table 2.1. Swelling abilities of the hydrogel systems.

samples	Swelling degree (q)
hgel	62.1 ± 0.3
AgNPs/hgel	75.9 ± 0.6
AgNPs/hgel-honey	79.1 ± 0.2

The antimicrobial susceptibility profiles of the laboratory strain *S. aureus* ATCC 25923 and MRSA clinical isolate for the tested compounds are summarized in **Figure 2.8**. In particular, the hydrogel alone showed a reduced toxicity compared to AgNPs and AgNPs-honey, with a minimum inhibitory concentration (MIC) of 12.5 mg/L for both *S. aureus* ATCC 25923 and the MRSA isolate. Conversely, the AgNPs/hgel and AgNPs/hgel-honey showed an enhanced antibacterial activity (3.12 mg/L) compared to the free form of AgNPs, alone or in combination with honey (6.25 mg/L) for both *S. aureus* ATCC 25923 and the MRSA isolate.

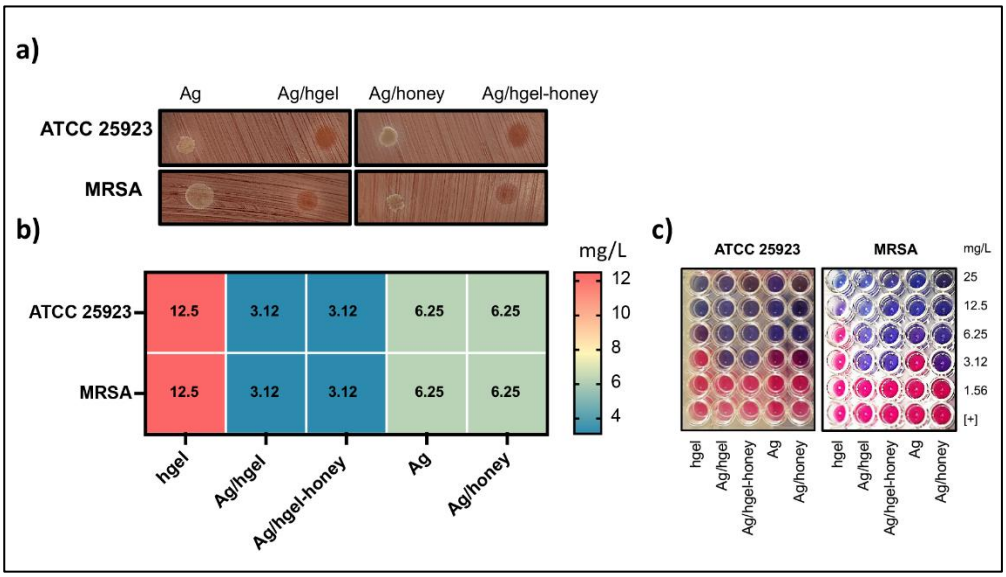

Figure 2.8. Antimicrobial susceptibility testing (AST) of AgNPs in the hydrogel composite. compared to the free form of AgNPs against *Staphylococcus aureus* ATCC 25923 and the methicillin-resistant *Staphylococcus aureus* (MRSA) clinical isolate. (**a**) Representative pictures for the plate inhibition zone test performed for different AgNPs formulations against ATCC 25923 and MRSA. Chocolate agar plates contained 20 µL of 3.12 mg/L solution of each compound tested. (**b**) Minimum inhibitory concentration (MIC) for hgel, AgNPs/hgel (Ag/hgel), AgNPs/hgel-honey (Ag/hgel-honey), AgNPs alone (Ag), and AgNPs + honey (Ag/honey). (**c**) Determination of MIC by resazurin microtiter assay method for the *Staphylococcus aureus* ATCC 25923 strain. Bacterial cells, incubated in cation-adjusted Mueller-Hinton broth (MHB) in the presence of resazurin (blue), were exposed to different compounds for 24 h. A change from blue to pink is indicative of the reduction of resazurin and, consequently, bacterial growth. The MIC was defined as the lowest drug concentration that prevented this color change. Experiments were performed in triplicate and repeated three times.

In another study, AgNPs/hgel composites were synthesized in another way using two different reducing agents. The novelty of this step lies in the development of different synthetic methodologies for one-pot preparation of AgNPs/hgel, where AgNP formation occurs *in situ* and

simultaneously with the sol–gel transition. The first synthesis involved the use of sodium 3-mercapto-1-propanesulfonate (3MPS) as a stabilizing agent and $NaBH_4$ as a reducing agent. Then, we moved on to a green approach, exploiting the reducing properties of monosaccharides such as glucose. We compared the effect of the preparation technique of composite hydrogels on the size, monodispersity, and stability of *in situ* synthesized AgNPs (**Figures 2.9, S3 and S4**).

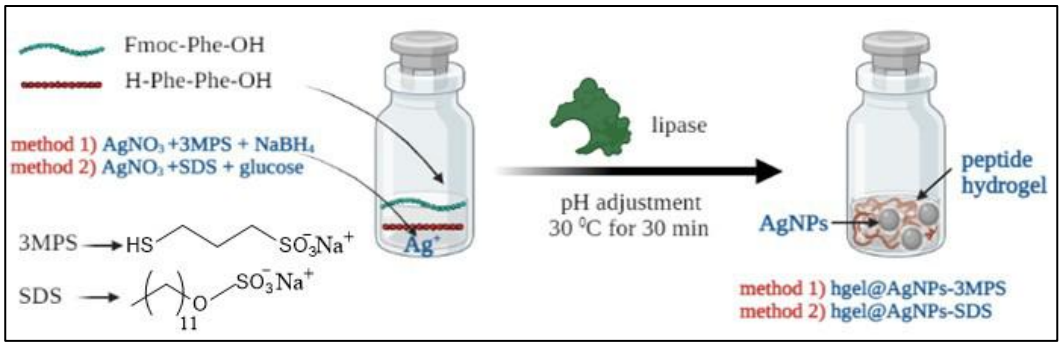

Figure 2.9. Scheme of the preparation of hgel/AgNPs composites with conventional and green methods.

Aiming to characterize in situ formed AgNPs, their optical features such as the presence of SPR (surface plasmon resonance) band as a function of time were studied. Different experiments were performed to investigate the influence of storage temperature and duration on AgNP surface plasmon resonance values. Firstly, the evolution of AgNPs absorbance in the presence of $NaBH_4$ as a function of reaction time was investigated. Samples stored at room temperature (RT) and 4 °C were examined. **Figure 2.10A,B** show the time evolution of the adsorption spectra of AgNPs synthesized in the hydrogel with $NaBH_4$ and 3MPS at different temperatures. For both temperatures, the SPR band of AgNPs, centered at 475 nm, tends to decrease, and the plasmonic peak tends to widen over time. This is most likely due to the poor stability of AgNPs, which tend to aggregate. The reported data show that sample storage at 4 °C partially prevents aggregation, probably due to a reduction in diffusion phenomena within the hydrogel matrix.

As can be seen from the spectra (**Figure 2.10C**), the SPR band of AgNPs-SDS synthesized with β-D-glucose at RT increases over time, while in the case of $NaBH_4$-mediated AgNPs synthesis, the SPR band decreases with time. In addition, for AgNPs synthesized with glucose, the SPR band is present at a smaller wavelength (425 nm), and it is narrower than the SPR peak of AgNPs synthesized with $NaBH_4$. These experimental observations could be due to the different AgNP formation kinetics obtained with the two different reducing agents. $NaBH_4$ is a strong reducing agent, used in combination with 3MPS thiol. AgNPs could be subjected to an oxidation process with the formation of an Ag_2O shell[180]. As a result, aggregation equilibria occur, and the band gradually widens and decreases over time.

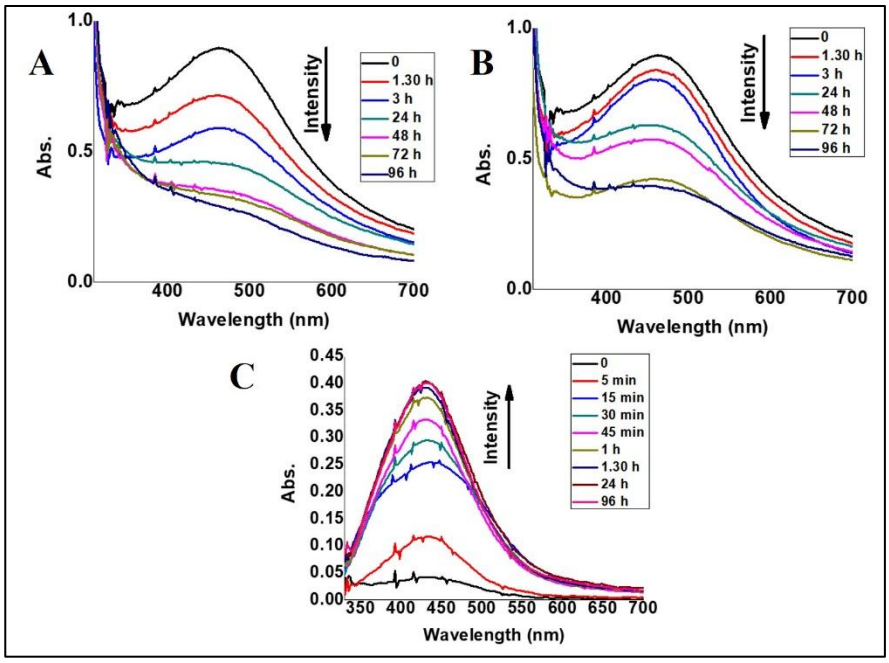

Figure 2.10. UV-Vis analysis in water. (**A**,**B**) The absorbance of hgel/AgNPs-3MPS at RT and 4 °C, respectively. (**C**) The absorbance of hgel/AgNPs-SDS at RT.

However, the use of a milder reducing agent such as β-D-glucose may account for a slower AgNP formation that increases with time. In addition, the presence of SDS as the capping agent seems to prevent AgNPs aggregation, resulting in a smaller and narrower SPR band.

The yield of AgNPs formed from Ag^+ ions, using both β-D-glucose and $NaBH_4$ as reducing agents, was calculated on the basis of ICP-AES experiments. According to ICP data, the amount of formed AgNPs in the presence of β-D-glucose and $NaBH_4$ is equal to 1.2 ± 0.14 and 4.2 ± 0.11 ppm, respectively. Dividing these amounts by the theoretical value indicates that the reaction yields are 23.5% and 82.3% for AgNPs formed using β-D-glucose and $NaBH_4$, respectively. As expected, in the optimized reaction conditions, the use of $NaBH_4$ leads to higher yields of formed AgNPs, given that this compound is a strong reducing agent.

DLS measurements were performed to estimate AgNP size and polydispersion degree. The size of the AgNPs is a fundamental parameter to be considered in the realization of antimicrobial nanosystems. In fact, many of their chemical and physical properties, such as stability, reactivity (proportional to their surface/volume ratio), and release kinetics of Ag^+ ions could be affected by size. The interaction processes of AgNPs with biological systems are also size dependent. **Figure 2.11A,B** shows the distributions of the hydrodynamic diameters of AgNPs synthesized using $NaBH_4$ and β-D-glucose as reducing agents.

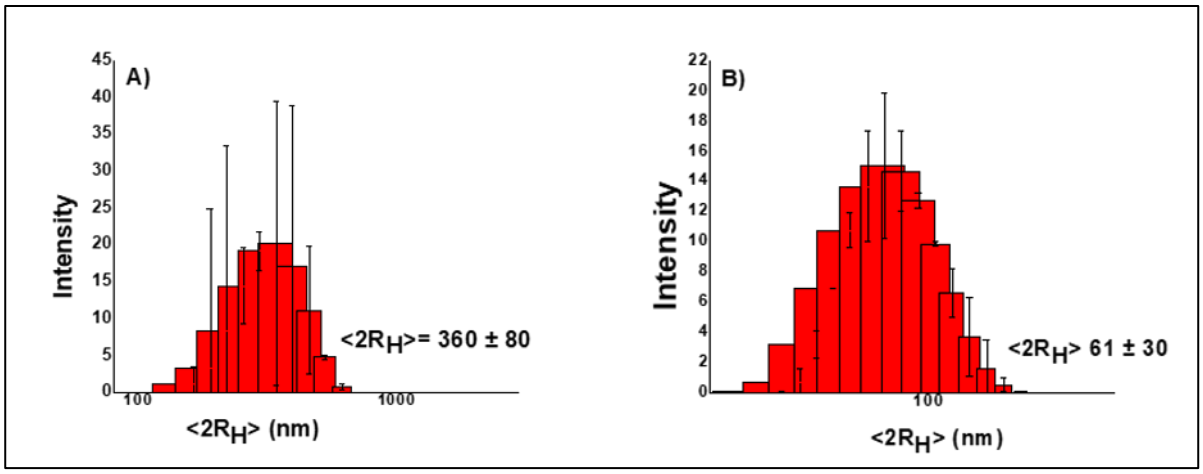

Figure 2.11. Hydrodynamic distribution of (**A**) hgel/AgNPs-3MPS and (**B**) hgel/AgNPs-SDS.

As can be seen, AgNPs synthesized using $NaBH_4$ as a reducing agent have larger dimensions and polydispersion (~360 nm, PDI: 0.475), compared to those obtained using β-D-glucose (~60 nm, PDI: 0.233). Certainly, different factors may be responsible for such differences in AgNP dimensions and polydispersion. Higher AgNP concentrations may enhance particle aggregation within the hydrogel structure (as when using $NaBH_4$). In addition, the structure of the capping agent could affect the final dimensions and/or particle aggregation.

The morphological features of the native hydrogel and hgel/AgNPs were investigated using SEM. **Figure 2.12A** shows a micrograph of the native hydrogel in which the fibrous nature of the highly reticulated three-dimensional network can be seen. **Figure 2.12B–E** is related to hgel/AgNPs-SDS and hgel/AgNPs-3MPS, respectively, and their high-resolution images. It can be seen that the presence of AgNPs does not affect the ability of the Fmoc-Phe3 tripeptide to self-assemble into supramolecular structures giving rise to composite gels with a highly cross-linked fibrillar morphology. Moreover, in both composites, AgNPs appear as well dispersed inside the hydrogel matrix.

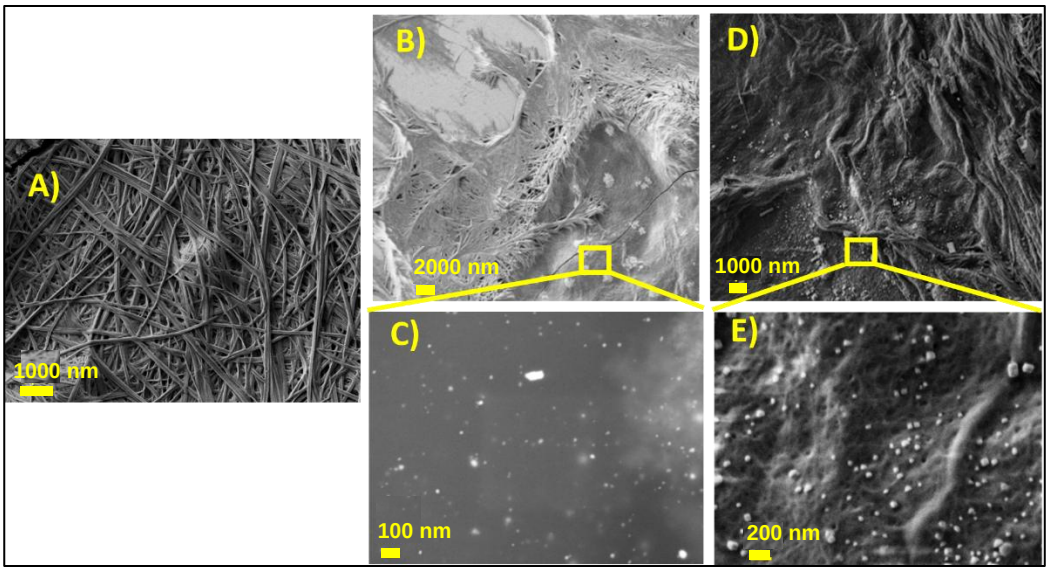

Figure 2.12. SEM images of (**A**) native hydrogel; (**B**) hgel/AgNPs-SDS; (**C**) hgel/AgNPs-SDS at high magnification; (**D**) hgel/AgNPs-3MPS; and (**E**) hgel/AgNPs-3MPS at high magnification.

Studying the rheological features of hydrogels is pivotal for evaluating their application potential. With the aim to analyze the viscoelastic behavior of hydrogel composites, we used a dynamo-mechanical analysis, and the measurements were conducted in an oscillatory mode, at different application frequencies of the stimulus under constant strain. Both hydrogel samples containing AgNPs, formed in situ with the two different protocols described in **Appendix A 4.3 methodologies**, as well as the native control hydrogel, were analyzed. The aim of this study was to quantify the influence of in situ formed AgNPs on the viscoelastic behavior of the composites, and therefore how the elastic and viscous moduli of the hydrogels changed. The results for all samples are reported in **Figure 2.13**.

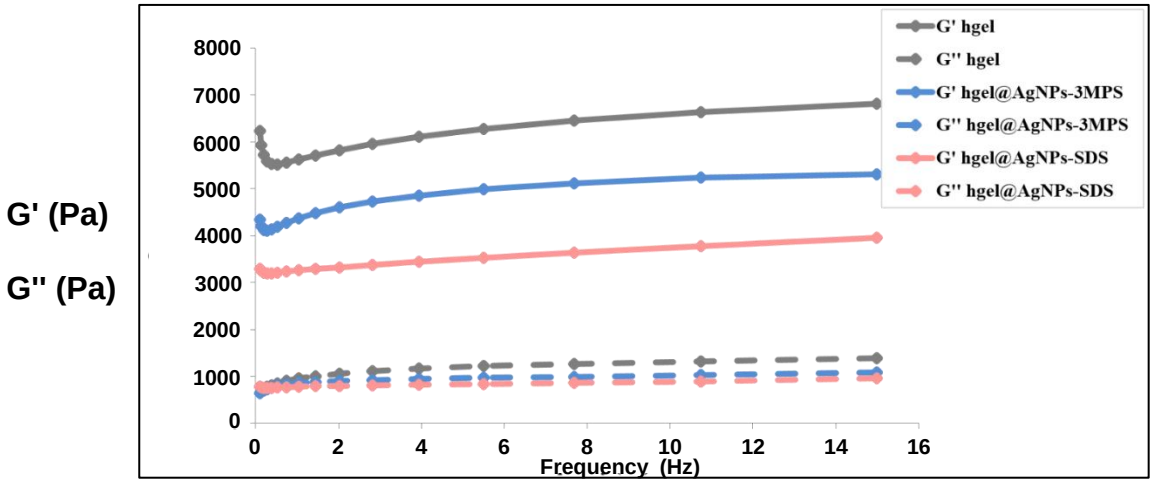

Figure 2.13. Frequency sweep of the hydrogel; hgel/AgNPs-3MPS; and hgel/AgNPs-SDS.

Regarding all types of hydrogels, the elastic modulus G′ and the viscous one G” do not vary according to the oscillation frequency but remain almost constant for the entire frequency range

analyzed. On this basis, a solid-like behavior is found (G′ > G″), whatever the frequency of the stimulus to which the sample is subjected. This indicates that there is a gel or a three-dimensional network in which chains, in this case, peptides, are held together thanks to physical and chemical crosslinks that prevent their sliding (typical of a liquid system) even at low frequencies. In fact, in the gel, there are only conformational variations in the peptide chains and translational motions of these chains are absent. Furthermore, from the frequency sweep experiments conducted, it is possible to obtain information also regarding the strength of the gel. Since the elastic modulus G′ is much higher than the viscous one G″ for all samples, it is possible to state that they are in the presence of strong and stable hydrogels.

In particular, with hgel/AgNPs-3MPS, we can observe a reduction in the mechanical properties compared to the hydrogel alone. In this case, the 3MPS stabilizer and $NaBH_4$ reducing agent could negatively influence the hydrogel gelling ability. In fact, physical crosslinks are present in the peptide hydrogel, such as hydrophobic interactions and aromatic π–π stacking (due to the presence of benzyl groups in the side chain of the amino acid phenylalanine), which can be reduced in the presence of polar compounds such as 3MPS and $NaBH_4$. As far as the hgel/AgNPs-SDS samples are concerned, we obtained a significant reduction in the viscous modulus G″ and, in particular, of the elastic one (G′). This indicates that a weaker gel is present, probably due to the presence of the amphiphilic surfactant SDS. In fact, the latter has a polar head that could affect the hydrophobic interactions that hold together the peptide lattice of the hydrogel.

The stability of hydrogel composites in physiological conditions, being an important feature for biological applications, was evaluated. The obtained results are summarized in **Table 2.2**.

Table 2.2. Percentage of weight loss (ΔW %) after 30 days of incubation in Ringer solution and daily degradation rate (T) of native and composite hydrogels.

Samples	ΔW %	T
Native hydrogel	9.1 ± 2.3	0.3±0.08
hgel/AgNPs-SDS	10.8 ± 1.7	0.3±0.06
hgel/AgNPs-3MPS	12.6 ± 2.6	0.4±0.09

Overall, all samples demonstrated good stability, accounting for a weight loss of approximately 10% after 1 month. The reported values of weight loss percentage (ΔW%) and degradation rate (T) of the analyzed composites do not differ much from those obtained for the native hydrogel. Therefore, it is possible to state that the in situ synthesis of AgNPs, both through the use of $NaBH_4$ and glucose, does not significantly compromise the stability of the peptide hydrogel in physiological conditions.

To test the antibacterial effects of silver and the application of these nanocomposites in the biomedical field, it was decided to carry out in vitro inhibition tests against *S. aureus*, which is a major human pathogen and the most common Gram-positive bacteria isolated from skin ulcers[191].
The tests were carried out on the hgel/AgNPs composites made with the three different synthesis strategies and with a Ag concentration equal to 0.094 mg/mL. In addition, the three types of AgNPs in solution with [Ag] = 0.094 mg/mL and the hydrogel as it is in the absence of AgNPs were tested as controls. A viability test was then carried out on S. aureus in the presence of these biomaterials at different concentrations to determine the MIC (minimum inhibitory concentration). It was evidenced that the hydrogel exhibited limited antibacterial activity even in the absence of AgNPs. Indeed, it is known that the peptides of which it is made up have antimicrobial properties[8]. In particular, the hydrogel was effective against S. aureus at the following concentrations: Fmoc-Phe: 0.9 mg/mL, Phe2: 0.725 mg/mL, and Fmoc-Phe3: 0.7 mg/mL. The results of the microbiological analyzes obtained for the AgNPs in solution and for the hgel/AgNPs composites prepared under the different experimental conditions are reported in **Table 2.3**.

Table 2.3. Minimum inhibitory concentration (MIC) for S. aureus ATCC 25923 for AgNPs in solution and hgel/AgNPs samples.

Sample	Reducing agent	MIC (mg/mL)
AgNPs-3MPS	$NaBH_4$	0.008
Hgel/AgNPs-3MPS	$NaBH_4$	0.006
AgNPs-SDS	β-D-glucose	0.004
Hgel/AgNPs-SDS	β-D-glucose	0.006

Comparing the MIC data, it can be seen that there are no substantial differences either with the variation in the synthesis technique of AgNPs (using $NaBH_4$ or β-D-glucose) or as a function of sample type (AgNPs colloidal suspension or hgel/AgNPs composites). In each of the analyzed cases, the MIC ranged between 0.004 and 0.008 mg/mL. Such values are comparable with those reported in the literature for similar systems. Thus, all the systems studied are promising candidates for treating S. aureus infections[192]. In particular, hgel/AgNPs samples have the advantage of being able to release silver ions in a controlled way over time; therefore, the bacteria, in the presence of these composites, will be subjected to the antimicrobial agent for a prolonged time and the duration of the antibacterial effect will be greater. Moreover, the green synthesis we propose, which uses glucose as a reducing agent, avoids the use of chemicals that could represent a biological risk.

2.2. Synthesis of the hydrogels containing TiO_2NPs with antibacterial properties

Asantibacterial agents, titania nanoparticles (TiO_2NPs) are attracting growing interest due to their chemical stability, biocompatibility and proven antibacterial properties. Due to its effective antibacterial activity against both Gram-negative and Gram-positive bacteria, In this part, the

encapsulation of commercial TiO_2NPs within self-assembling tripeptide hydrogels to form hgel-TiO_2NP composites with significant photo antibacterial properties is reported. Two different concentrations of TiO_2NPs were used to investigate the ability of peptide hydrogels to disperse and stabilize them and also to investigate the effect of concentration on gel parameters such as fibrillary structure, rheological properties, and swelling ability (**Figure 2.14**). Ultrasonication was also applied to the samples and its effect on several physicochemical properties of the obtained hydrogels was investigated.

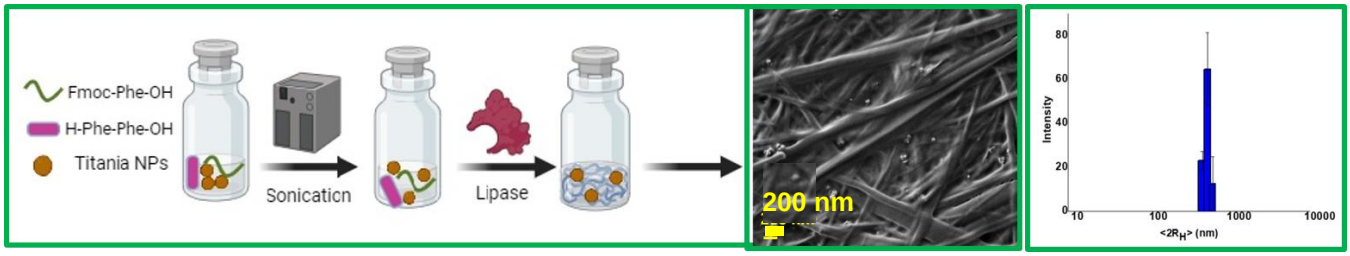

Figure 2.14. Schematic reperesentation of preparation of peptide hydrogel composites with different concentration of TiO_2NPs.

Field emission scanning electron microscopy (FESEM) studies were conducted to investigate the effect of sonication on the hydrogel fibrillary structures, as well as the dispersion of different amounts of TiO_2NPs inside the hydrogels. **Figure 2.15(A–C)** show the fibrillar structure of hgel-TiO_2NPs (5 mg) and hgel-TiO_2NPs (10 mg) before applying sonication, respectively. As evident, TiO_2NPs showed aggregation in both concentrations inside the gel. At the same time, after sonication (**Figure 2.15(E,F)**), they were finely dispersed without any aggregation, which reveals the effect of sonication on NP dispersion. It is also interesting to mention that sonication did not affect the fibrillar structure of hgel (**Figure 2.15D**) and hgel-TiO_2NPs.

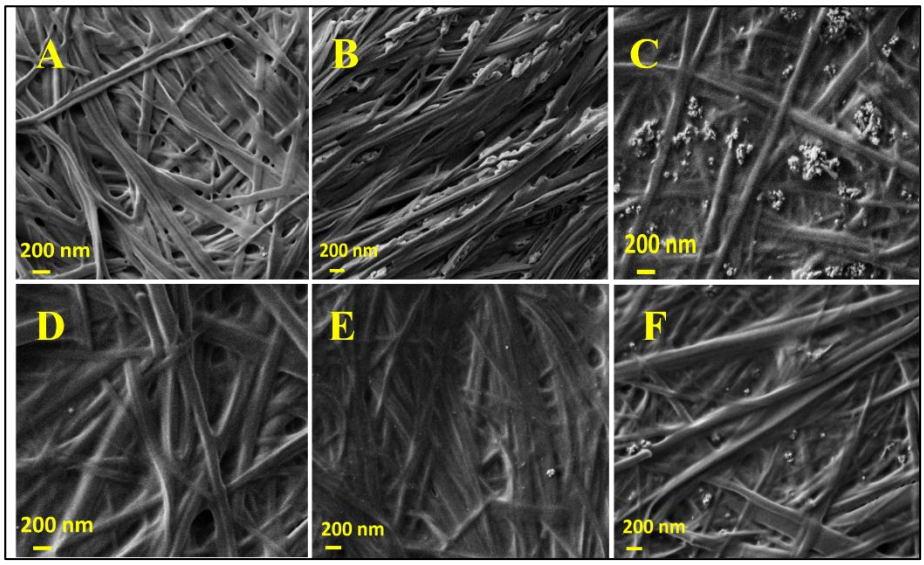

Figure 2.15. SEM images of: (**A**) hgel, (**B**) hgel-TiO_2NPs(5 mg), (**C**) hgel-TiO_2NPs(10 mg) in the absence of sonication and (**D**) hgel, (**E**) hgel-TiO_2NPs(5 mg), (**F**) hgel-TiO_2NPs(10 mg) with sonication.

DLS measurements were performed to evaluate the size and polydispersity of TiO_2NPs once they were inserted inside the hydrogels and evaluate if they underwent aggregation. Figure 2A,B show the size distribution of hgel-TiO_2NP composites containing different amounts of TiO_2NPs (5 mg and 10 mg, respectively), prepared without sonication. The average diameters measured for these samples were 396 ± 50 nm and 712 ± 84 nm, respectively. However, after sonication (**Figure 2.16(C,D)**) the particle size decreased (255 ± 33 nm and 531 ± 45 nm, respectively), demonstrating the positive effect of sonication on the dispersion of particles, which is consistent with SEM data.

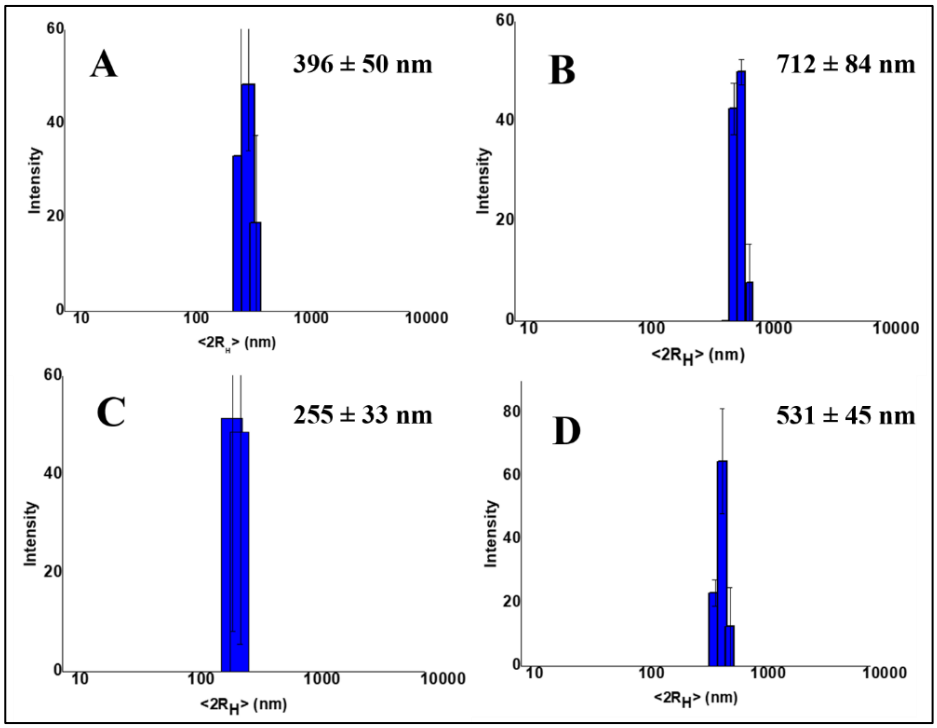

Figure 2.16. Size distributions of (**A**) hgel-TiO_2 (5 mg); (**B**) hgel-TiO_2 (10 mg); (**C**) hgel-TiO_2 (5 mg)-s; (**D**) hgel-TiO_2 (10 mg)-s ("s" represents sonication).

SAXS profiles were collected to study the structural features within 1-100 nm scale of hgel and hgel-TiO_2NPs, both sonicated and non-sonicated and with different concentrations of TiO_2NPs. We can mention that the visual appearance of the samples results slightly inhomogeneous at a macroscopic (mm) scale, showing regions with more intense white color probably related to a higher local concentration of TiO_2NPs; for SAXS data collection we sample 0.5 mm sized portions and therefore slight variations of signal can be considered due to this variability. All samples show isotropic scattering patterns even if the pre-formed gels were injected into borosilicate capillaries with a long needle syringe and then shaken to fill the bottom. The data of the pristine hydrogel (hgel, grey and black dots) show the profile of fibrillar structures, with characteristic cross-section radius of the cylinder-like fibrillar aggregates in the range of 2.5-8 nm. For $q < 0.2$ nm^{-1} the slope

deviates from the q^{-1} predicted for straight rod-like objects towards more negative values (close to –2) since the fibrils cannot be seen as individual rods anymore at larger length scales (> 10-20 nm) compared to their cross-sections. This could be interpreted as due to the branched fibrillar network, giving rise to a fractal structure with characteristic dimension close to 2.

As can be seen in **Figure 2.17A**, the SAXS profile obtained for the hgel-TiO_2NPs at low concentration is almost superimposable to that of the hydrogel sample in the q-range > 0.3 nm^{-1}, suggesting that the fibrillar cross section is not perturbed. A slightly higher scattering intensity can be appreciated for q < 0.3 nm^{-1}, with initial power law $q^{-1.77}$, compared to $q^{-1.63}$ observed for the pristine hgel obtained in the same conditions. When considering the composite sample with double the content of TiO_2 particles (hgel-TiO_2NPs (10 mg)), a very intense additional scattering signal with initial slope oscillations (maxima at q 0.125, 0.22 and 0.3 nm^{-1}) can be seen in the lower q. A comparison with the SAXS profile of the TiO_2NPs commercial powder clarifies that for the high concentration composite most of the signal can be attributed to the inorganic particles, which have an intrinsically much higher scattering power compared to the peptide hgel. The relative amount of this contribution seems not to be linearly related to the nominal volume fraction of TiO_2 added in the sample, since the scale factor for roughly reproducing the SAXS signal of the low concentration composite as a sum of the signals from hgel and TiO_2 particles should be only 0.04 times that of the high concentration composite, despite the TiO_2 amount should be only half. While at q > 0.3 nm^{-1} the SAXS data of the TiO_2NPs powder follows the Porod's power law decay (q^{-4}), indicating that the individual particles have a sharp interface when seen at a length-scale < 10-20 nm, the initial power law is close to $q^{-2.1}$. This suggests that the individual TiO_2 particles are clustered in mass fractals with fractal dimension 2.1. The pair distance distribution functions P(r) (**Figure 2.17C**) can help estimate the characteristic sizes that contribute to the SAXS profile of the TiO_2NPs, even if the overall size of the inorganic nanoparticle clusters is beyond the largest accessible distance of the SAXS experiment (> π/0.04 nm^{-1} ≈ 80 nm), as also perceived from the SEM micrographs. The P(r) functions present a main maximum around 30 nm, which is coherent with the approximate radius expected for the nanoparticles, but also contributions of distances around 12 nm and 60 nm can be seen. This might be due to two additional populations of particles and to a hierarchical structuring of the clusters made by particles with approximate diameter 25 and 60 nm organized in a non-compact aggregate. Diffraction peaks can also be observed in the scattering profiles of the composites (**Figure 2.17B**). While the intense peak at 17.8 nm^{-1} and the following one at 19.3 nm^{-1} are also found in the scattering pattern of the TiO_2NPs powder and are consistent with those expected for the anatase crystalline phase[152], additional peaks are observed for q < 17.8 nm^{-1} in the composites with highest TiO_2 content. These signals (peaks at q values 2.65, 3.63, 4.53, 6.21, 7.32,

14.64 nm^{-1}) suggest the presence of mesoscale ordered structures (lamellar, hexagonal phases) with characteristic spacings of the order of 2 nm, which cannot be found in dry TiO_2 powder but form in the composite hydrogel preparations.

As can be seen in **Figure 2.17(D,E)**, the data of both the pristine hydrogel and of the hgel-TiO_2NPs in both concentrations show overall the same profile when comparing non-sonicated vs. sonicated samples, indicating that sonication does not have any effect on the hydrogel structure neither appreciable effects on the composite at low concentration of TiO_2. For the high concentration hgel-TiO_2NPs, the sonicated sample shows less intense peaks in the q region 2-10 nm^{-1}, suggesting that the sonication procedure might affect the amount of the ordered mesophases formed.

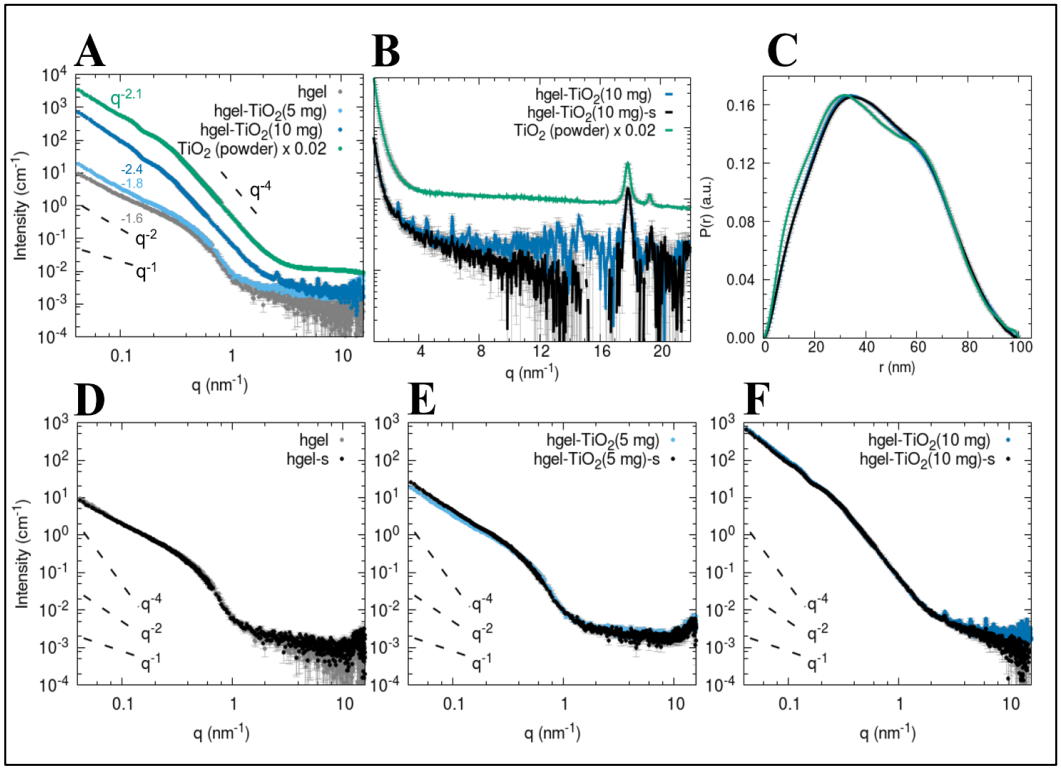

Figure 2.17. SAXS profiles of **A**) hgel (grey dots), hgel-TiO_2NPs (5 mg) (light blue dots), hgel-TiO_2NPs (10 mg) (blue dots), and of the TiO_2 powder (green dots). Characteristic power laws are reported for reference (black dashed lines), while the exponent observed at $q < 0.3$ nm^{-1} is reported in each case. **B**) Enlargement of the WAXS region of the scattering profile to highlight diffraction peaks for the samples hgel-TiO_2NPs (10 mg) (blue), hgel-TiO_2NPs(10 mg)-s (black), and TiO_2 powder (green). **C**) Pair distance distribution functions obtained from the SAXS data of the samples hgel-TiO_2NPs (10 mg), hgel-TiO_2NPs (10 mg)-s, and of the TiO_2 powder. Scaling factors were applied to match the height of the main maximum: 1.125 for hgel-TiO_2NPs (10 mg)-s and 0.0044 for TiO_2 powder. **D-F**) Comparison between the SAXS profiles of non-sonicated and sonicated samples.

This investigation aimed to unravel the effect of TiO_2NPs on the viscoelastic properties of the hydrogels, which are essential for their final application. As can be seen in **Figures 2.18(A,B**), all sonicated samples show higher G' (elastic modulus) and G" (viscous modulus) values in comparison to their non-sonicated counterparts (the only exception is for hgel-TiO_2NPs (5 mg), where G"

overlaps in both sonicated and non-sonicated samples) which show the effect of sonication in providing homogenized matrices and fibrillar structures that may increase the tensile strength of the hydrogels both in the presence and absence of NPs. Regarding **Figure 2.18B**, increasing the concentration of TiO_2NPs inside the hydrogel, the G' value rises, demonstrating the formation of further crosslinks leading to a stronger hydrogel.

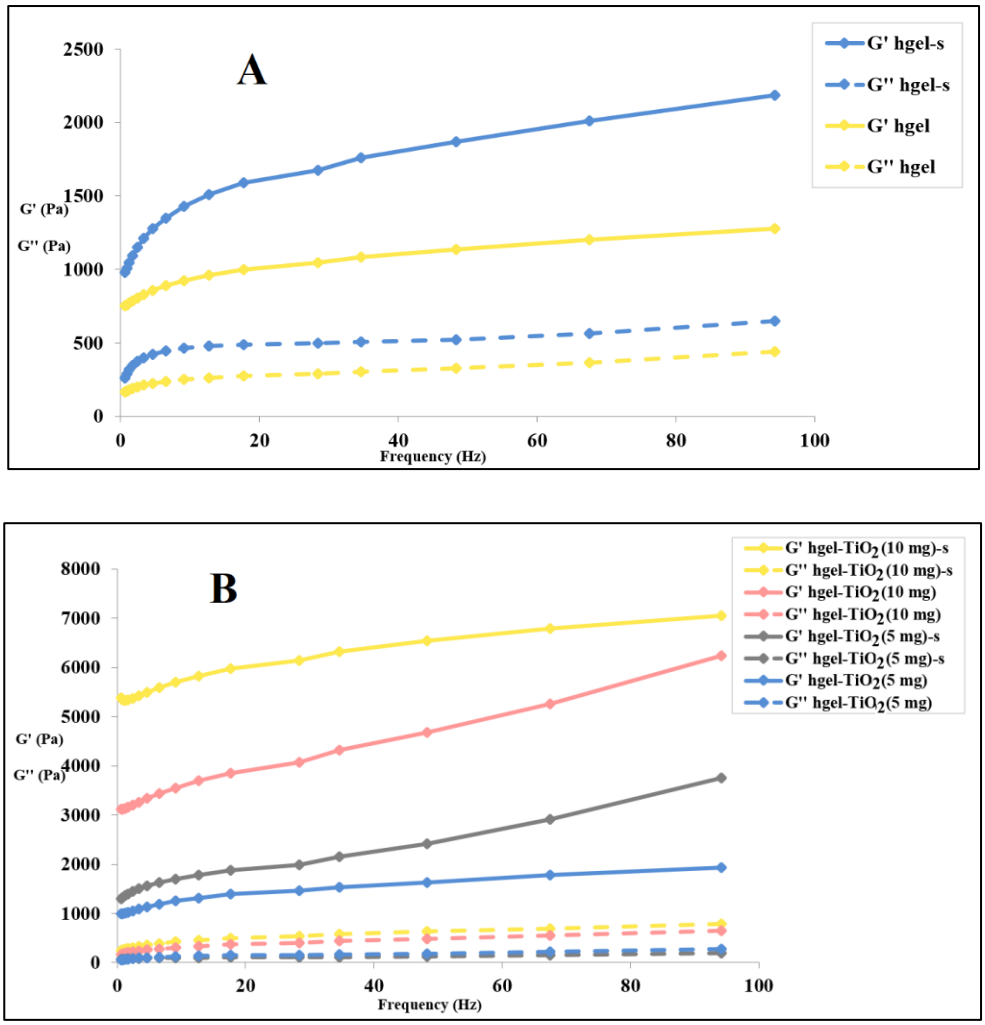

Figure 2.18. Frequency sweep of **A**) hydrogel prepared with or without sonication, **B**) hgel-TiO_2NPs with different concentrations of NPs prepared with or without sonication ("s" in the insets indicates sonication).

The swelling behaviors of the native hydrogel and hgel-TiO_2NPs were investigated. Different samples were prepared, with or without sonication, to determine the effect of this treatment on the swelling ability of the obtained hydrogel materials. As shown in **Figure 2.19**, the sonicated hydrogel showed a higher swelling degree than its non-sonicated counterpart, while for the hydrogel composites non-sonicated samples had the highest swelling degree. Overall, by increasing the concentration of TiO_2NPs, the swelling ability decreased (while the tensile strength increased in this condition), which may indicate that the presence of NPs provides cross-links and prevents water molecules from easily penetrating inside the matrix. For the case of sonicated samples, they showed even lower swelling degrees in comparison to non-sonicated ones. Probably, since

sonication leads to a higher dispersity of TiO_2NPs and a more homogeneous hydrogel matrix, such uniform hydrogel networks show higher tensile strength and consequently a lower swelling degree than non-sonicated ones. For hgel-TiO_2NPs (5 mg), there was an almost 10% decrease in swelling ability after sonication that doubled for ion that doubled for hgel-TiO_2NPs (10 mg).

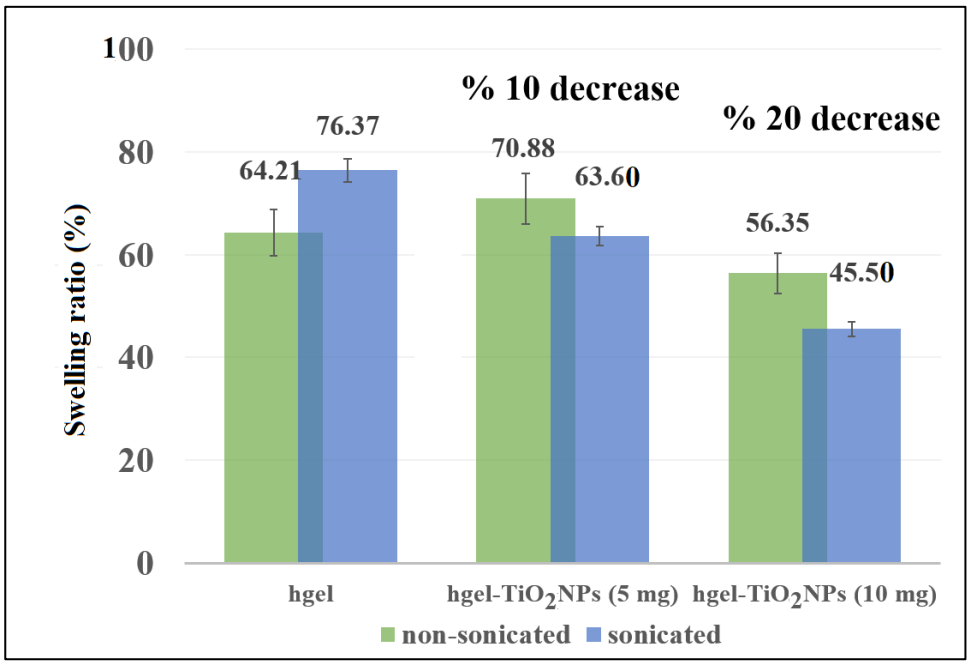

Figure 2.19. Swelling ratio of hgel, hgel-TiO_2NPs (5 mg) and hgel-TiO_2NPs (10 mg), prepared with or without sonication.

The antibacterial activity of the prepared TiO2 based hydrogel composites was investigated. MRSA represents a major antibiotic-resistant pathogen involved in tissue and medical-device-related infections[181]. TiO_2NPs have shown potential antimicrobial properties[182], so their antibacterial effect was tested on MRSA clinical isolates. To initially characterize the virulence of the bacterial isolates, antimicrobial susceptibility testing (AST) was performed for ceftaroline (CEF), daptomycin (DAP), erythromycin (ERY), fusidic acid (FUS), levofloxacin (LEV), linezolid (LIN), oxacillin (OXA), rifampicin (RIF), teicoplanin (TEI), tetracycline (TET), tigecycline (TIG), trimethoprim-sulfamethoxazole (TSX), and vancomycin (VAN). Notably, MRSA2 and MRSA25 showed resistance to 50% (6/12) and 33.3% (4/12) of the tested antibiotics, respectively. Conversely, the laboratory strain *S. aureus* 6583 (ATCC) was susceptible to all antibiotics (**Figure 2.20A**). Antibiotic-resistance genes were assessed for all clinical isolates (**Figure 2.20B**). The MRSA phenotype was confirmed by the presence of the *mecA* genes conferring resistance to oxacillin or ceftaroline. Resistance to macrolides and lincosamides was associated with erm(C) or erm(A). In MRSA2 and MRSA25, resistance to LEV was linked to the *gyrA* gene. Resistance to TSX and fusidic acid were associated with the *dfrC* (MRSA2) and fusA (MRSA25) genes, respectively (**Figure 2.20A**).

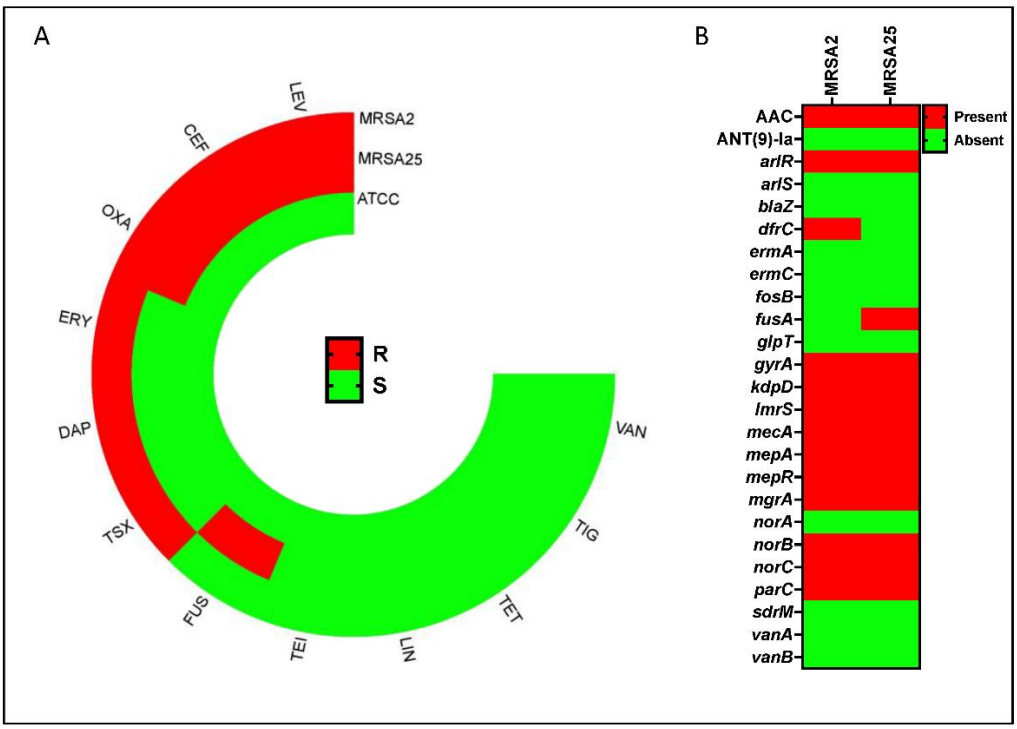

Figure 2.20. Antimicrobial resistance genes and antimicrobial susceptibility test. **A**) circular heatmap of antimicrobial susceptibility testing (AST) for the following antibiotics: ceftaroline (CEF), daptomycin (DAP), erythromycin (ERY), fusidic acid (FUS), levofloxacin (LEV), linezolid (LIN), oxacillin (OXA), teicoplanin (TEI), tetracycline (TET), tigecycline (TIG), trimethoprim-sulfamethoxazole (TSX), and vancomycin (VAN) expressed as resistant (red – R) or susceptible (green – S). **B**) Heatmap displaying antibiotic resistance genes found in the Methicillin-Resistant *S. aureus* (MRSA) strains (MRSA2 and MRSA25) and the laboratory *S. aureus* strain ATCC 6538 (ATCC).

A preliminary study determined the UV exposure time that wouldn't impact bacterial growth. *S. aureus* suspensions in nutrient broth were exposed to UV light at an intensity of 6.9 mW/cm^2 for 10, 5, and 3 minutes. Notably, a 10-minute exposure significantly reduced the growth of the MRSA25 strain (P = 0.037) compared to untreated controls. In contrast, 5 and 3-minute exposures did not impact *S. aureus* growth (**Figure 2.21**). Based on these results, a 5-minute UV exposure was selected as the optimal treatment for the photoactivation of TiO_2NPs.

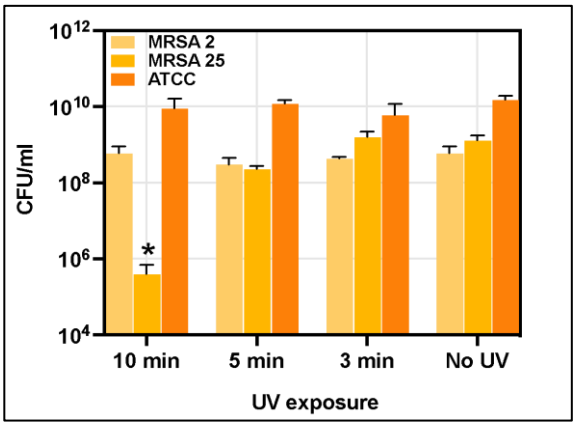

Figure 2.21. Effect of UV light at different exposure times on the growth curve of *S. aureus*. The graph represents 10 min, 5 min and 3 min UV exposure compared to unexposed cells. Each value corresponds to the mean of 3 replicates.

The error bars represent standard deviation. Statistical differences were determined using the Kruskal–Wallis test. *, P<0.05; **, P<0.01; ***, P<0.001.

The inhibitory effects of different concentrations (0.05, 0.1, 0.2, 0.4, 0.8 and 1.6 mg/mL) of TiO_2NPs and hgel-TiO_2NPs on *S. aureus* strains are shown in **Figure 2.22**. Specifically, after UV activation, *S. aureus* strains exposed to TiO_2NPs showed a more significant reduction in surviving cells than those in dark conditions across all tested concentrations (**Figure 2.22A**). Notably, bacterial cells exposed to TiO_2NPs in dark conditions showed an unexpected increase in CFU/mL compared to the untreated control cells (**Figure 2.22A**). In contrast, *S. aureus* bacterial cultures exhibited a marked concentration-dependent survival decrease in both photoactivated and non-photoactivated hgel-TiO_2NPs (**Figure 2.22B**). It is worth noting that at the lower tested concentration (0.05 mg/mL), photoactivated hgel-TiO_2NPs resulted in a significant (P = 0.026) reduction in CFU/mL compared to dark conditions. Comparative analysis revealed that hgel-TiO_2NPs significantly reduced *S. aureus* survival compared to TiO_2NPs, both in the dark (**Figure 2.22C**) and photoactivated (**Figure 2.22D**) conditions, across all tested concentrations.

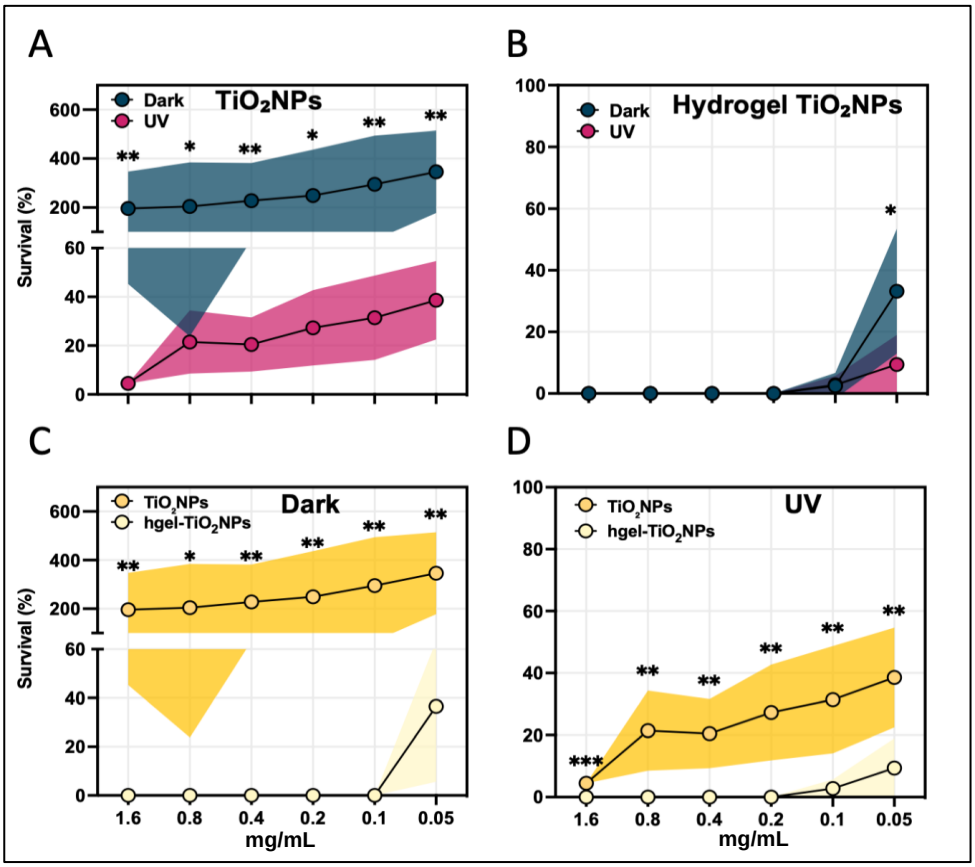

Figure 2.22. Antibacterial activity of photoactivated (UV light) and non-photoactivated (Dark) **A**) TiO_2NPs and **B**) hgel-TiO_2NPs at different concentrations of TiO_2 (0.05, 0.1, 0.2, 0.4, 0.8, and 1.6 mg/mL). Comparative analysis of antibacterial activity for TiO_2NPs and hgel-TiO_2NPs in the dark **C**) or in the presence of UV **D**). Values are expressed as a percentage of survival of treated cells compared to the untreated controls. Data points and the corresponding shaded areas represent the mean ± standard deviation from three independent experiments, each analyzed in triplicate. Statistical differences were determined using the Mann-Whitney test. *, P<0.05; **, P<0.01; ***, P<0.001.

The impact of non-photoactivated TiO_2NPs and hgel-TiO_2NPs on the metabolic activity of S. aureus was evaluated at different TiO_2NPs concentrations (0.05, 0.1, 0.2, 0.4, 0.8 and 1.6 mg/mL). This was determined by monitoring the production of fluorescent resorufin (7-hydroxy-3H-phenoxazin-3-one) over a 1200 min period, as depicted in **Figure 2.23**. When exposed to nonphotoactivated TiO_2NPs, S. aureus isolates exhibited a concentration-dependent increase in their metabolic activity (**Figure 2.23A**). This result supports the previous observations of increased bacterial growth in the presence of non-photoactivated TiO_2NPs. Conversely, the response to non-photoactivated hgel-TiO_2NPs remained consistently low across most concentrations, except for 0.05 mg/mL (**Figure 2.23B**). This finding aligns with a plate count assay that indicated partial bacterial growth at the hgel-TiO_2NP concentration of 0.05 mg/mL.

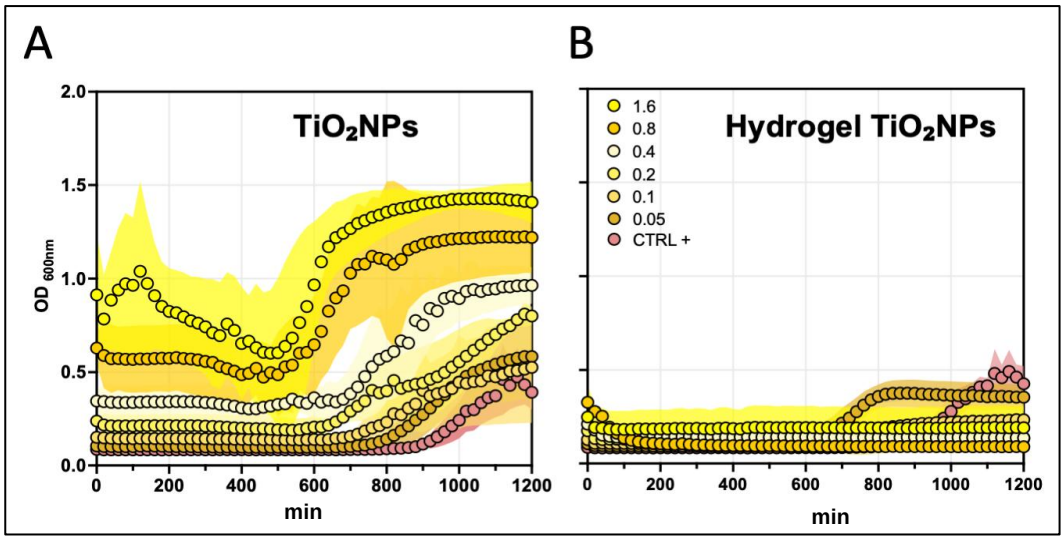

Figure 2.23. Metabolic activity of S. aureus strains in response to varying concentrations of TiO_2NPs (0.05, 0.1, 0.2, 0.4, 0.8, and 1.6 mg/mL) using both non-photoactivated **A**) TiO_2NPs and **B**) hgel-TiO_2NPs, assessed by resazurin-to-resorufin conversion after 1,200 minutes of incubation. Data points and the corresponding shaded areas represent the mean ± standard deviation Data represent the means ± standard errors from two independent experiments, each analyzed in duplicate.

The obtained results underpin the importance of understanding environmental influences when considering therapeutic NPs deployment. The observed influence of TiO_2NPs on *S. aureus* growth, specifically the unexpected rise in bacterial growth in non-photoactivated TiO_2NPs conditions, resonate with findings from a previous study where HeLa cells exposed to low concentrations of TiO_2NPs exhibited heightened sensitivity to *S. aureus* infections[183]. This alignment with previous studies underscores a potentially complex interplay between TiO_2NPs and bacterial growth dynamics, dependent on the specific conditions and cellular context. Adding to this concern is the widespread use of TiO_2NPs in cosmetics, that has raised safety concerns[184].

The efficacy of hgel-TiO_2NPs in diminishing *S. aureus* populations, regardless of photoactivation, is another crucial observation. This concentration-driven effect demonstrates that hgel-TiO_2NPs have intrinsic anti-staphylococcal properties that can act independently of light exposure, a finding

consistent with the broader understanding of NPs interactions with bacteria[194,185]. Furthermore, when combined with photoactivation, hgel-TiO_2NPs displayed augmented antibacterial activity, even at suboptimal concentrations like 0.05 mg/mL. This interplay between NPs concentration and UV light exposure has been explored previously, reinforcing the role of UV light in enhancing NP-based antimicrobial strategies[186]. The present study also offers insightful revelations into how non-photoactivated TiO_2NPs and hgel-TiO_2NPs distinctly influence the metabolic activity of *S. aureus*. The concentration-dependent growth associated with TiO_2NPs suggests that non-photoactivated TiO_2NPs might enhance bacterial metabolic activity. While supported by the data, this assertion necessitates further investigations to ascertain the underlying mechanisms.

2.3. Preparation of the hydrogel composites for water remediation

Co-precipitation is known as a simple and cheap method to synthesize magnetic iron oxide NPs (γ-Fe_2O_3NPs) from aqueous solutions of Fe(II) and Fe(III) by the addition of a base as a precipitating agent at mild temperature, and a large amount of NPs can be prepared by this method. The co-precipitation process, schematized in **Figure 2.24a**, does not require organic solvents or toxic precursor iron complexes and proceeds at temperatures below 100°C. More importantly, it can be developed and scaled up from lab to industry due to its simplicity, reproducibility, and eco-friendly reaction conditions. However, this method sometimes suffers from a lack of control over particle size distribution, probably because of the complicated set of pathways that lead to the formation of NPs.[187] The general mechanism for the formation of MNPs first involves hydroxylation of the ferrous and ferric ions to form $Fe(OH)_2$ and $Fe(OH)_3$, respectively. These two low-soluble hydroxides (K_{sp} (25 °C) = 7.9×10^{-15} and 6.3×10^{-38}, for ferrous and ferric hydroxide, respectively)[188] can be obtained at alkaline pHs (pH > 8), and when NaOH is used as the precipitating agent, a black colloidal solution of iron containing NPs is formed instantaneously. By applying a 2:1 molar ratio of Fe(III):Fe(II) and an oxygen-free environment, magnetite NPs (Fe_3O_4NPs) are the main product of this reaction through the following possible reactions (**equations 1-4**):

$$Fe(III) + 3OH^- \rightarrow Fe(OH)_3 \quad (1)$$

$$Fe(OH)_3 \rightarrow FeOOH + H_2O \quad (2)$$

$$Fe(II) + 2OH^- \rightarrow Fe(OH)_2 \quad (3)$$

$$2FeOOH + Fe(OH)_2 \rightarrow Fe_3O_4NPs\downarrow + 2H_2 \quad (4)$$

Magnetite shows an inverse (or normal) spinel crystal structure, and its unit cell contains 32 O^{2-} anions, 8 Fe(II), and 16 Fe(III) cations. Due to the presence of reduced iron (Fe(II)) in this crystal

structure, Fe_3O_4NPs are easily subject to oxidation and are transformed to a more stable maghemite phase (γ-Fe_2O_3NPs) by the following equation (**Equation 5**)[189]:

$$3Fe_3O_4NPs + 0.5O_2 + 2H^+ \rightarrow 4\gamma\text{-}Fe^{III}{}_2O_3NPs + Fe(II) + H_2O \quad (5)$$

Another important aspect of iron-based NPs is their colloidal stability after the synthesis. Due to their magnetic properties, iron-based NPs are more vulnerable to agglomeration because of the magnetic attraction among particles. In general, colloidal stability is the result of a balance between repulsive interactions (steric and electrostatic) and attractive forces (Van der Waals, dipolar, and magnetic), which can be influenced by the medium parameters, including composition, pH, and ionic strength.[190] To enhance their colloidal stability, MNPs should be stabilized by steric, electrostatic, or a combination of these repulsive forces. In the electrostatic stabilization, the repulsive forces between the NPs originate from likewise charges,[191] and for the steric stabilization, the presence of large molecules provides a repulsive hindrance for the surface of NPs. Steric stabilization is usually favored because it is less sensitive to medium parameters and therefore more suitable when MNPs are in contact with complex media.[192,193,194] To this aim, several small and large stabilizing agents have been applied for the surface functionalization of MNPs, such as polymers (polytrolox ester, PAA, and polyacrylic-co-maleic acid), natural antioxidants (green tea polyphenols, curcumin, quercetin, and anthocyanins) and organic or inorganic acids (gallic, ascorbic, citric, and humic acid).[195] Among these stabilizers, the functionalization of magnetic NPs with PAA provides both steric and electrostatic effects on the NPs' surface.[196] The electrostatic effect of PAA originates from its carboxylate groups, and the steric effect from its polymeric nature. For water purification applications, PAA is known for its ability to absorb a large amount of water and is used as a superabsorbent. Another advantage of PAA is its biocompatibility which is highly desirable. For the PAA functionalization of NPs, two methods are generally used: *in situ* and post (*ex situ*) surface coating. For in situ functionalization, PAA is used simultaneously with the iron precursors during the synthesis of magnetic NPs, and both synthesis and functionalization occur simultaneously in one step. For the post (*ex situ*) method, PAA is added to pre-synthesized NPs in a separate step (next step) from the synthesis. Generally, the *in situ* method is more preferable due to the inhibition of particle growth in a high concentration of PAA. Also, the high hydrophilicity and colloidal stability induced by PAA stabilization of magnetic NPs can decrease the long gelation time of supramolecular magnetogels. For instance, it was reported that the stabilization of iron oxide NPs with polyacrylic acid allowed homogeneous encapsulation of NPs up to 30 m/m% in both Npx-L-Asp-Z-ΔPhe-OH and Npx-L-Tyr-Z-ΔPhe-OH hydrogels containing non-canonical amino acids. These are some important benefits of PAA for its applications as composite adsorbents. For instance, PAA-functionalized magnetic magnetite particles have been used as an

adsorbent for basic dyes.[197,198] For the above reasons, we synthesized the magnetic NPs stabilized by PAA using the in situ strategy to obtain small and colloidally stable γ-Fe_2O_3NPs, followed by preparation of γ-Fe_2O_3NPs@HG magnetogel. The mximum yield% of the γ-Fe_2O_3NPs formation was found to be 55%.

The isolation of γ-Fe_2O_3NPs was first confirmed by the visual magnetic behavior of the purified precipitates. As can be seen in **Figures 2.24b** and **S5**, the particles are strongly attracted to the external magnet and easily redispersed after removing the magnet. To confirm the stabilizing effect of PAA, uncoated magnetic NPs were also synthesized, using the same reaction conditions but without the presence of PAA. For the synthesis of γ-Fe_2O_3NPs@HG magnetogels, we have used the blending strategy mentioned in the introduction section as a well-known method to synthesize magnetogels.[152] This method is based on sequential syntheses of the components, starting with the magnetic NPs, which are then blended with hydrogel precursors to make the resulting magnetogels. The formation of the hydrogel followed a well-assessed procedure, using a microbial lipase to catalyze the synthesis in water of self-assembling peptides generated by the peptide bond formation between 9-fluorenylmethoxycarbonyl-phenylalanine (Fmoc-Phe) and the dipeptide diphenylalanine (Phe_2) (**Figure 2.24c**).[199]

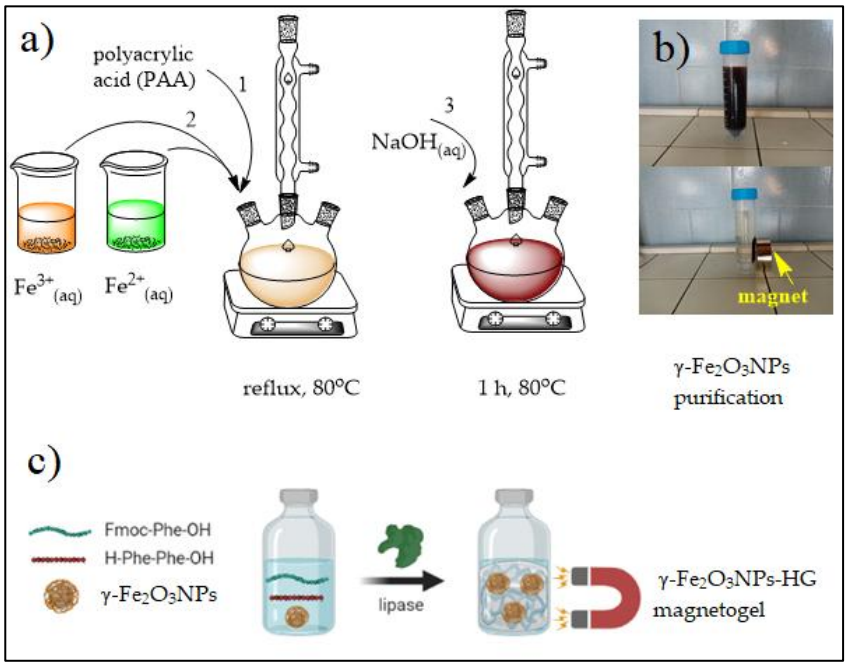

Figure 2.24. a) Schematic *in situ* synthesis and purification of PAA stabilized γ-Fe_2O_3NPs; b) separation of γ-Fe_2O_3NPs with an external magnetic field; c) illustration of the *ex situ* incorporation of γ-Fe_2O_3NPs into the peptide-based hydrogels γ-Fe_2O_3NPs@HG (blending method).

Fourier transform-infrared (FT-IR) and Raman spectroscopies are two commonly used techniques to characterize iron oxide nanoparticles, as they can provide information on the oxide phase through

detection of phonon modes.[200] The FT-IR spectra of bare and PAA-stabilized γ-Fe_2O_3NPs are presented in **Figure 2.25a** in the 1000–400 cm^{-1} region, containing information about the phase of both NPs. Based on literature, the magnetite phase has a sharp and symmetrical vibration at around 571 cm^{-1}, assigned to the Fe–O bonds present in tetrahedral and octahedral sites of the spinel structure. It is a general characteristic band of iron oxide NPs, and its sharpness clarifies the pure defect-free phase. In maghemite, this band splits into two characteristic vibrations, due to the creation of vacancy defects and vanishing of Fe(II) ion from the octahedral sites upon the formation of γ-Fe_2O_3, causing a decrease in Fe–O bond length, and hence, corresponding splitting of the band occurs.[201] It should be mentioned that both phases (magnetite or maghemite) show a weak band in the 440–460 cm^{-1} region. Regarding the crystal structure, also group theory theoretically predicts that if the γ-Fe_2O_3NPs have a spinel crystal, then there are four T_1 modes expected at 212, 362, 440, and 553 cm^{-1},[202] of which we were able to only detect the highest two frequencies with our experimental setup. Both spectra of γ-Fe_2O_3NPs clearly show the two T_1 modes around 460 and 570 cm^{-1} for uncoated γ-Fe_2O_3NPs, and 462 and 565 cm^{-1} for the PAA stabilized γ-Fe_2O_3NPs, confirming a spinel crystal structure for both NPs of our experiment. Hence, in both spectra, the formation of γ-Fe_2O_3NPs was confirmed from the broadening and splitting of the band into 628 and 570 cm^{-1} for uncoated γ-Fe_2O_3NPs, and 626 and 565 cm^{-1} for PAA-stabilized γ-Fe_2O_3NPs. Regarding the PAA coating and its interaction with the surface of NPs, the FT-ATR data are shown in **Figure 2.26b** for PAA-stabilized γ-Fe_2O_3NPs (red line) and pristine PAA (black line) in the 4000–600 cm^{-1} region. The FT-ATR spectrum of PAA stabilized γ-Fe_2O_3NPs is not a simple superposition of the PAA spectrum, and the relative intensities of the main vibrational bands show some changes, which suggests that PAA alters its symmetry when it attaches to the NPs. The main features of these spectra are summarized in **Table 2.4**, which shows the characteristic frequencies of free PAA, including the carbonyl stretching (−C=O) at 1669 cm^{-1}, $-CH_2$ scissoring at 1446 cm^{-1}, and the −C−O stretching at 1236 cm^{-1}, as well as the symmetric stretching frequencies of the carboxylate ions ($-COO^-$) at 1402 cm^{-1}. Compared to the PAA spectrum, the PAA-stabilized γ-Fe_2O_3NPs spectrum shows all these characteristic bands (except –C–O stretching) with a maximum of 6 cm^{-1} shift. There is also an additional band for the PAA-stabilized γ-Fe_2O_3NPs at around 1556 cm^{-1}, assigned to $-COO^-$ asymmetric stretching. These results confirm the surface functionalization of NPs with PAA, and based on the small shifts observed in frequencies of PAA-stabilized γ-Fe_2O_3NPs (compared to the PAA spectrum), a physical interaction can be proposed between the negatively charged PAA ($-COO^-$) and positive surface Fe(III) ions of NPs.[203]

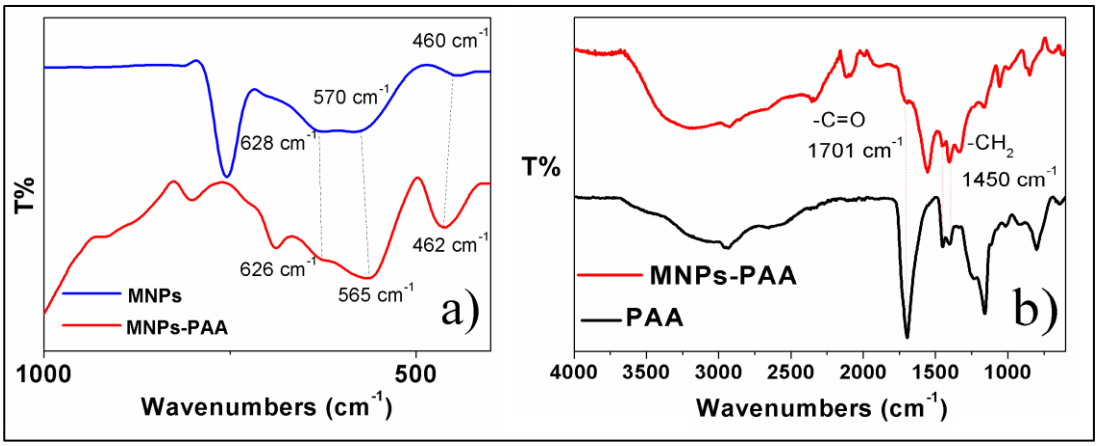

Figure 2.26. a) FT-IR spectra of uncoated γ-Fe_2O_3NPs NPs (blue line) and PAA stabilized γ-Fe_2O_3NPs (red line); b) FT-ATR of PAA stabilized γ-Fe_2O_3NPs (red line) and PAA (black line).[182]

Table 2.4. Comparison of FT-ATR peak assignments (in cm^{-1}) for polyacrylic acid (PAA) in solid form and after attachment onto the γ-Fe_2O_3NPs.

PAA	MNPs-PAA	peak assignment
1699	1705	–C=O (free COOH)
-	1556	$–COO^-$ (aymmetric)
1446	1444	$–CH_2$ scissor
1402	1408	$–COO^-$ (symmetric)
1236	-	–C–O

As mentioned above, Raman spectroscopy can discriminate iron oxide phases because they exhibit distinct Raman signatures originating from their different oxidation states.[204] Hence, Raman spectroscopy was used as a complementary technique to better understand the structure of the synthesized γ-Fe_2O_3NPs (in collaboration with Prof. Andrea Giacomo Marrani and Dr. Francesco Amato). The Raman spectra of the synthesized uncoated γ-Fe_2O_3NPs and PAA-coated γ-Fe_2O_3NPs are shown in **Figure 2.27(a,b)**, respectively. The results clearly match Raman spectra for maghemite previously reported in the literature,[205] with the three broad observed Raman active phonon modes at around 350 cm^{-1} (T_1), 500 cm^{-1} (E), and 700 cm^{-1} (A_1). Regarding the PAA-coated sample, we clearly see the Raman modes at higher wavenumbers, with two main bands centered at around 1400 and 2927 cm^{-1}, assigned to $–COO^-$ (symmetric) and –CH/$–CH_2$ stretching bands, respectively.[206] These results are in accordance with the FT-IR spectra and confirm the presence of maghemite phase for the PAA-coated γ-Fe_2O_3NPs.[207,208,209,210] The maghemite phase is also confirmed by XPS results (**Figure 2.28(c,d)**),[211,212,213,214,215] and the PAA-coated γ-Fe_2O_3NPs sample was analyzed with XPS in order to ascertain the chemical composition of the inorganic core structure. **Figure 2.29c** shows the XPS spectrum, where the signals due to ionization of Fe, C, O,

and Na are visible, the latter resulting from the use of NaOH in the synthesis of PAA-coated γ-Fe_2O_3NPs. Figure 3d shows the Fe 2p spectrum of PAA-coated γ-Fe_2O_3NPs, which is composed of two rather broad spin-orbit split components (j = 3/2 and 1/2), whose maxima are separated by a ΔE_{so} ~ 13.6 eV. This spectrum was curve-fitted in order to determine the oxidation state of the iron species. The curve-fitting procedure was conducted following the work by Grosvenor et al.,[250] who applied a Shirley background removal to the 2p3/2 envelope and successfully used the Gupta and Sen (GS) multiplets calculated for free metal ions, to account for electrostatic interactions in high-spin Fe(II) and Fe(III) compounds. Also in the present case, a five-fold GS multiplet for Fe(III) compounds was used in the curve-fitting (green curves in **Figure 2.29d**, first component at 710.05 eV binding energy), achieving a good match with the experimental data. This agreement strongly supports the attribution of this signal to γ-Fe_2O_3, as reported by Grosvenor et al. A further two-fold multiplet was added at low binding energy (red curves in **Figure 2.29d**, first component at 708.17 eV binding energy), in order to better reproduce the experimental signal. This multiplet appears also in the spectrum by Grosvenor et al. as a "pre-peak" and might stem from residual Fe(II) high-spin components possibly present in γ-Fe_2O_3.

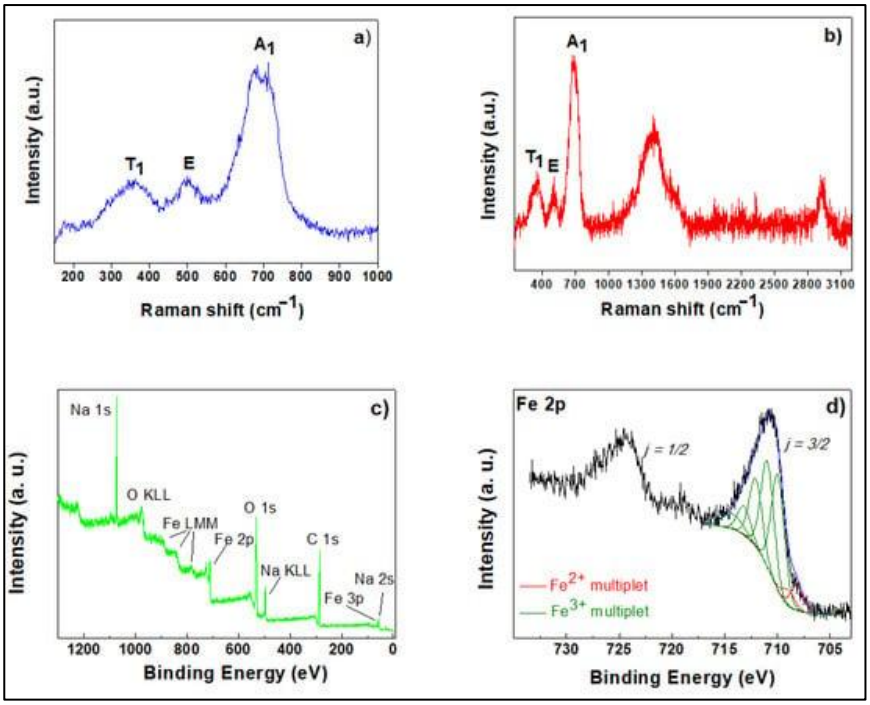

Figure 2.29. a) Raman spectra of uncoated γ-Fe_2O_3NPs; and b) PAA coated γ-Fe_2O_3NPs; c) XPS survey spectrum of PAA coated γ-Fe_2O_3NPs; d) XPS Fe 2p spectrum of PAA coated γ-Fe_2O_3NPs[182].

The hydrodynamic size and surface charges of the two γ-Fe_2O_3NPs systems (bare and coated with PAA) were studied by DLS and ζ-potential techniques (**Figure 2.30(a,b)**). Compared to uncoated γ-Fe_2O_3NPs, PAA-coated γ-Fe_2O_3NPs show smaller size and higher negative surface charge, which can be a good indication of PAA coating and, more importantly, PAA's stabilizing effect on the

NPs. Using PAA in the in situ synthesis of NPs allows for controlling the size of γ-Fe_2O_3NPs because the attached PAA moiety provides steric (by its polymeric nature) and electrostatic (by its $–COO^–$ group) stabilizations, thus permitting γ-Fe_2O_3NPs dispersion in aqueous media. In fact, the presence of PAA on the surface of γ-Fe_2O_3NPs prolongs the colloidal stability by slowing down the agglomeration process. Another major advantage of PAA is that the carboxylic acid-enriched surfaces of PAA-coated γ-Fe_2O_3NPs may provide a platform for attaching these NPs to other systems to prepare multifunctional nanohybrids. UV-Vis spectra of PAA-coated γ-Fe_2O_3NPs (1.6–0.005 mg/mL) were monitored over a 7-day period to characterize their colloidal stability against agglomeration and sedimentation.[216,217,218] As can be seen in **Figure 2.30c**, results show no significant changes in the intensities, indicating the stability of the preparations against aggregation. The images of three PAA-coated γ-Fe_2O_3NPs suspensions (1.6, 0.16, and 0.08 mg/mL) are shown in **Figure S6(a,b)**, in which no precipitation was observed, consistent with the UV-Vis spectra (**Figure 2.30c**). Also, the colloidal stability of higher concentrations of PAA-coated γ-Fe_2O_3NPs (10 mg/mL) was visually monitored over one week, and a remarkable stability of the NPs against sedimentation was observed. Conversely, uncoated γ-Fe_2O_3NPs showed a fast aggregation and sedimentation that were visually detected, even at low concentrations (**Figure S6c**). These results are consistent with previous studies on the use of organic molecules as stabilizing agents for MNPs. However, the uncoated NPs showed a limited amount of precipitation in the vials, demonstrating the positive long-term stabilizing effect of PAA-coated γ-Fe_2O_3NPs (**Figure 2.30c**). These results are comparable and consistent with the literature about the stabilizing effect of PAA on γ-Fe_2O_3NPs.

The UV-Vis spectra of both NPs systems show the presence of a new absorption band at around 355 nm (**Figure 2.30d**), which is different compared to the spectra of precursors ions ($Fe^{2+}_{(aq)}$ and $Fe^{3+}_{(aq)}$) and assigned to the band gap of maghemite derived from O(2p) → Fe(3d) transitions.[219,220,221,222,223] In the freshly prepared samples of both NPs, shoulder peaks centered at around 450 nm are observed due to the presence of a minor amount of Fe_3O_4NPs, which then oxidized to the maghemite phase, and are not seen in the results of previous section.

The peaks of $Fe^{3+}_{(aq)}$ and $Fe^{2+}_{(aq)}$ are assigned to charge-transfer electronic transition in octahedral acqua complexes.[182] Regarding these UV-Vis spectra of the $Fe^{3+}_{(aq)}/Fe^{2+}_{(aq)}$, it is worthy to explain that their electronic transition is largely governed by their d-electron configuration. The charge-transfer transitions are both spin- and Laporte-allowed and occur in the UV region, which is closely related to the strength of the applied ligand field (10D*q*).[224]

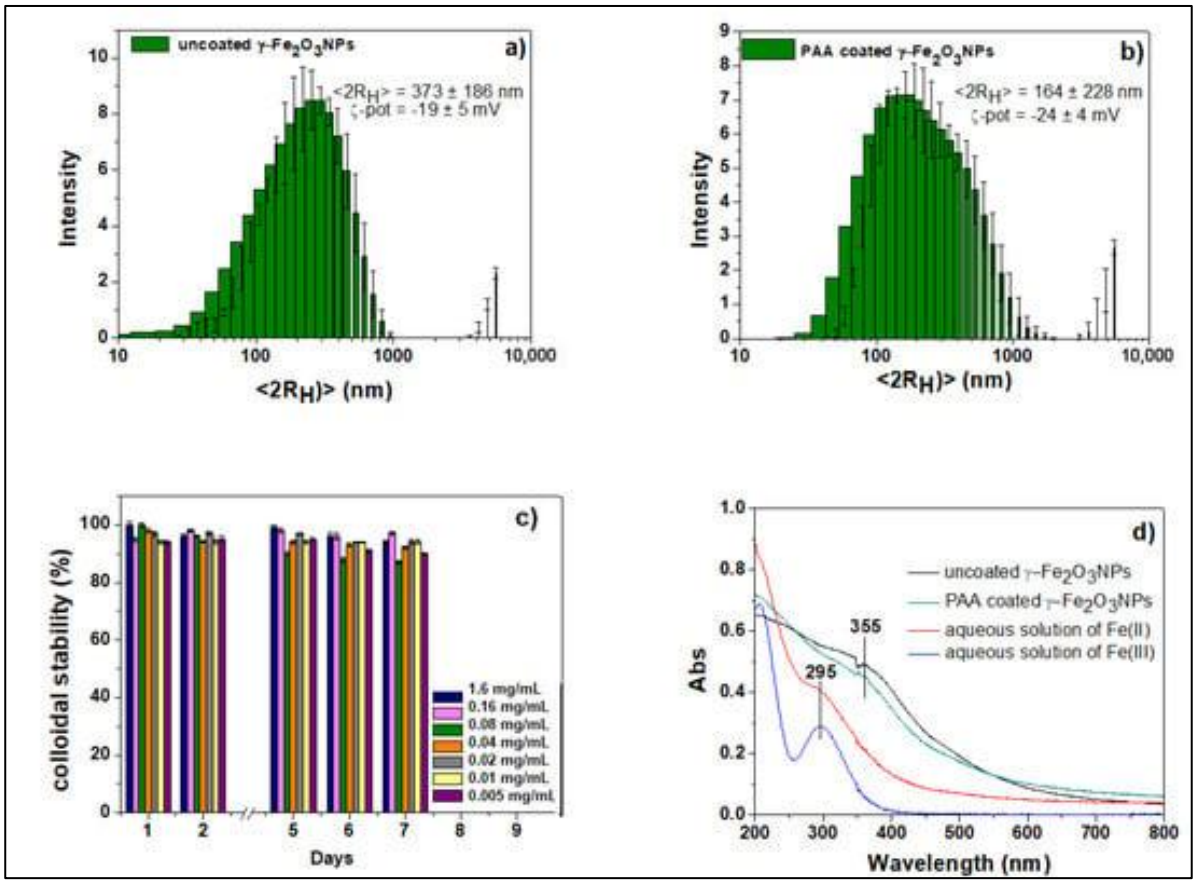

Figure 2.30. a,b) DLS results of the two bare and PAA-coated γ-Fe_2O_3NPs; **c**) stability tests of PAA-coated γ-Fe_2O_3NPs assessed by following the maximum absorption peak at 355 nm; **d**) UV-Vis spectra of freshly prepared precursors ions ($Fe^{2+}_{(aq)}$ and $Fe^{3+}_{(aq)}$) and the two NPs.

The solid-state morphology and size of the γ-Fe_2O_3NPs were evaluated using Field Emission Scanning Electron Microscopy (FESEM) (**Figure 2.31(a,b)**). The FESEM image of uncoated γ-Fe_2O_3NPs demonstrates a grain-like morphology with a size range of 15–65 nm (**Figure 2.31(a,c)**), and a little aggregation is detected in the image. In agreement with DLS results, the FESEM images of PAA-coated γ-Fe_2O_3NPs show smaller particles (**Figure 2.31(b,d)**, 10–40 nm). This result is consistent with the general mechanism of γ-Fe_2O_3NPs formation including a nucleation step in the beginning of co-precipitation, followed by nuclei growth and coalescence. This mechanism is supported by our results, in which both DLS and FESEM analyses indicate that the γ-Fe_2O_3NPs obtained without PAA have a larger average size compared to the particles in the presence of PAA. EDS elemental analyses showed the presence of C element, which is due to the presence of PAA, previously confirmed by the FT-IR/ATR and Raman results (**Figure S7**). For both γ-Fe_2O_3NPs (with and without PAA), we see smaller distribution particles, compared with the DLS results, relating to the differences between these two techniques. In fact, FESEM probes the electron-rich part of the particle in the solid state; then only the inner core can be seen, and the result obtained would be smaller. On the other hand, the DLS measures a hydrodynamic diameter based on the

diffusion of the particles in the solutions, and in most cases, we see larger nanoparticles due to the hydrodynamic layer. FESEM images of the hydrogel and magnetogel are shown in **Figure 2.31(e,f)**, both exhibiting the typical fibrillar structure, suggesting that the presence of PAA-coated γ-Fe_2O_3NPs does not change the macromolecular structure of the gel. Also, the small particles seen in the magnetogel image can be assigned to γ-Fe_2O_3NPs.

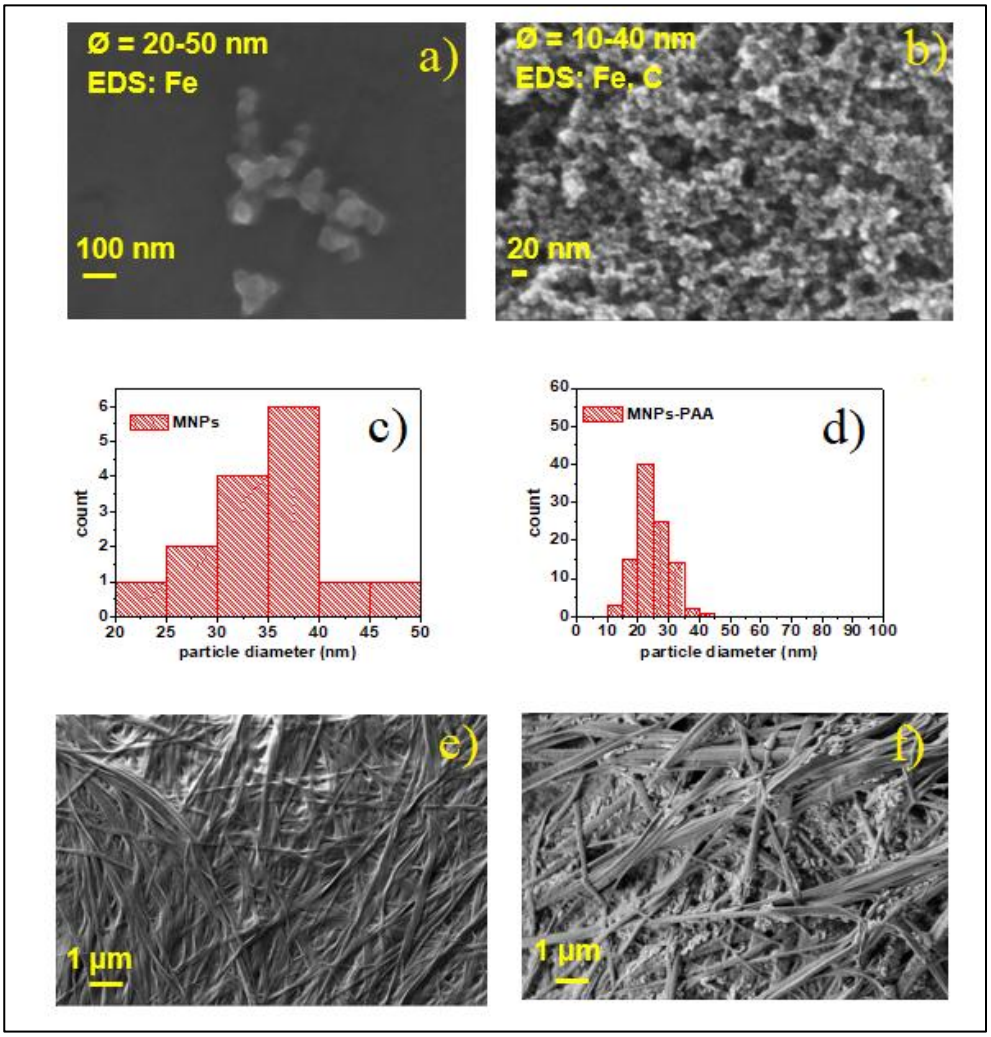

Figure 2.31. (**a**) FESEM results of uncoated γ-Fe_2O_3NPs and (**b**) PAA-coated γ-Fe_2O_3NPs; (**c**) size histogram of γ-Fe_2O_3NPs and (**d**) PAA-coated γ-Fe_2O_3NPs; (**e**) FESEM of peptide hydrogel alone and (**f**) γ-Fe_2O_3NPs@HG magnetogel. EDS data of PAA-coated γ-Fe_2O_3NPs are reported in the supporting section (Figure S7).

The viscoelastic behavior and the adsorption properties of hydrogel materials are tightly correlated properties. The goal of the rheological analyses was to understand how the presence of PAA-coated γ-Fe_2O_3NPs and their concentration could modulate the viscoelastic behavior of the hydrogels. As can be seen in **Figure 2.32**, for all systems, the experimental curves show a typical trend of a viscoelastic gel-like material, characterized by G' values much larger than G" values.[225] All the magnetogels showed lower mechanical strength compared to the hydrogel alone, and a concentration-dependent trend is observed for the magnetogels' mechanical strength, in which the highest concentration of γ-Fe_2O_3NPs (30 mg/mL) had the lowest storage modulus. The decrease in

the strength of the magnetogels may be due to the presence of PAA-coated γ-Fe_2O_3NPs with different sizes, morphologies, and surface charges. The negatively charged PAA-coated γ-Fe_2O_3NPs could expand the hydrogel network and increase the number of pores and free spaces, lowering the mechanical strength. The PAA-coated γ-Fe_2O_3NPs can interact with some hydroxyl and amine groups of the hydrogel using Fe(III) and PAA moieties expanding the internal network structure.[226,227,228,229,230] The swelling abilities of hydrogel and magnetogel samples was measured and summarized in **Table 2.5**. All magnetogels showed higher swelling behavior in comparison to the native peptide-based hydrogel. This result may be attributed to the interaction of the hydrogel networks with PAA-coated γ-Fe_2O_3NPs, neutralizing the repulsions in the networks and resulting in the penetration of more water in order to compensate for the buildup of osmotic ion pressure.[8,231] Another water adsorbing moiety is the attached-PAA. These results are consistent with the rheological studies, and there is an inverse relationship between them, meaning that the higher mechanical strength causes the lower swelling ability of the gels. For all successive removal applications, we used the 10 mg/mL PAA-coated γ-Fe_2O_3NPs magnetogels because of their higher mechanical strength compared to the other two magnetogels.

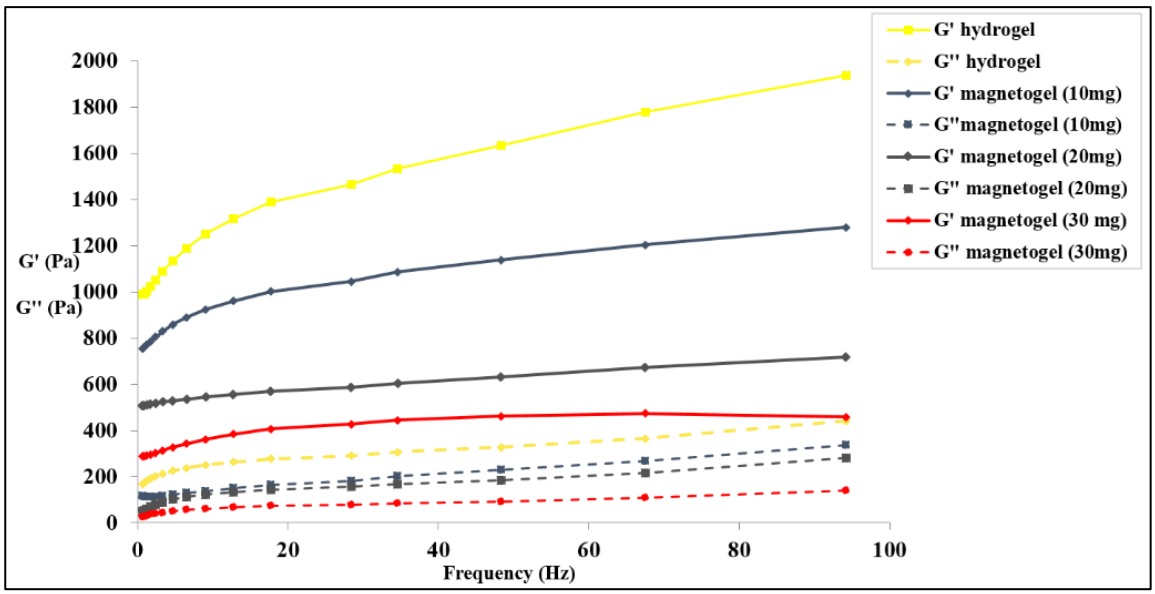

Figure 2.32. Frequency sweep of the hydrogel and Hgel@MNPs-PAA magnetogels.

Table 2.5. Swelling abilities of the hydrogel systems.

samples	Swelling degree (q)
hydrogel	62.1 ± 0.3
Hgel@MNPs-PAA (containing 10 mg/mL)	73.8 ± 0.9
Hgel@MNPs-PAA (containing 20 mg/mL)	81.2 ± 0.2
Hgel@MNPs-PAA (containing 30 mg/mL)	88.2 ± 0.3

Co(II) removal studies. $Co(II)_{(aq)}$ has a broad metal-based absorption peak in the visible region centered at 512 nm.[232] Over the whole removal process, the intensity of this peak decreases without significant change in the wavelength for all the three adsorbents (**Figures 2.33a** and **S8**) tested, *i.e.*,

HG, γ-Fe_2O_3NPs@HG, and γ-Fe_2O_3NPs@HG upon magnetic field application. In particular, in **Figure 2.33a**, the UV-Vis spectra of γ-Fe_2O_3NPs@HG upon magnetic field application is reported. The adsorption capacity of these systems was monitored as a function of contact time ($Co(II)_{initial}$ = 61 mg/mL), and q_t (in mg g^{-1}) plots are shown in **Figure 2.33b**, with contact times ranging from 0 to 480 min (**Equation 4, 5 Appendix A**). The adsorption capacities follow the trend γ-Fe_2O_3NPs@HG upon magnetic field application > γ-Fe_2O_3NPs@HG > HG, confirming the enhancing effect of γ-Fe_2O_3NPs on the adsorption. The interaction of magnetogel with an external magnet further increases the capacity, compared to that of the magnetogel. For each adsorbent, a fast Co(II) removal was observed in the first 15 min, which is due to the large number of active sites available on the hydrogel.[233] This rapid adsorption might be due to chemical rather than physical adsorption because of the possible complexation between the suitable functional groups of hydrogels and Co(II) ions. This phenomenon was already reported in several studies of Co(II) adsorption.[234,235] Then, their adsorption gradually slowed until reaching equilibrium after 480 min for all systems. At equilibrium, the capacity of γ-Fe_2O_3NPs@HG upon magnetic field application is about 1.25 times higher than that of the other two adsorbents. Total adsorption efficiencies were estimated, and the results show that γ-Fe_2O_3NPs@HG and γ-Fe_2O_3NPs@HG upon magnetic field application increase the removal efficiency by 0.3% and 5.3%, respectively (**Table 2.6**), in comparison with hydrogel alone. Under these experimental conditions, the external magnetic field has a relevant effect on the adsorption capacity and efficiency of the hydrogel.

As time passes, the removal speeds decrease, owing to more active sites occupied by Co(II) ions. To better understand the adsorption kinetics, two well-known kinetic models, pseudo-first order and pseudo-second order, were applied and evaluated using the given linearized equations (**Equations.** (**6**) and (**7**)), as provided in **Appendix A**. In general, the pseudo-first order model describes a reversible adsorption between solid and liquid phases,[236] claiming physisorption rather than chemisorption. Conversely, the second-order model mainly suggests a chemical adsorption of adsorbates onto the adsorbents;[237] in which chemical bonding occurs among the metal ions and polar functional groups of the adsorbents. Two kinetic plots are shown in **Figure 2.33(c,d)**, and the subsequently calculated kinetics parameters are summarized in **Table 2.7**. Considering the correlation coefficient, R^2 better-fitted straight lines were obtained from the pseudo-second order relation for all the adsorbents, compared to those obtained for the pseudo-first order plots. Moreover, the calculated equilibrium adsorption capacities, q_e, obtained from the pseudo-second order equation were much closer to the experimental trend seen in **Figure 2.33b**. The results suggest that the adsorption of Co(II) onto our synthesized HG and γ-Fe_2O_3NPs@HG systems

occurs through chemisorption, in agreement with previous works.[238] Also, we can clearly see the significant effect of magnetic interaction on the speed of adsorption, as shown in **Table 2.7**.

The chemisorption of Co(II) can be interpreted based on the coordination chemistry of Co(II) aquo complexes, which are kinetically labile species. For substitution reactions, the transition metal kinetics are governed by their electronic configurations. For octahedral complexes, the d orbitals split into high energy e_g (d_z^2 and $d_{x^2-y^2}$) and low energy T_{2g} (d_{xz}, d_{yz}, d_{xy}) levels, of which e_g orbitals show anti-bonding characters. Due to the high-spin d^7 configuration of Co(II) aqua complexes having the $T_{2g}^5 e_g^2$, they also exhibit the Jahn-Teller effect (z-out), which is a geometric distortion of a non-linear molecular system that reduces its symmetry and energy, seen in the complexes having the occupied e_g levels. Therefore, the Co(II) ions in the dissolution process have high lability and are vulnerable to the chemical substitution reaction to achieve their stable electronic configurations. In fact, the presence of Fmoc-Phe and diphenylalanine (Phe_2) in the hydrogel network can provide the chelating moiety (through their nitrogen and oxygen atoms) for the Co(II) ions, resulting in stable Co(II) complexes.[239]

Regarding the enhancing effect of γ-Fe_2O_3NPs nanoparticles, it is consistent with previous studies on magnetogels[240,241] and is related to the fact that NPs embedded in hydrogel can increase the cross-linking degree and porosity of the gel, providing a channel for the entry, exit, and adsorption of some substances. More importantly, the interaction of γ-Fe_2O_3NPs@HG with the external magnet further enhances the adsorption. As is well-known, magnetogels can exhibit an on/off effect on the hydrogel pores. In fact, swelling or shrinking states of γ-Fe_2O_3NPs@HG can be influenced by the magnetic dipole-dipole orientation of γ-Fe_2O_3NPs toward the external magnetic field[242] and can increase the permeability of Co(II) into the hydrogel network for the chemisorption.[243]

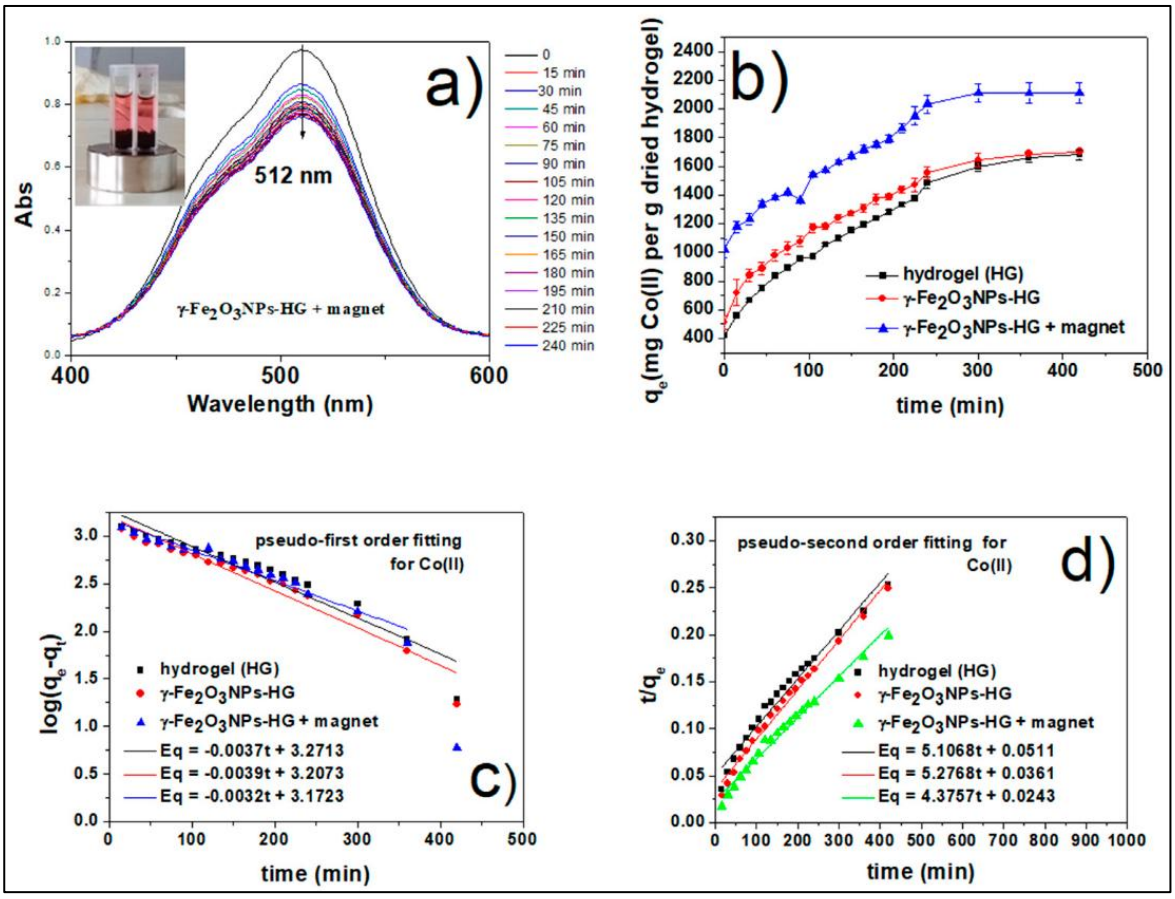

Figure 2.33. a) UV-Vis study of Co(II) adsorption by γ-Fe_2O_3NPs@HG upon magnetic field application (the UV-vis spectra for the peptide HG and γ-Fe_2O_3NPs@HG are reported in the Supporting Information section, toghether with the calibration curve for Co(II) aqueous solutions); b) adsorption capacity of HG, γ-Fe_2O_3NPs@HG and γ-Fe_2O_3NPs@HG upon magnetic field application *versus* time; c) fit of kinetic data to pseudo-first order model and d) pseudo-second order model for Co(II).[182]

Table 2.6. Co(II) adsorption efficiencies and capacities, obtained from the UV−Vis measurements at the equilibrium, at room temperature.

Adsorbent	**Removal% (RE%)**	**Experimental q_e (mg g^{-1})**
HG	20.4 ± 0.3	1680 ± 34
γ-Fe_2O_3NPs@HG	20.7 ± 0.4	1703 ± 42
γ-Fe_2O_3NPs@HG + magnet	25.7 ± 0.6	2111 ± 72

Table 2.7. Co(II) adsorption rate constant obtained from pseudo-first order and pseudo-second order models, at room temperature.

	pseudo-first-order model			**pseudo-first-order model**		
	k_1 (min^{-1})	q_e (mg g^{-1})	R^2	k_2 (g mg^{-1} min^{-1})	q_e (mg g^{-1})	R^2
hydrogel	0.0036	1867	0.9057	0.0005	1958	0.9722
Hgel@MNPs-PAA	0.0036	1611	0.9363	0.0005	1895	0.9872
Hgel@MNPs-PAA + magnet	0.0032	1486	0.9667	0.0004	2285	0.9834

Ni(II) removal studies. $Ni(II)_{(aq)}$ complexes display a typical octahedral structure with six water ligands in the first coordination shell[244] and an absorption maximum at 394 nm due to spin-allowed transitions. Upon interaction, a decrease in the absorption band was observed without significant changes in the wavelength (see supporting information, **Figure S9**). The γ-Fe_2O_3NPs@HG dramatically enhances the adsorption of Ni(II), with and without an external magnet. All the three systems show very fast adsorptions in the early 30 min, and applying an external magnet results in reaching the equilibrium earlier, after around 150 min for γ-Fe_2O_3NPs@HG + magnet. Considering the effect of an external magnet on γ-Fe_2O_3NPs@HG adsorption ability, a plateau is reached after 150 min. Without applying the external magnet, the equilibrium is reached later (after 360 min) but with 10% higher adsorption capacity (**Figure 2.34**). The adsorption efficiencies are summarized in **Table 2.8**, showing that the γ-Fe_2O_3NPs@HG and γ-Fe_2O_3NPs@HG + magnet systems can increase the removal efficiency by 7.3% and 5.1%, respectively, compared to the native hydrogel.

For all the three adsorbents, the speed of adsorption is higher in the beginning and slows down with time. Also, the adsorption speed of magnetogels (with and without an external magnet) is higher than that of the native hydrogel. Applying the kinetics models for the Ni(II) removal, it can be seen (**Figures 2.34b**) that the pseudo-second order model was more consistent for all these three systems (all second-order coefficients R^2 are higher than 0.97), supporting a chemisorption mechanism for Ni(II) (**Table 2.9**).

Table 2.8. Ni(II) adsorption efficiencies and capacities, obtained from the UV−Vis measurements at the equilibrium, at room temperature.

adsorbent	**% removal**
hydrogel	18.6 ± 0.1
Hgel@MNPs-PAA	25.9 ± 0.4
(Hgel@MNPs-PAA + magnet)	23.7 ± 0.4

Table 2.9. Ni(II) adsorption rate constant obtained from pseudo-first order and pseudo-second order models, at room temperature.

pseudo-first-order model				**pseudo-first-order model**		
	k_1 (min^{-1})	q_e ($mg\ g^{-1}$)	R^2	k_2 ($g\ mg^{-1}\ min^{-1}$)	q_e ($mg\ g^{-1}$)	R^2
hydrogel	0.0115	1948	0.8548	0.000005	1785	0.9735
Hgel@MNPs-PAA	0.0161	2998	0.8247	0.000007	2325	0.9954
Hgel@MNPs-PAA + magnet	0.0092	613	0.9457	0.000036	1851	0.9993

Cr(III) removal showed a different pattern, compared to Co(II) and Ni(II) adsorption. It is known that the aqueous $Cr(III)_{(aq)}$ can show three absorption peaks due to both the d→d electronic

transitions. In the present study, the absorption peak of 420 nm was monitored and assigned to spin-allowed transition. The UV-Vis spectra (reported in the supporting information, **Figure S10**) show the decrease in the 420 nm absorption band due to the removal of Cr(III). As can be seen in **Figure 2.34c**, the adsorption rate of both magnetogels γ-Fe_2O_3NPs@HG with and without the applied magnet is higher than that of the hydrogel HG in the first half of the experiments. However, at equilibrium, all adsorbents reach almost similar values of removal capacity (**Figure 2.34c**) (120–130 mg/g). Similar to the Co(II) and Ni(II) results, here also we clearly see the higher speed of magnetogels in removing the contaminant, further enhanced by the presence of a magnetic field. Table 8 reports the removal efficiencies for all the systems.

Kinetic studies provided us further detailed information on Cr(III) removal. The adsorption efficiency and fitting results of the kinetic models are given in **Tables 2.10** and **2.11**. For the hydrogel, the correlation coefficient (R^2) provided by the pseudo-first order model is much higher than that of the pseudo-second order, suggesting a physical mechanism for the adsorption of Cr(III) (**Figure 2.34d**). This can be explained by the electronic configuration of Cr(III) aqua complexes (d^3), which are kinetically inert and have a low rate for the chemical substitution reaction in normal conditions. The physical mechanism might be due to the electrostatic interaction of positively charged Cr(III) ions with the negatively charged hydrogel network. Conversely, the data obtained with both magnetogels (with and without magnet) fit with a pseudo-second order model, suggesting that the presence of γ-Fe_2O_3NPs@HG and magnetic field can both change the hydrogel network and porosity, providing chelating conditions inside the hydrogel suitable for the formation of the chemical bonds among hydrogel hyteroatoms and Cr(III) ions.

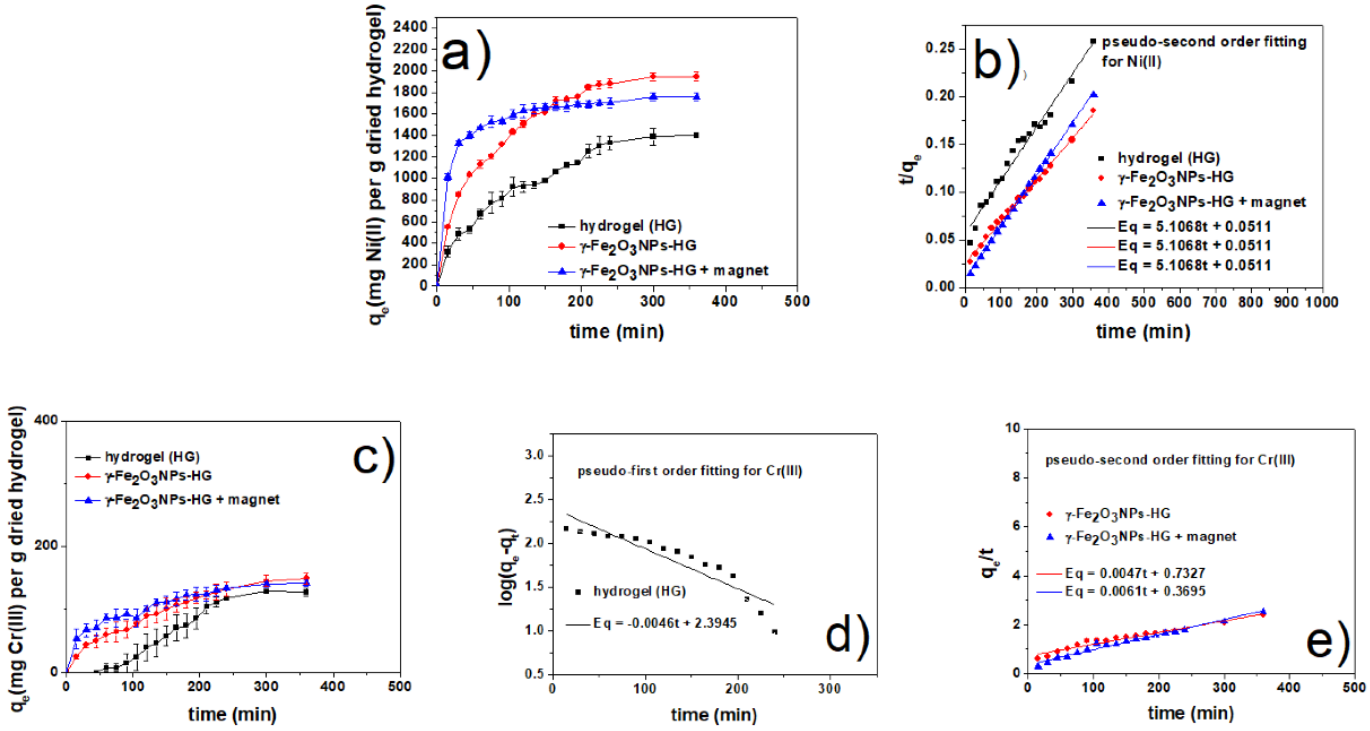

Figure 2.34. (**a**) Ni(II) adsobtion capacity of the HG, γ-Fe_2O_3NPs@HG and γ-Fe_2O_3NPs@HG + magnet *versus* time; (**b**) fit of kinetic data to the pseudo-second-order model for Ni(II). (**c**) Cr(III) adsobtion capacity of the HG, γ-Fe_2O_3NPs@HG and γ-Fe_2O_3NPs@HG +magnet *versus* time; (**d**) fit of kinetic data to the pseudo-first and (**e**) second-order models for Cr(III). (the complete UV-Vis study of Ni(II) and Cr(III) adsorption are reported in the supporting information section togheter with the Ni(II) and Cr(III) calibration curves).

Table 2.10. Cr(III) adsorption efficiencies and capacities, obtained from the UV−Vis measurements at the equilibrium, at room temperature.

adsorbent	**% removal**
hydrogel	13.2 ± 0.1
Hgel@MNPs-PAA	15.5 ± 0.1
Hgel@MNPs-PAA + magnet	14.7 ± 0.0

Table 2.11. Cr(III) adsorption rate constant obtained from pseudo-first order and pseudo-second order models, at room temperature.

pseudo-first-order model				**pseudo-first-order model**		
	k_1 (min^{-1})	q_e (mg g^{-1})	R^2	k_2 (g mg^{-1} min^{-1})	q_e (mg g^{-1})	R^2
hydrogel	0.0105	248	0.8355	-	27	0.0040
Hgel@MNPs-PAA	0.0101	184	0.9052	0.00003	212	0.9538
Hgel@MNPs-PAA + magnet	0.0112	134	0.9197	0.0001	163	0.9794

Two different experimental set-ups were developed for the removal of methylene blue (MB), rhodamine 6G (Rh6G), and methyl orange (MO) by using different hydrogel samples (**Figure 2.35**). In a first set of experiments, gel samples were prepared inside cuvettes, and then the aqueous

dye solution was placed on top of them. With this configuration, the dyes may diffuse into the gel matrix by gravity (without the need to apply any external forces). In another set of experiments, gel samples were prepared inside syringes. In the removal experiments, the dye solutions were allowed to flow inside the syringes, placed vertically, either by gravity or by applying an external force. Therefore, in this set-up, the dyes pass through the gel matrix and exit from the lower inlet of the syringe. **Figure S12** showes the calibration curves for these dyes.

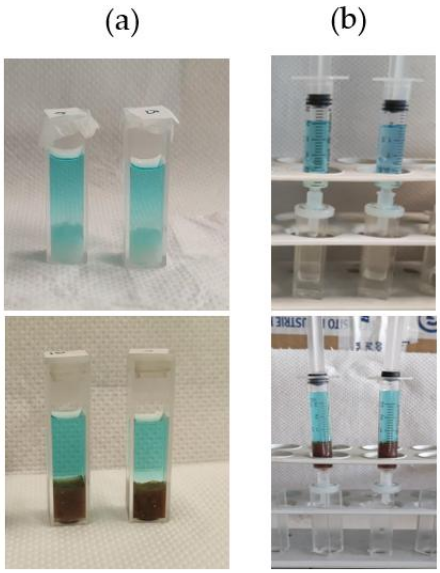

Figure 2.35. The two different set-ups used for the removal studies of organic dyes from water: a) employing cuvettes and b) employing syringes.

2.3.1. Experimental set-up employing cuvettes

MB has a heterocyclic aromatic structure (**Figure 2.36**) with characteristic absorbance peaks at 293 and 664 nm, related to $\pi - \pi^*$ and $n - \pi^*$ transitions, respectively.[245] The visible absorption (664 nm) was monitored during MB removal studies. Regarding Rh6G, it contains a xanthene moiety that is responsible for its $\pi \rightarrow \pi^*$ absorption at visible wavelengths.[246] The visible absorption at 527 nm was monitored for evaluating Rh6G removal by the adsorbents. The anionic dye MO has a strong absorption at around 500 nm, which was selected for the adsorption experiments.

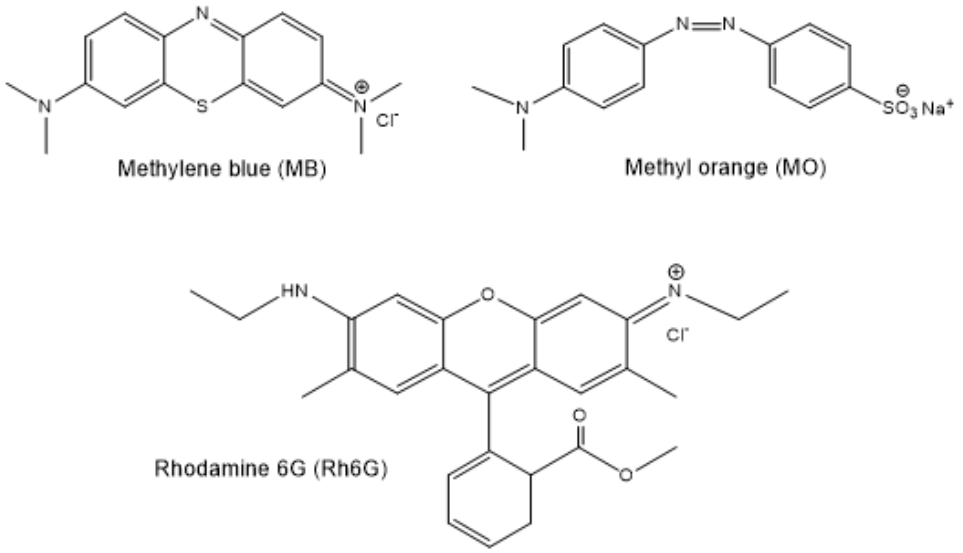

Figure 2.36. Chemical structures of methylene blue (MB), rhodamine 6G (Rh6G) (model cationic dyes) and methyl orange (MO) (model anionic dye).

Three different types of adsorbents were used for the removal of the three organic dyes described above from aqueous solutions: the native gel, γ-Fe_2O_3NPs@gel and γ-Fe_2O_3NPs@gel + mf (mf: external magnetic field).

In particular, the adsorption abilities of these materials were evaluated as a function of contact time with the solution of the selected dye and expressed as q_t (mg of dye absorbed by 1 g of dry hydrogel). The evolution of q_t values as a function of time for each dye+adsorbent system is reported in the plots in **Figures 2.37(a-c)**, for contact times ranging from 0 to 480 min. In addition, **Tables 2.11** and **2.12** show the removal efficiencies/capacities and calculated kinetic parameters of the three adsorbent systems for the three dyes, respectively.

The results obtained with this experimental set-up show that the magnetic NPs change the adsorption properties of the pristine gels and, also, an external magnetic field additionally modifies the adsorbing character of the gels. Over the whole removal process of the three examined systems, no significant changes were detected in the maximum wavelength of the dyes and, as can be seen in **Figures 2.37(a-c)**, dye adsorption decreased with time. This general feature, observed for all dyes and adsorbents, is probably linked to the progressive saturation of the active sites of the adsorbent over time, that eventually reaches the equilibrium after approximately 400 min.

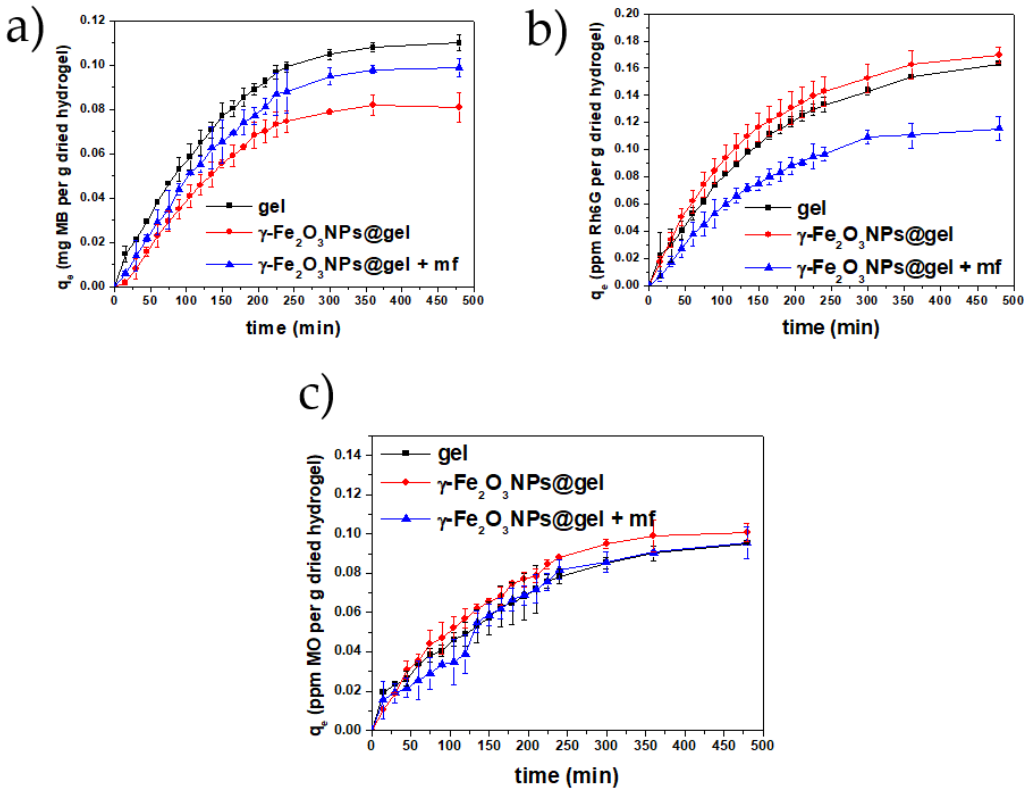

Figure 2.37. Adsorption capacities (q_t, mg/g) of the native gel, γ-Fe_2O_3NPs@gel and γ-Fe_2O_3NPs@gel + mf, versus time for MB (a), Rh6G (b) and MO (c).

Figure 2.37a shows that the q_t values for MB follow the trend gel > γ-Fe_2O_3NPs@gel + mf > γ-Fe_2O_3NPs@gel, which is different from those observed for Rh6G and MO, where γ-Fe_2O_3NPs@gel exhibits the best performance in terms of dye removal (**Figures 2.37(b,c)**). Such difference may be ascribed to the different structures of the dyes, which affect the gel-dye interaction at the molecular level.

Another worth mentioning result is the change of removal efficiencies (RE%) and final adsorption capacities for different systems, summarized in **Table 2.11**. For MB, the results show that the removal efficiencies of γ-Fe_2O_3NPs@gel and γ-Fe_2O_3NPs@gel + mf are decreased by 26.3% and 10.1%, respectively, in comparison with the native gel. For Rh6G, both magnetogels and pristine gels show similar RE% values and the combination of magnetogels with the application of a magnetic field significantly drops the adsorption efficiency by 29.1%. For MO, the magnetogel shows the highest RE% value, while the interaction of magnetogels with the magnetic field increases the dye removal by 16.7%.

Regarding the different effect of γ-Fe_2O_3NPs on dye adsorption, it is in good agreement with literature data on magnetogels[247,248] and is due to the ability of NPs embedded in hydrogels to affect both cross-linking degree and porosity of the gels, influencing the surface channels and, therefore, the entry, exit and adsorption of molecules.[249] Also, the application of an external magnetic field

can further change the adsorption, because magnetogels are able to exert an on/off effect on the hydrogel pores.[250] Swelling or shrinking states of γ-Fe_2O_3NPs@gels can be influenced by the magnetic dipole-dipole orientation of γ-Fe_2O_3NPs towards the external magnetic field[251] and most prorbably affect the permeability of dyes into the gel network.[252,253]

Table 2.11. Removal efficiencies and capacities (qe) of different hydrogel systems for MB, Rh6G and MO.

	adsorbent	removal efficiency% (RE%)	q_e (mg g^{-1})
MB	gel	30.8 ± 1	0.11 ± 0.0
	γ-Fe_2O_3NPs@gel	22.7 ± 2	0.08 ± 0.0
	γ-Fe_2O_3NPs@gel + mf	27.7 ± 1	0.09 ± 0.0
R6G	gel	45.7 ± 1	0.16 ± 0.0
	γ-Fe_2O_3NPs@gel	47.5 ± 1	0.17 ± 0.0
	γ-Fe_2O_3NPs@gel + mf	32.4 ± 2	0.11 ± 0.0
MO	gel	13.3 ± 1	0.09 ± 0.0
	γ-Fe_2O_3NPs@gel	14.1 ± 0	0.10 ± 0.0
	γ-Fe_2O_3NPs@gel + mf	13.4 ± 0	0.09 ± 0.0

As well known, the study of the adsorption kinetics is able to provide information on the nature of the adsorption (e.g. physisorption or chemisorption).[254] In this study, we employed pseudo-first and pseudo-second order kinetic models, as described for metal removal in **Appendix A**.The calculated kinetic parameters are summarized in **Table 2.12**, where the best correlation coefficients (R^2) of MB and Rh6G studies were mainly obtained when using the pseudo-first-order kinetic model, except for γ-Fe_2O_3NPs@gel (Rh6G) studies. For this system, the calculated equilibrium adsorption capacity, q_e, obtained from the pseudo-first order relation was more similar to the experimental values reported in **Figure 2.37** and **Table 2.11**, suggesting that the adsorption of Rh6G onto these adsorbents mainly occurs through physisorption. MB and Rh6G dyes possess cationic imine and amine groups that can favor their adsorprion on the hydrogels, thanks to different electrostatic interactions that may occur, such as that between the positively-charged imine nitrogen of the dyes and the negatively-charged hydroxyl groups of the hydrogel. Moreover, H-bonding interactions among the amine group of the dyes and the −OH groups of the hydrogels may be established.[255] Returning to the possible pseudo-second order mechanism estimated for γ-Fe_2O_3NPs@gel (Rh6G), it is attributed to chemisorption, which may depend on the chelation between the carboxyl and amine groups of the gels (–NH, –OH, and –COOH) and the lone pair electrons of the dye molecules.[256,257,258,259,260,261] Conversely to these cationic dyes, MO (as an anionic dye) shows much lower RE% and q_e values, which may be related to its negative charge, significantly limiting its electrostatic interaction with the gels, even if it was used at higher initial concentrations (10 ppm) than MB and Rh6G (5 ppm). For MO, two adsorbents show physisorption (gel and γ-Fe_2O_3NPs@gel + mf), controlled by physical forces like dipole-dipole interactions, hydrogen

bonds, van der Waals forces, hydrophobic interactions. Based on these results, the prepared adsorbent is more suitable for the removal of cationic dyes, rather than anionic ones.

Table 2.12. Kinetic data obtained from pseudo-first and pseudo-second order models for different hydrogel systems and MB, Rh6G or MO at RT.

		pseudo-first order			**pseudo-second order**		
	adsorbent	**k_1 (min^{-1})**	**q_e (mg g^{-1})**	**R^2**	**k_2 (g mg^{-1} min^{-1})**	**q_e (mg g^{-1})**	**R^2**
MB	gel	0.011	0.14	0.9715	0.037	0.16	0.9713
	γ-Fe_2O_3NPs@gel	0.012	0.12	0.9493	0.0028	0.35	0.1329
	γ-Fe_2O_3NPs@gel + mf	0.011	0.15	0.9323	0.017	0.18	0.8257
Rh6G	gel	0.0074	0.17	0.992	0.023	0.23	0.9822
	γ-Fe_2O_3NPs@gel	0.0080	0.18	0.9881	0.026	0.23	0.9921
	γ-Fe_2O_3NPs@gel + mf	0.0089	0.14	0.9696	0.018	0.20	0.8597
MO	gel	0.0069	0.10	0.9712	0.048	0.13	0.954
	γ-Fe_2O_3NPs@gel	0.010	0.13	0.9328	0.037	0.15	0.9832
	γ-Fe_2O_3NPs@gel + mf	0.0080	0.11	0.9638	0.024	0.15	0.8149

2.3.2. Experimental set-up employing syringes

The absorbing abilities of native gel, γ-Fe_2O_3NPs@gel and γ-Fe_2O_3NPs@gel + mf towards the selected dyes were tested with the experimental set-up employing syringes (**Figure 2.38**). Three different conditions were used, including: 1) gravitational passage of the dye through the gels inside the syringe (**Figure S13a**); 2) gravitational passage with application of filters attached to the outlet of the syringe (**Figure S13b**); and 3) application of a constant pressure to increase the flow rate of the dye inside the syringe, combined with the use of a filter at the outlet of the syringe (**Figure S13c**). In terms of time and reproducibility, the third set-up was selected as the optimized condition for studying the absorbing abilities of the gels. It must be taken into account that the filters absorb

part of the dye, therefore this filter absorption was quantified for each dye and then subtracted from the amount of dye removed by each hydrogel system (see **Figures S14-S17**).

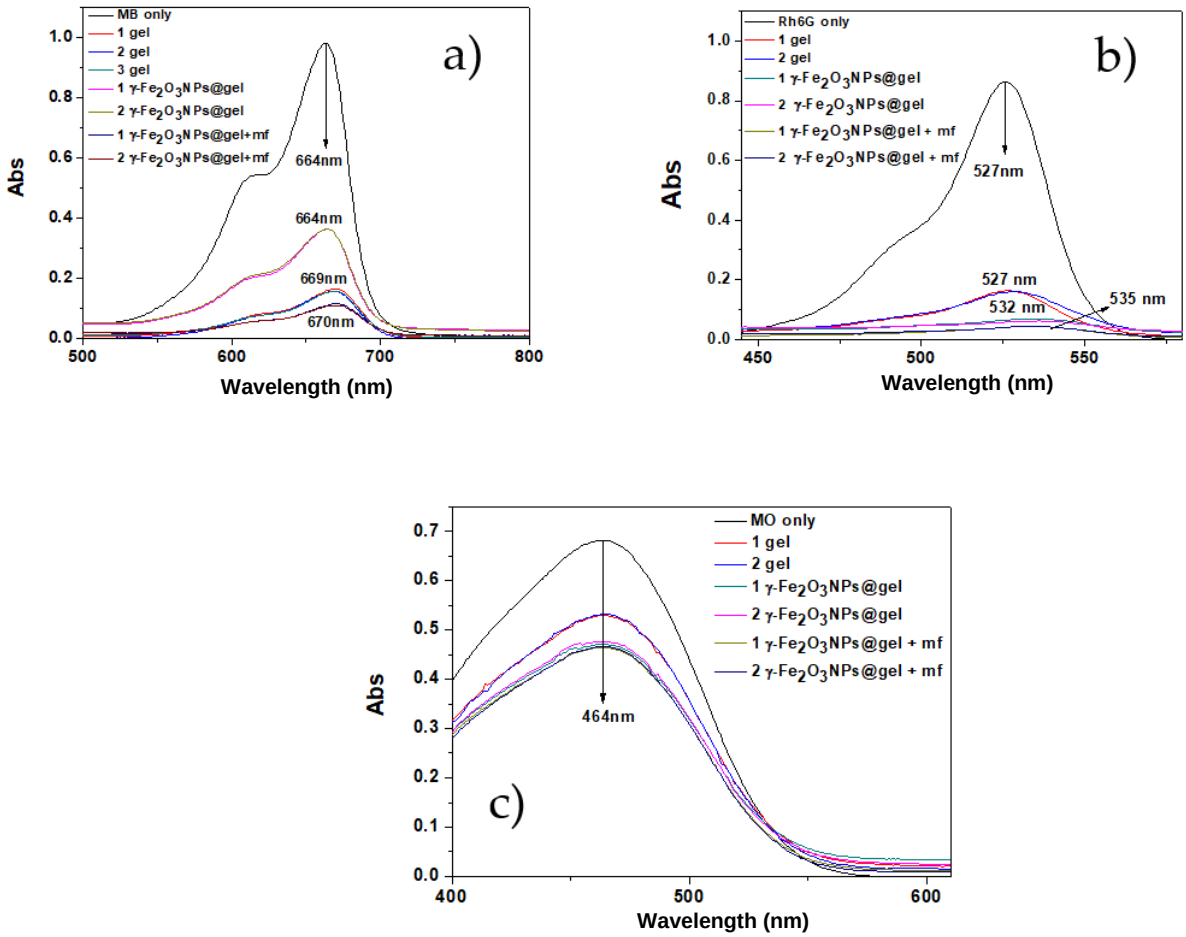

Figure 2.38. Absorbing abilities of gel, γ-Fe_2O_3NPs@gel, and (γ-Fe_2O_3NPs@gel + mf) for the removal of a) MB (C_0 = 5 ppm, pH = 7.4, 1 mg of adsorbent, flow rate = 0.2 mL/min); b) Rh6G (C_0 = 5 ppm, pH = 7.2, 1 mg of adsorbent, flow rate = 0.2 mL/min); c) MO (C_0 = 10 ppm, pH = 7.5, 1 mg of adsorbent, flow rate = 0.2 mL/min).

For the cationic dyes, MB and Rh6G, significant adsorptions (> 60%) were observed for all adsorbents (gel, γ-Fe_2O_3NPs@gel and γ-Fe_2O_3NPs@gel + mf) (**Table 2.13**). For MB, the pristine gel showed 20.3% higher RE% than the magnetogel, however, when the external magnet was used, the γ-Fe_2O_3NPs@gel + mf system demonstrated a 4.5% higher RE%, compared to the native hydrogel. For both γ-Fe_2O_3NPs@gel + mf and pristine gel systems, a red-shift was also detected, which may be attributed to the decrease of dye concentration, after passing through the gels. The UV-Vis spectrum of the initial MB solution shows a monomeric structure for the dye, that can exist in two monomeric mesomers (I and II), based on literature data (see **Figure 2.39**).[262]

Table 2.13. Adsorption efficiencies of different hydrogel systems for the removal of MB, Rh6G or MO from an aqueous phase using the experimental set-up employing syringes.

	adsorbent	RE% of cuvette set-up	RE% of syringe set-up
MB	gel	30.8 ± 1	80.4 ± 1
	γ-Fe_2O_3NPs@gel	22.7 ± 2	60.1 ± 2
	γ-Fe_2O_3NPs@gel + mf	27.7 ± 1	84.9 ± 0
R6G	gel	45.7 ± 1	83.2 ± 1
	γ-Fe_2O_3NPs@gel	47.5 ± 1	95.0 ± 0
	γ-Fe_2O_3NPs@gel + mf	32.4 ± 2	97.6 ± 0
MO	gel	13.3 ± 1	21.8 ± 7
	γ-Fe_2O_3NPs@gel	14.1 ± 0	30.0 ± 6
	γ-Fe_2O_3NPs@gel + mf	13.4 ± 0	31.3 ± 6

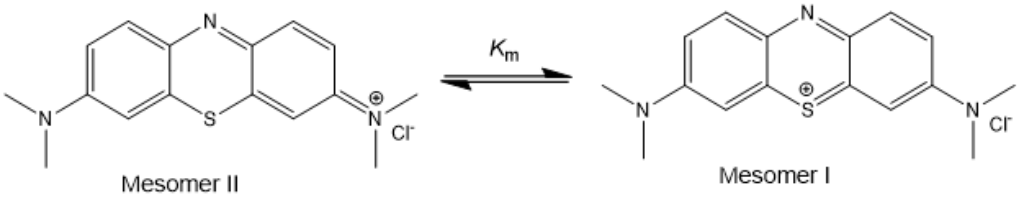

Figure 2.39. Alternative mesomeric structures for MB.

Based on Fernández-Pérez's work on the mesomeric structure of MB in water, we propose that, after the removal of the dye by the native gel or γ-Fe_2O_3NPs@gel+mf, the purified solutions contain the mesomeric II structure of MB, which has different UV-Vis adsorption with the observed red-shift, compared to the initial MB solution.

For Rh6G, more than 95% of the dye was removed by both γ-Fe_2O_3NPs@gel and γ-Fe_2O_3NPs@gel+mf and for the observed red-shift of the purified solutions, a monomer/dimer change of Rh6G may be proposed. In fact, the initial solution of Rh6G shows a combination of monomer/dimer species for the dye. After dilution, the concentration of monomers becomes significant and the spectral change is observed. Another important factor is the possible release of ions (e.g., Na^+, Cl^-) from the hydrogel matrix to the filtered solutions which can also affect the spectral pattern on the dyes.

Conversely to the cationic dyes, for MO no significant spectral changes were detected after filtration; RE% values for MO are much lower (20-30%) compared to MB and Rh6G, probably due to the different charges of the dyes. Regarding the amount of MO adsorbed by the three hydrogel systems, γ-Fe_2O_3NPs@gel and γ-Fe_2O_3NPs@gel+mf show the same adsorption efficiencies (approximately 30%), compared to lower amounts observed for the pristine gel (approximately 20%).

In **Table 2.14**, the adsorption capacities of γ-Fe_2O_3NPs@gel + mf (in the experimental set-up employing syringes) towards cationic dyes were compared with those of similar adsorbents reported

in literature. The observed lower adsorption capacities for the magnetogels described in this study may be improved by modifying the formulation of the magnetogel, e.g. using crosslinkers that could also improve the mechanical stability of the magnetogels and, therefore, their reusability as adsorbents.

By comparing the two experimental setups (cuvettes and syringes, see **Table 2.13**), the adsorption using cuvettes is much lower, as it occurs only at the interface between gel and solution, while in the case of syringes the solution passes through the mass of the gel, allowing a greater interaction with it and, consequently, a greater adsorption of the dyes. More importantly, in each methodology, the trends of RE% values of the adsorbents (**Figures S18-S20**) are changed. These to results demonstrate that syringes are more effective because of the ability of mechanical pressure applying which force the dyes move along the gels.

Table 2.14. Comparison of the adsorption capacities of (γ-Fe_2O_3NPs@gel + mf) with similar adsorbents for the removal of cationic dyes.

adsorbent	**cationic dyes**	**C_0 (mg mL^{-1})**	**adsorption capacities of syringe set-up (mg g^{-1})**	**reference**
γ-Fe_2O_3NPs@gel + mf	MB	0.005	0.9	this work
γ-Fe_2O_3NPs@gel + mf	Rh6G	0.005	1.1	this work
poly(acrylic acid-acrylamide-butyl methacrylate) magnetic hydrogel	MB	50-100	12.6	[263]
Fe_3O_4/poly(2-hydroxyethyl methacrylate-co-itaconic acid) magnetic hydrogels	MB	0.05-0.2	174.9	[264]
poly(2-(2-methoxyethoxy) ethyl methacrylate-*co*-oligo (ethylene glycol) methacrylate-*co*-acrylic acid) (PMOA) hydrogel-magnetic attapulgite/Fe_3O_4	RhB (rhodamine B)	0.001	1.65	[265]

3. Conclusion

The potential impact and perspective of this thesis could be summarized as:

1- We developed an in situ one-pot approach for preparing AgNPs inside peptide hydrogels using a photochemical synthesis, without any toxic reducing agents. We biosynthesized a very short self-assembling peptide containing only three amino acids with the maximum aromatic moieties that a tripeptide can have, which can self-assemble in water. *Pseudomonas* fluorescence lipase was used to catalyze the synthesis of the Fmoc-Phe3 hydrogelator. The use of biocompatible peptide molecules, instead of toxic precursors, paves the way for an eco-friendly generation of AgNPs. The novelty of this work lies in the development of different synthetic methodologies for one-pot preparation of hgel@AgNPs, where AgNP formation occurs in situ and simultaneously with the sol-gel transition. In addition, the synthesized nanocomposites showed significant anti-bacterial activity against *S.aureus*, a common bacteria frequently found on the skin and in the upper respiratory tract causing skin infection, sinusitis, and food poisoning without any vaccine prevention. The prepared hgel@AgNPs composites have the potential to be applied as films on the skin surface.

2- Moreover, we introduced a novel hydrogel composite using our short peptide hydrogels as scaffolds for stabilizing TiO_2NPs; which have the potential of photocatalytic inactivation of microorganisms. To our knowledge, this was the first report in which a self-assembling peptide hydrogel was used as scaffold for stabilizing TiO_2NPs. According to our previous studies, the antibacterial activity of Fmoc-Phe3 hydrogel is n, the antibacterial activity of Fmoc-Phe3 hydrogel is negligible, but adding TiO_2NPs significantly increased the photocatalytic antimicrobial properties of the composite against *S.aureus*. In addition, different concentrations of TiO_2NPs inside the hydrogels were used to investigate the effect of concentration on the swelling ability, mechanical strength, and antibacterial properties of the composites. However, the effect of ultrasonication during hydrogel preparation on the properties of the composites was evaluated.

3- Turning to the magnetogel, The goal of this work was to direct attention to emerging and novel research involving Magnetogel nanohybrid materials that might be relevant in future applications for the Treatment of wastewater, as well as other fields. Generally, composite hydrogels are promising adsorbents with tunable features, and we demonstrated that the addition of effective functional groups in nanohybrid materials through chemical conjugation is a promising strategy to further improve the adsorption abilities of hydrogels. The results achieved pointed out that the presence of γ-Fe_2O_3NPs provides magnetic properties to the resulting nanohybrids, which can be applied for magnetic-based removal applications of contaminants, such as heavy metal ions and dyes, from aqueous phases. The results of the removal studies demonstrate that the presence of

Fe_2O_3NPs in combination with the application of an external magnetic field increases the adsorption efficiency of the hydrogel matrix. In the future, this study could be expanded to test the recovering ability of the these adsorbing systems for the recycling of metal ions, and extensive efforts should be directed to scale up the applications and test the developed materials in practical scenarios. These results are promising for potential environmental applications of γ-Fe_2O_3NPs-peptide magnetogels to the removal of pollutants from aqueous media.

Acknowledgements

• Biological studies in collaboration with Dr. Enea Gino Di Domenico, Department of Biology and Biotechnology "C. Darwin", Sapienza University of Rome

• FESEM in collaboration with Francesco Mura at Sapienza Nanotechnology and Nanoscience Laboratory (SNN-Lab CNIS)

• ICP-OES measurements in collaboration with Prof. Silvano Mignardi, Department of Earth Science, Sapienza University

• XPS and Raman measurement of removal studies in collaboration with Prof. Andrea Giacomo Marrani and Dr. Francesco Amato

• Rheological measurments in collaboration with Dr. Fabrizio Marra at Sapienza Nanotechnology and Nanoscience Laboratory (SNN-Lab CNIS)

• Preparation of the magnetic nanoparticles in collaboration with Prof. Ilaria Fratoddi, and Dr. Farid Hajareh Haghighi

I sincerely acknowledge for useful helps and discussions with Dr. Laura Chronopoulou, and all the other colleagues and students of the laboratory.
Plots, schemes, and figures were drawn with BioRender, ChemDraw Professional, OriginLab.

This work was partially supported by Sapienza grant "Avvio alla Ricerca 2022" AR122181687C379A.

4. Appendix A

4.1. Materials:

Silver nitrate ($AgNO_3$, 98%, Sigma-Aldrich, 169,87 g/mol); Sodium3-mercapto-1-propanesulfonate (3MPS, 98%, Sigma-Aldrich, 178,21 g/mol); Sodium borohydride ($NaBH_4$, 99%, Sigma-Aldrich, 37,83 g/mol); Sodium dodecylsulfate (SDS); β-D-Glucose (Commercial product, 180,156 g/mol); Honey (Millefiori) (G.B. Ambrosoli SpA, Commercial product); Fluorenylmethyloxycarbonyl-phenylalanine (Fmoc-Phe-OH, 99%, Bachem, 387,44 g/mol); L-Diphenylalanine (H-Phe-Phe-OH, 98%, Bachem, 312,36 g/mol); Lipase from *Pseudomonas fluorescens* (Sigma-Aldrich, ≥20,000 U/g); Deionized water; NaOH (Carlo Erba Reagents, ≥98%); HCl (Carlo Erba Reagents, 37%); NaCl (Carlo Erba Reagents); KCl (Carlo Erba Reagents); Acetone; Ethanol; $FeCl_2 \cdot 4H_2O$ (Fluka, 198.75 g/mol); $FeCl_3$ (Fluka, 162.20 g/mol); $CrCl_3 \cdot 6H_2O$ (Carlo Erba, 158.36 g/mol); $NiCl_2 \cdot 6H_2O$ (Alfa Aesar, 129.59 g/mol); $CoCl_2 \cdot 6H_2O$ (Alfa Aesar, 129.83 g/mol); Dyes

4.2. Instrumentation:

All UV-Vis spectra were recorded in 1.00 cm optical path quartz cells using a UV/Visibile Ultraspec 4000 spectrophotometer (Pharmacia Biotech, Uppsala, Sweden).. The measurements were performed as the wavelength of resonance related to silver nanomaterials is between approximately 400 and 500 nm, depending on their dimensions, as mentioned above. Several analyzes have been conducted to study how surface plasmon resonance varies of silver nanoparticles as a function of various parameters, such as time, temperature conservation of the samples, and, as regards the AgNPs synthesized with $NaBH_4$, β-D glucose, and honey, the time of exposure to sunlight. For these measurements, the AgNPs in solution were diluted and sonicated to break any aggregates that had been formed. Instead, to analyze the AgNPs trapped in the hydrogel matrix, the composites were first mechanically broken, then diluted and sonicated too.

The measurement of the size of the NPs was conducted using the Dynamic Light technique Scattering (DLS), using a Zetasizer Nano ZS instrument (Malvern Instruments, UK). This technique is based on the fact that when a suspension is crossed by a ray bright, a part of the light that hits the particles is scattered, that is, it is deflected from the its straight path in all directions. It is observed that the intensity of the scattered light measured at a given angle θ varies with time. These intensity fluctuations are due to motion Brownian, i.e. the random motion of suspended particles in all directions. Even more so, the particles move quickly, the more rapid the variations in intensity are. The experimental conditions used are the following: a He-Ne laser operating at $\lambda = 633$ nm, with a fixed dispersion angle of 173° and at a constant temperature (25 °C). For these measurements, the AgNPs in solution were diluted and sonicated to break any aggregates that had been formed. Instead, to analyze the AgNPs trapped in the hydrogel matrix, the composites were first mechanically broken, then diluted and sonicated too.

Morphological characterization of the all NPs (Ag, TiO_2, γ-Fe_2O_3) and composite hydrogels were performed through field emission scanning electron microscope (FESEM) measurement. FESEM images were obtained using a variable pressure scanning electron microscope (VP-SEM, Hitachi SU-3500) equipped with dual-energy-dispersive X-ray spectroscopy detectors (VP-SEM-dEDS) in a parallel configuration (Bruker, XFlash 6|60) and a high active area (60 mm^2 each). Samples were deposited onto stubs without the need for a conductive coating and analyzed at an accelerating voltage that avoided radiation damage.

ICP-AES was performed to find the yield of the in situ formed AgNPs after exposure. First, the nanoparticles were separated from unreacted silver ions using 3 kDa membrane f ilter (Amicon Ultra-100 Centrifugal Filter Unit, Millipore, UK) inside a centrifuge with 15,000 rpm for 30 min at 20 C. Then the purified nanoparticles were digested in HNO_3 overnight, and the final solution was diluted by a final factor of 25 before the measurements. The amount of formed AgNPs in ppm was analyzed by inductively coupled plasmaatomic emission spectrometry (ICP-AES) with a Varian Vista RL CCD Simultaneous ICP-AES spectrometer. The analytical detection limit for Ag was 0.04 mg/L, and analytical errors were estimated to be in the order of 3% using Ag emission line 338.289 nm. The formation yield for AgNPs was calculated with the following equation:

$$Yeild = \frac{experimental\ Ag\ quantity}{theoretical\ Ag\ quantity} \times 100$$

Raman spectra were run at room temperature in backscattering geometry with an inVia Renishaw micro-Raman spectrometer equipped with an air-cooled CCD detector and super-Notch filters. An Ar^+ ion laser (λ_{laser} = 514 nm) was used, coupled to a Leica DLML microscope with a 20× objective. The resolution was 2 cm^{-1} , and spectra were calibrated using the 520.5 cm^{-1} line of a silicon wafer[266].

FTIR-ATR data were collected with a Bruker Vertex 70 instrument (Bruker Optics, Ettlingen, Germany) using KRS-5 cells in the 4000−400 cm^{-1} range or in ATR mode on a diamond crystal in the 4000−600 cm^{-1} spectral region.

To characterize the composites from a rheological point of view, it is possible to exploit dynamo-mechanical analysis (mechanical spectroscopy). In this case, the test in oscillatory mode was carried out on the hydrogels with an Anton Paar MCR 302 rotational rheometer, registering the elastic (G') and viscous (G") moduli trend, in the presence and absence of silver nanoparticles, varying the frequency of application of the stimulus and keeping the intensity of the deformation to which the samples are subjected constant (shear strain = 1%). These frequency sweep experiments are carried out with a rotational rheometer having a plate-plate geometry, keeping the gap between the two plates constant (1 mm). The test is performed under constant temperature conditions (30 °C).

For XPS analysis, a modified Omicron NanoTechnology MXPS system was employed. Samples were excited by achromatic AlKα photons (hν = 1486.6 eV), operating the anode at 14–15 kV, 10–20 mA. The take-off angle and pass energy were fixed at 21◦ and 20 eV, respectively. Samples were prepared by casting onto a hydrogenated Si(100) wafer a 20 µL drop of a hydrogel where the initial Ag+ concentration was 15 mM. The obtained Si-supported sample was left to dry overnight, and then mounted on a stainless steel sample holder for measurement.

For characterization of the hydrogel composites containing AgNPs, The small angle X-ray scattering measurements were conducted at SAXS Lab Sapienza with a Xeuss 2.0 Q Xoom system (Xenocs SA, Grenoble, France) equipped with a micro-focus Genix 3D X-ray Cu source and a two-dimensional Pilatus3 R 300 K detector (Dectris Ltd., Baden, Switzerland) as reported previously[267].

In the case of TiO_2 NPs, SAXS measurements were carried out based on previously published works with some modifications[8]. A Xeuss 2.0 Q Xoom instrument (Xenocs SA, Grenoble, France) was used. A small portion of each hydrogel sample was inserted into borosilicate glass capillaries and the measurements were carried out at 25 ± 1 °C and reduced pressure (< 0.4 mbar). Model intensities were calculated using SasView[268]. In order to obtain information on the size in the real space of the inhomogeneities giving rise to SAXS profiles, pair distance distribution functions were obtained by indirect Fourier inversion of the I(q) using the GNOM software of the ATSAS package[269].

Swelling ability of the hydrogels were investigated after hydrogel formation. In this cases 3 mL of phosphate buffer solution (PBS, pH = 7.4) was added and incubated for 24 h at 30 °C in a thermostatic bath. Then PBS was removed, and the hydrogels were lyophilized. The swelling degree was calculated according to the Equation (1):

$$q = \frac{Ws - Wd}{Wd} \quad (1)$$

q =swelling degree, Ws = hydrogel weight after PBS removal, Wd = weight of lyophilized gel.

The degradation kinetics of the native hydrogels as well as hydrogel composites containing AgNPs, under physiological conditions, were evaluated using the following stability assay. Briefly, 8.5 mL of Ringer's solution, containing NaCl (8.6 mg/mL), KCl (0.3 mg/mL), and $CaCl_2$ (0.33 mg/mL), were added to each hydrogel sample. Samples were incubated at 37 °C for 30 days. After incubation, the supernatant was removed. The hydrogels were weighed before adding Ringer's solution (W0) and after its removal (Wt). The percentage of weight loss (ΔW%) was calculated using Equation (2)

$$\Delta w\% = \frac{W0 - Wt}{Wt} \times 100 \quad (2)$$

To obtain the daily degradation rate (T), the percentage of weight loss (ΔW%) was then divided by the total incubation time (30 days) using Equation (3):

$$T = \frac{(\Delta W\%)}{30} \quad (3)$$

4.3. Methods

Synthesis of Fmoc-tripeptide composite hydrogels and PAA-coated magnetic nanoparticles. For the preparation of the hydrogel, 40 μmol of Fmoc-Phe and 40 μmol of Phe_2, were dispersed in 1 ml of water in a glass vial and stirred magnetically. To dissolve the peptides the pH value was increased to 12 adding 0.42 mL of 0,5 M NaOH and stirring for approximately 10 minutes. Then pH was adjusted to 7 by the addition of 1,5 ml of 0.1 M HCl, reaching a final volume of 3 ml. *Pseudomonas fluorescence* Lipase solution (50 mg/ml) was added (100 μL) and the reaction mixture was placed in a thermostated bath at 37°C for 30 minutes.

In the case of AgNPs/hgel (AgNPs/hgel) composite preparation, equimolar quantities of the amino acid and dipeptide along with 0.750 mL of H_2O and 0.315 mL of NaOH were mixed and stirred for 10 min. Then, 0.333 mL of $AgNO_3$ was added to the mixture and the pH was decreased to around 7 using HCl. Then the volume was adjusted to 3 mL and PFL was added. For the preparation of the composite with honey (AgNPs/hgel-honey), Before the addition of PFL solution, 0.90 mL of honey (350 mg/mL) was introduced and the mixture was incubated for 30 min at 37 °C in a thermostated bath. Regarding the synthesis using β-D-glucose, the AgNP precursors solution was prepared by hydrogel precursors and dissolved in an aqueous phase with the following reagents: 0.333 mL of $AgNO_3$ (5 mM), 0.333 mL of SDS (10 mM) and 0.333 mL of β-D-glucose (75 mM). The optimized molar ratios among the reagents are equal to 1: 2: 15 ($AgNO_3$: SDS: β-D-glucose). The mixture was then stirred magnetically for 1 min to start the nucleation of AgNPs. When using $NaBH_4$, the AgNPs precursors solution was prepared as follows: 0.333 mL of $AgNO_3$ (5 mM) and 0.333 mL of 3MPS (20 mM) were mixed and bubbled with Ar for 10 min. At the end of bubbling, 0.333 mL of $NaBH_4$ (25 mM) were added to start the AgNPs nucleation and then they added to the hydrogelators.

To prepare the hydrogel composites containing TiO_2 NPs (hgel-TiO_2NPs), a titania water dispersion was added instead of water, after 30 minutes in an ultrasonic bath. Two different titania concentrations were used: 5 mg/3ml, 10 mg/3 mL.

In the case of Hgel@MNPs-PAA composite, first The PAA-coated magnetic nanoparticles were synthesized in a separate step using the co-precipitation method in which 40 mg of $FeCl_3$ and 25 mg of $FeCl_2 \cdot 4H_2O$ were dissolved in 25 mL of an aqueous solution of polyacrylic acid (PAA) and degassed with $Ar_{(g)}$ for 15 min, followed by increasing the temperature to 80 °C. Then pH of this solution was increased to 11 by a fast addition of NaOH (10 M). The mixture was stirred at 80 °C for 60 min (with constant monitoring of the pH) and then cooled down to room temperature. The dark-brown colloidal solution of MNPs was collected by the strong magnet (1.42-1.47 T) and

washed three times with a total volume of 150 mL of ultra-pure water, to remove the excess amount of NaOH and other non-magnetic species. The resultant nanoparticles were freeze-dried and stored at room temperature. Regarding the PAA, it was synthesized by radical polymerization of acrylic acid (2 mL) in the presence of initiator potassium persulfate (50 mg) in a total volume of 25 mL water for at 80 °C for 5 h. For the preparation of peptide hydrogels impregnated with the synthesized magnetic NPs 1 mL of three different concentrations of MNPs suspension (10mg/mL, 20mg/mL, and 30mg/mL) were selected and added to the hydrogelatros instead of water with the same procedure as described for composites containing titania NPs.

Adsorption Experiments. Magnetogel samples were prepared in cuvettes, and 2 mL of the target solutions (Co(II), Ni(II), and Cr(III)) were cast on top of them, using different concentrations of the cations (see Figure S7). We only used the 10 mg type γ-Fe_2O_3NPs/hgel magnetogel because of its higher mechanical strength, evidenced by the rheological characterization. The removal studies were performed using UV-Vis spectroscopy, and the results are presented in Figures 2.34 and S9–S11. For all the tested pollutants, we used three main hydrogel-based absorbents including (1) HG, (2) γ-Fe_2O_3NPs/hgel magnetogel, and (3) γ-Fe_2O_3NPs/hgel + magnet). We also studied the removal efficiency of γ-Fe_2O_3NPs alone (10 mg/mL), and no significant change was observed in the UV-Vis of solutions. For dyes removal, 2 mL of aqueous dye solution (MB, Rh6G or MO) were cast on top of the gels. The concentration of MB and Rh6G was 5 ppm, while MO concentration was 10 ppm.

The UV-Vis absorbances of the solutions were monitored over time with 15 min intervals, and the removal efficiency (RE) was estimated by absorption spectra using Equation (4) as follows:

$$RE(\%) = \frac{C0-Cf}{C0} \times 100 \quad (4)$$

where C_0 is the initial concentration of pollutant and C_f is the concentration of pollutant in the eluted solution. The calibration curves were obtained and used for the calculations. Also, the adsorption capacities were estimated using the stock solutions of the pollutants (Co(II), Ni(II), and Cr(III)) prepared at pH 7, and their concentrations remaining in solutions after specific time intervals were determined by UV-Vis spectrophotometry. The adsorption capacity (qe, mg g^{-1}) of the adsorbents was calculated using Equation (5)[270]:

$$qe = \frac{C0-Ce}{m \times V} \quad (5)$$

where m (g) is the dried hydrogel mass, C0 and Ce (mg L^{-1}) are the initial and equilibrium pollutant concentrations, and V (L) is the solution volume, respectively. Kinetic behavior was studied using non-linear pseudo-first order and pseudo-second order kinetic models (Equations (6) and (7))[271].

$$\log(qe - qt) = \log qe - \frac{k1t}{2.303} \quad (6)$$

$$\frac{t}{qt} = \frac{1}{k2qe2} + t/q \quad (7)$$

Tested microorganisms for antibacterial activities. For the case of hydrogel, composites containing AgNPs alone and AgNPs coated with honey, S. aureus ATCC 25923 was purchased from the American Type Culture Collection. The methicillin-resistant Staphylococcus aureus (MRSA) clinical isolate was provided by the Microbial Strain Repository of the Microbiology and Virology laboratory of San Gallicano Dermatology Institute, Rome, Italy, collected in 2020 from a patient presenting skin and soft tissue infections[272].

For the case of composites containing AgNPs synthesized with $NaBH_4$ and β-D-glucose as reducing agents, The antimicrobial activity was evaluated using the S. aureus strain from the American Type Culture Collection (ATCC) 25923. The laboratory strain S. aureus ATCC 25923 was collected from a Blood Agar plate (Oxoid, Basingstoke, Hampshire, UK).

For the case of composites containing TiO_2NPs, S. aureus ATCC 6538 was purchased from the American Type Culture Collection. (Manassas, VA, USA) Methicillin-resistant Staphylococcus aureus (MRSA) clinical isolates were provided by the Microbial Strain Repository of the Microbiology and Virology Laboratory of San Gallicano Dermatological Institute IRCCS, Rome, Italy. These microorganisms were collected in 2020 from patients presenting skin and soft tissue infections. MRSA strains presented the gene for methicillin resistance (mecA), oxacillin resistance (MIC ≥ 4 mg/mL) and a positive agglutination test for penicillin-binding protein (PBP2; Oxoid, Basingstoke, UK). Whole-genome analysis of MRSA strains and the phylogenomics were carried out as previously described[273].

Plate inhibition zone assay to test for antimicrobial activity. An overnight culture of S. aureus ATCC 25923 or MRSA grown on a blood agar plate was used to inoculate 2 mL of 0.45% saline solution to 0.5 ± 0.1 McFarland turbidity standard (~108 CFU/mL). Then, the bacteria were swabbed onto a Chocolate agar plate (bioMérieux, Marcy-l'Étoile, France). A 20 µL drop containing AgNPs formulations was released on the top of the agar plate and incubated at 37 ◦C for 24 h. A 0.45% saline solution was used as the positive control. After 24 h of incubation, the diameter of the inhibition zone was measured, and plates were photographed.

Determination of minimal inhibitory concentration (MIC). For the case of hydrogel, composites containing AgNPs alone and AgNPs coated with honey, The experiments were conducted as previously described[274]. Antimicrobial susceptibility testing (AST) of silver nanoparticles in the hybrid in the free form was performed as described previously[275]. The metabolic activity of the treated planktonic bacterial cultures was evaluated in the presence of serial two-fold dilutions of different compounds[264]. Experiments were conducted in triplicate and repeated three times.

For the case of composites containing AgNPs synthesized with $NaBH_4$ and *β*-D-glucose as reducing agents, MICs (minimum inhibitory concentrations) were calculated using the broth microdilution method. The laboratory strain S. aureus ATCC 25923 inoculated in 2 mL of 0.45% saline solution (Air Life, Fresno, CA, USA) to obtain turbidity of 0.5 ± 0.1 McFarland (McF). Subsequently, 100 µL of bacterial suspension, diluted 1:100 in cation-adjusted Mueller–Hinton broth (MHB), corresponding to 1 × 106 CFU/mL, was used to inoculate a 96-well polystyrene plate (Corning Inc., Corning, NY, USA). bacteria were incubated at 37 ◦C for 24 h in the presence of different concentrations of antimicrobial compounds. After treatment with the different antimicrobial compounds, viable cells were determined with plate counting for the CFU/mL determination[264]. All experiments were in triplicate and repeated three times.

For the case of composites containing TiO_2NPs, The antimicrobial activity of hgel-TiO2NPs and TiO_2NPs was determined for each strain using the broth microdilution method to define the minimum inhibitory concentration (MIC). Briefly, a standard bacterial inoculum of approximately 1 × 105 CFU/mL was prepared in cation-adjusted Mueller–Hinton broth (MHB, Thermo Fisher Scientific, Waltham, MA, USA) and used to inoculate a 96-well polystyrene flat-bottom plate with 100 µL. Cells were treated with serial 2-fold dilutions of the compounds in MHB, ranging from 1.6 to 0.05 mg/mL. Growth controls containing no compounds and sterility controls without bacteria were also included. To evaluate the bactericidal activity of UV light-activated hgel-TiO_2NPs and TiO_2NPs, a preliminary set of experiments was conducted using microplates exposed to direct UV light for 10, 5 and 3 min[276]. The plates were incubated for 24 h at 37 ◦C in a microplate reader (Multiskan SkyHigh, Thermo Fisher Scientific, Waltham, MA, USA), where QD600 readings were taken every 20 min. Viable cell counts were determined through plate counting to measure CFU/mL. Experiments were performed in triplicate and repeated three times.

Determination of Metabolic Activity. To determine the metabolic activity, 100 µL of a standard bacterial inoculum of approximately 1 × 105 CFU/mL bacteria, treated with a two-fold dilution of the tested compounds as previously described (from 16 to 0.05 mg/mL), was placed in 96-well flat-bottom microtiter plates with the addition of resazurin (Promega, Madison, WI, USA). Positive controls of the bacterial inoculum were left untreated. Metabolic activity was assessed in the absence of UV exposure. The plates were incubated for 1200 min (20 h) at 37 ◦C and the absorbance (600 nm) was recorded every 20 min by a multidetector microplate reader (Multiskan SkyHigh, Thermo Fisher Scientific, Waltham, MA, USA)[264].

Appendix B: (supporting figures)

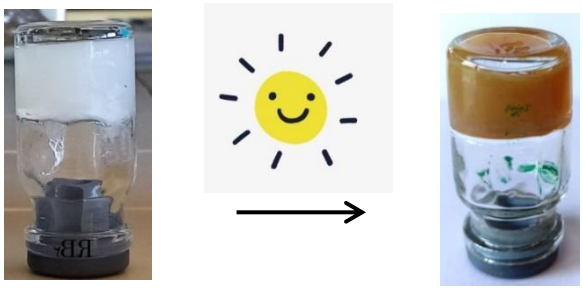

Figure S1. Color changing of the prepared hydrogel containing silver solution after exposuring to the sun light (formation of the AgNPs).

Figure S2. Color changing of the prepared hydrogel containing silver solution and honey after exposure to the sunlight (formation of the AgNPs@honey).

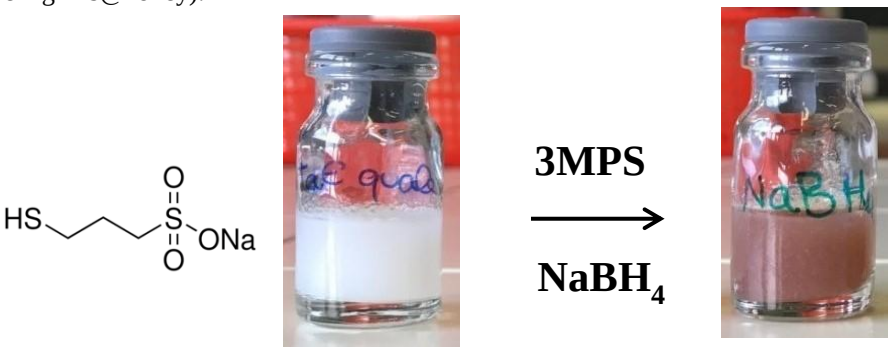

Figure S3. Preparation of the peptide hydrogel composites impregnated with AgNPs in the presence of 3MPS as capping agent and $NaBH_4$ as reducing agent (conventional method).

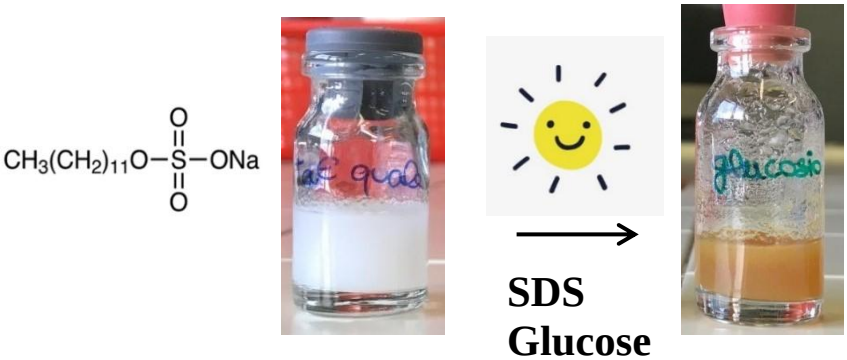

Figure S4. Preparation of the peptide hydrogel composites impregnated with AgNPs in the presence of SDS as capping agent and glucose as a green reducing agent (green method).

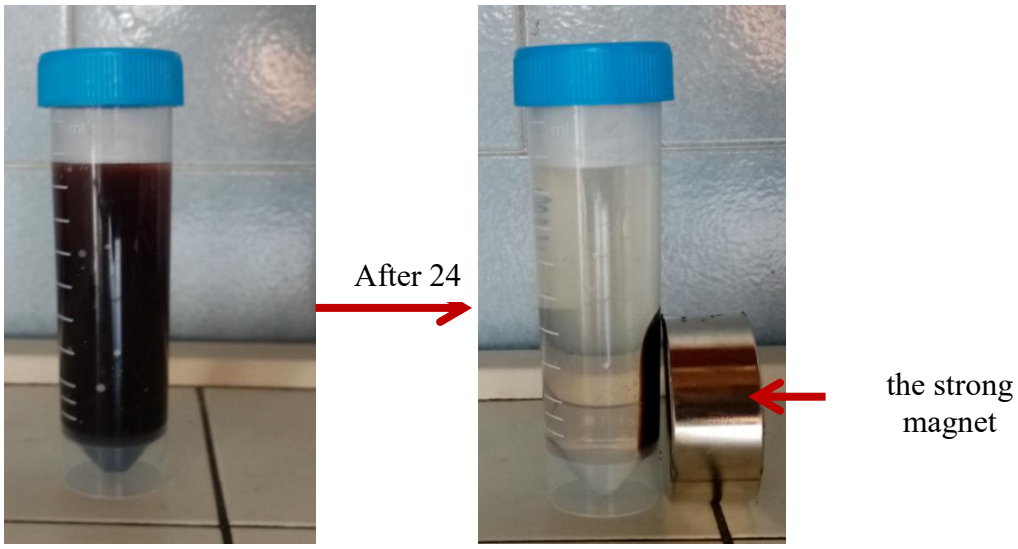

Figure S5. Separation of γ-Fe_2O_3NPs with an external magnetic field (1.42-1.47 T).

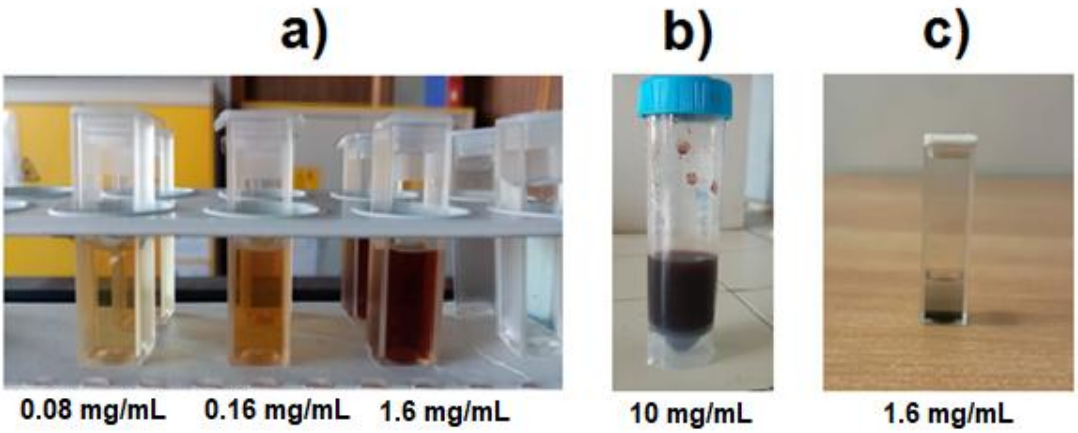

Figure S6. PAA-coated γ-Fe_2O_3NPs solutions after one week for a) 1.6, 0.16 and 0.08 mg/mL and b) 10 mg/mL; c) sedimentation of uncoated γ-Fe_2O_3NPs after 24 h.

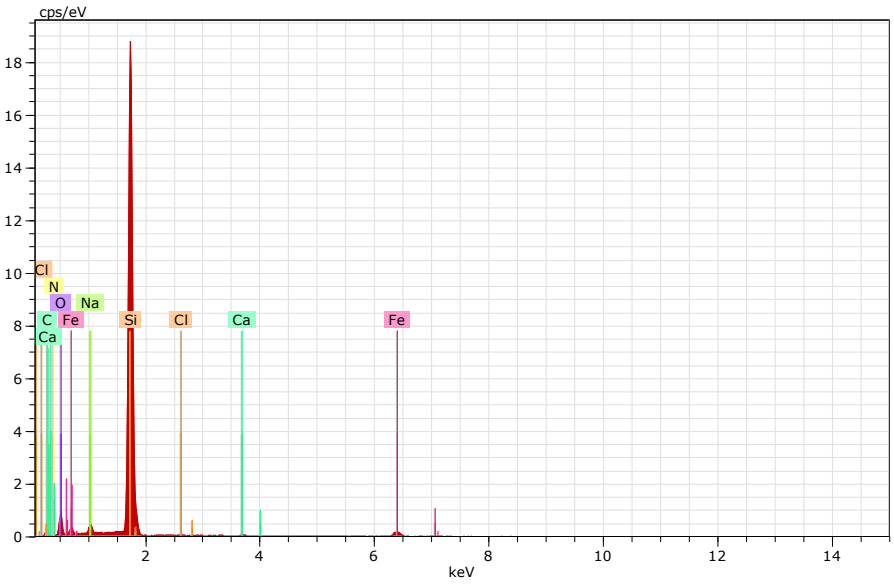

Figure S7. EDS spectrum of PAA-coated γ-Fe_2O_3NPs.

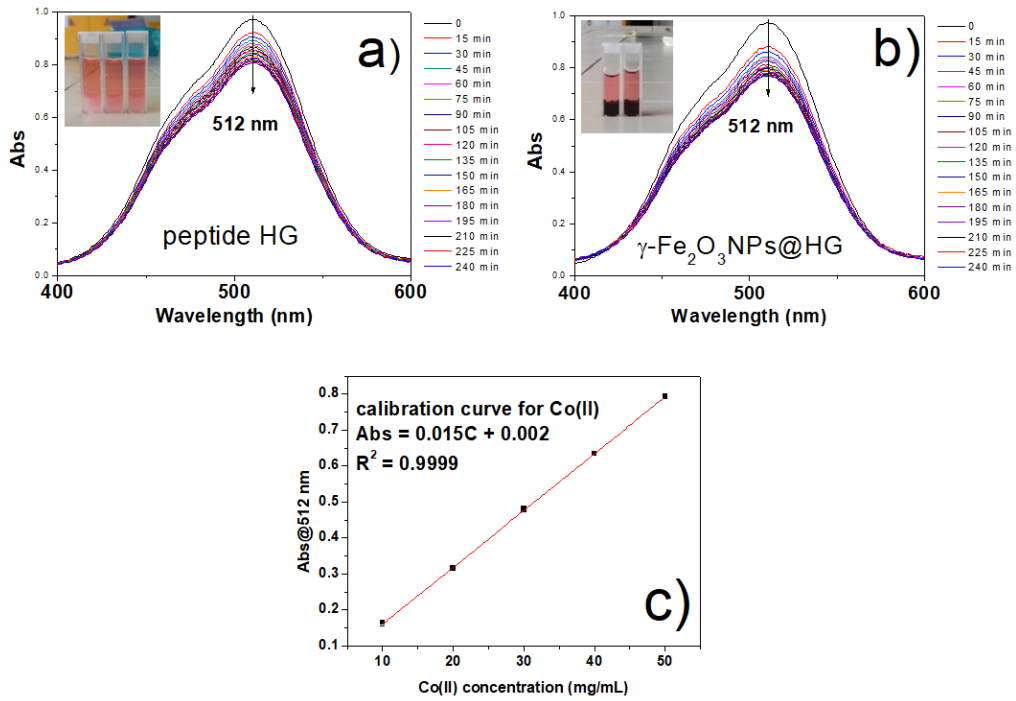

Figure S8. UV-Vis study of Co(II) adsorption for a) the peptide HG; b) γ-Fe_2O_3NPs@HG, and c) the calibration curve for Co(II) aqueous solutions.

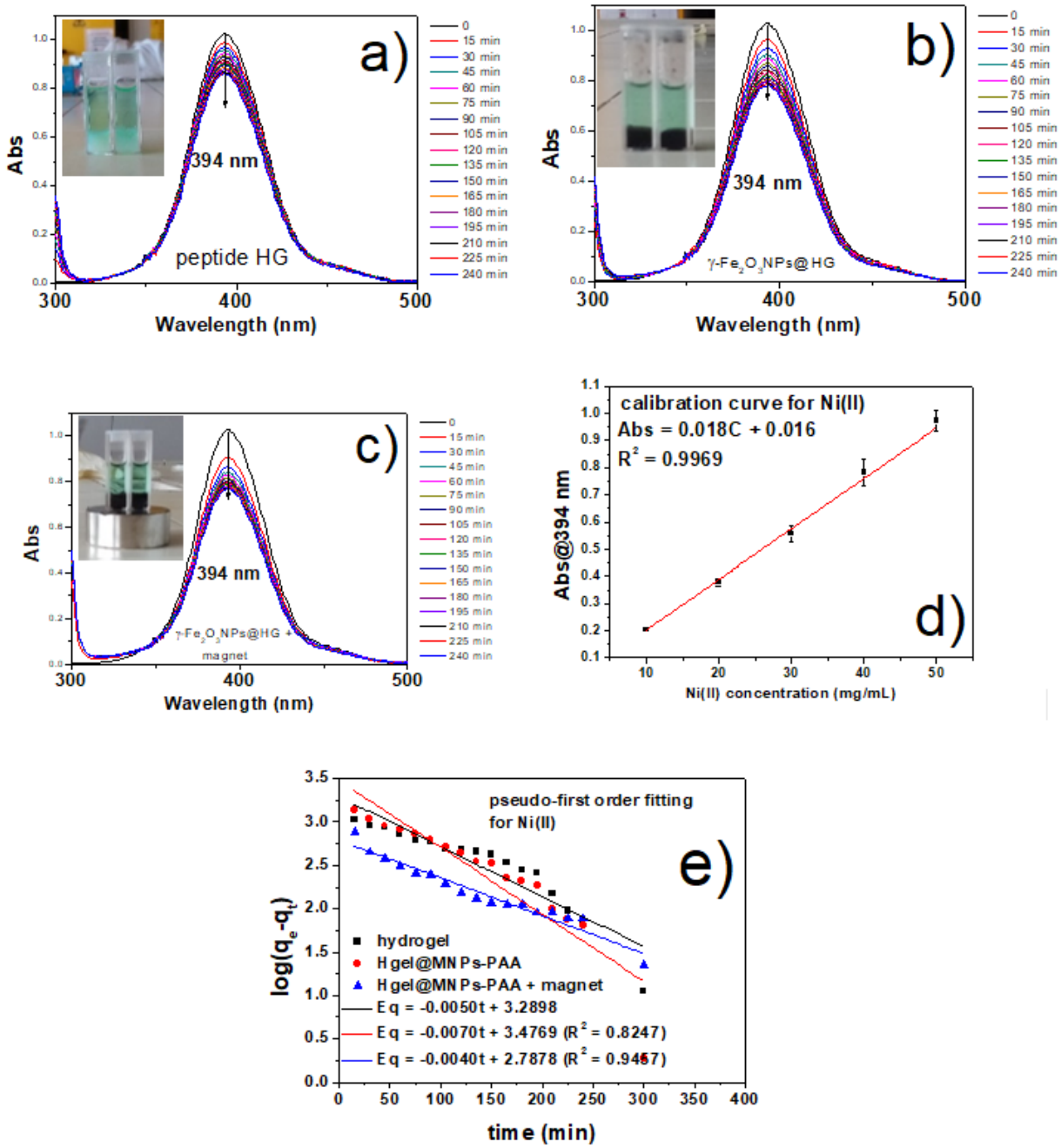

Figure S9. UV-Vis study of Ni(II) adsorption for a) the peptide HG; b) γ-Fe_2O_3NPs@HG; c) γ-Fe_2O_3NPs@HG upon magnetic field application; d) the calibration curve for Ni(II) aqueous solutions, and e) fit of kinetic data to pseudo-first order model for Ni(II).

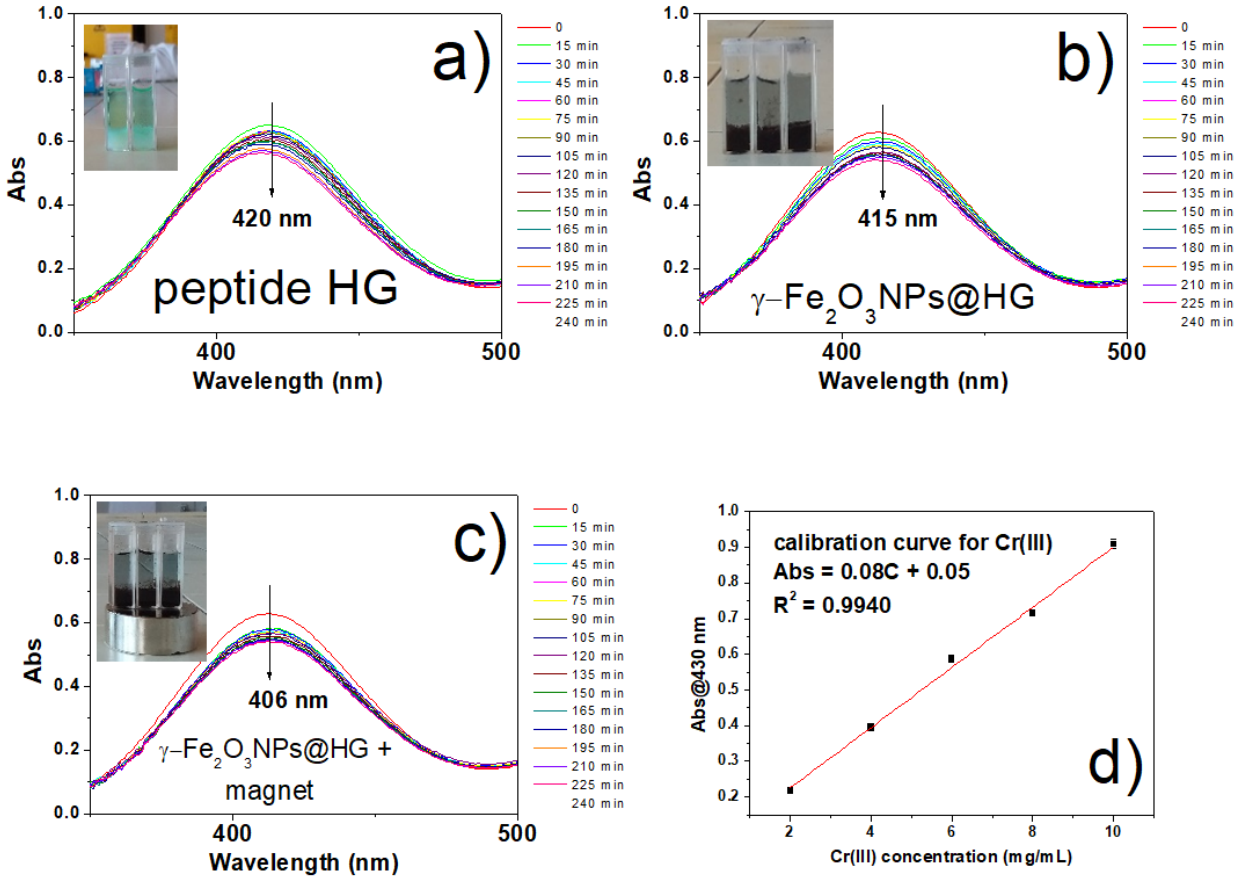

Figure S10. UV-Vis study of Cr(III) adsorption for a) the peptide HG; b) γ-Fe_2O_3NPs@HG; c) γ-Fe_2O_3NPs@HG upon magnetic field application and d) the calibration curve for Cr(III) aqueous solutions.

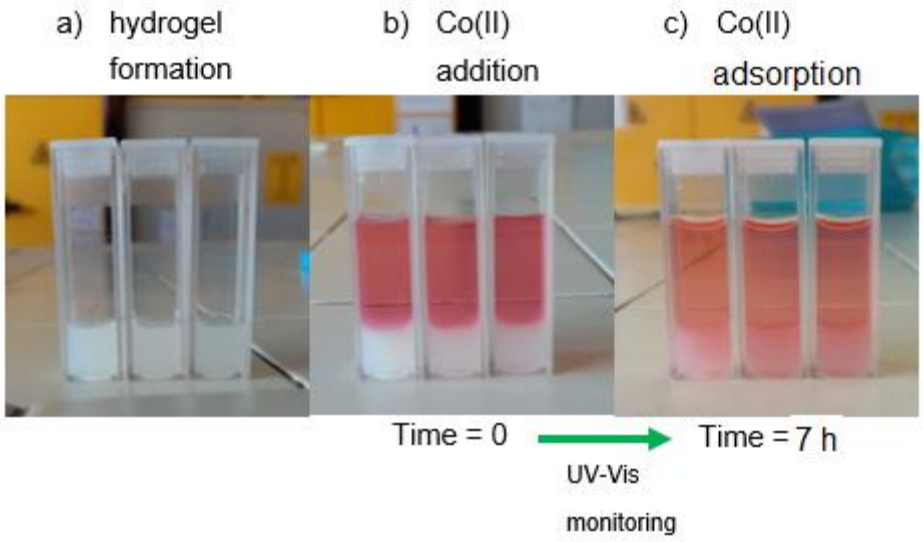

Figure S11. Methodology used for studying the removal efficiency of Co(II), as an example here.

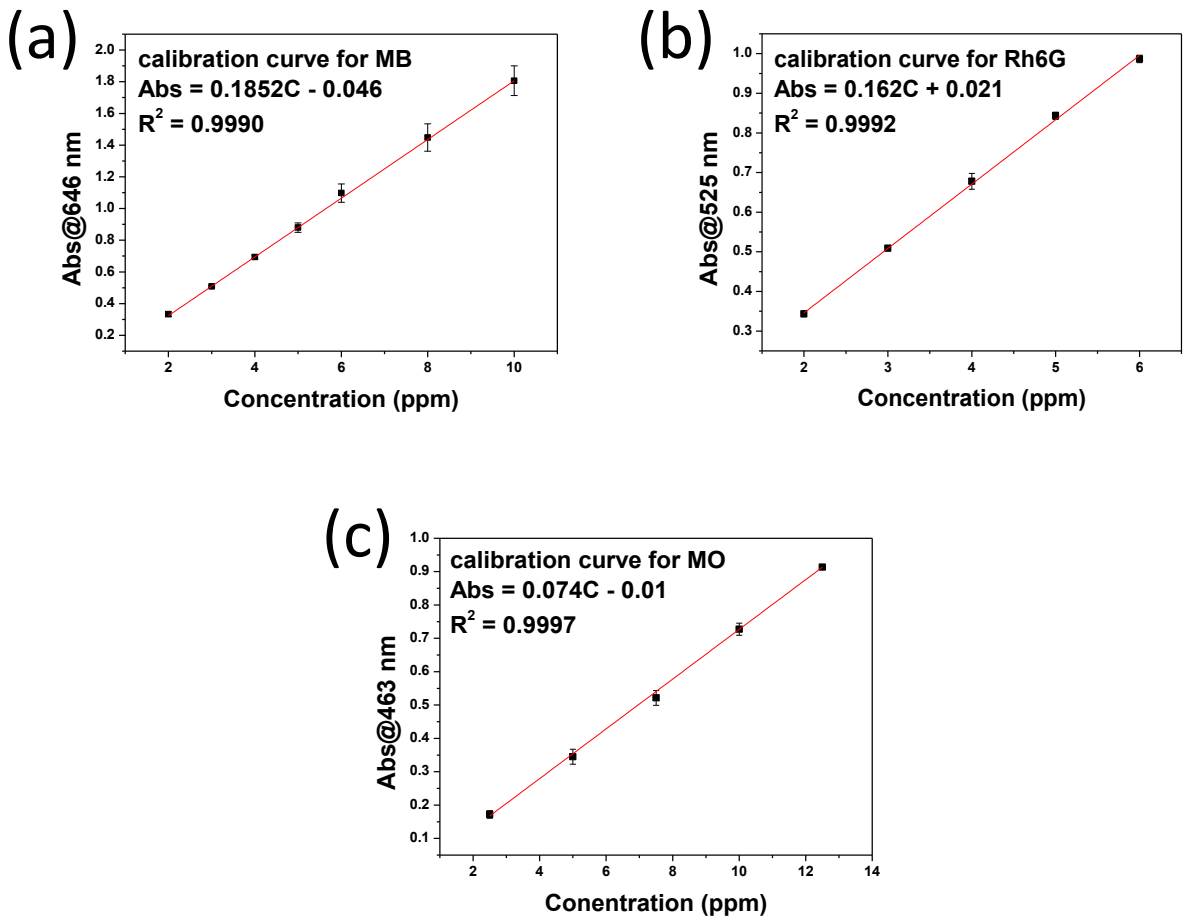

Figure S12. (a) Calibration curve of methylene blue (MB); (b) calibration curve of rhodamine 6G (R6G); (c) calibration curve of methyl orange (MO).

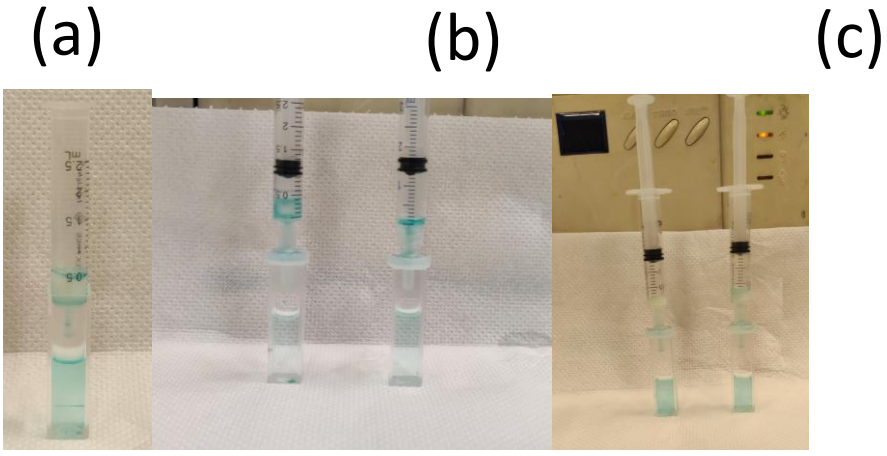

Figure S13. (a) Gravitational passage of MB through the gels inside the syringe; (b) gravitational passages with applying the filter in the outlet of the syringe; (c) gravitational passage with applying the filter and a constant pressureincrease the flow rate of the dye inside the syringe.

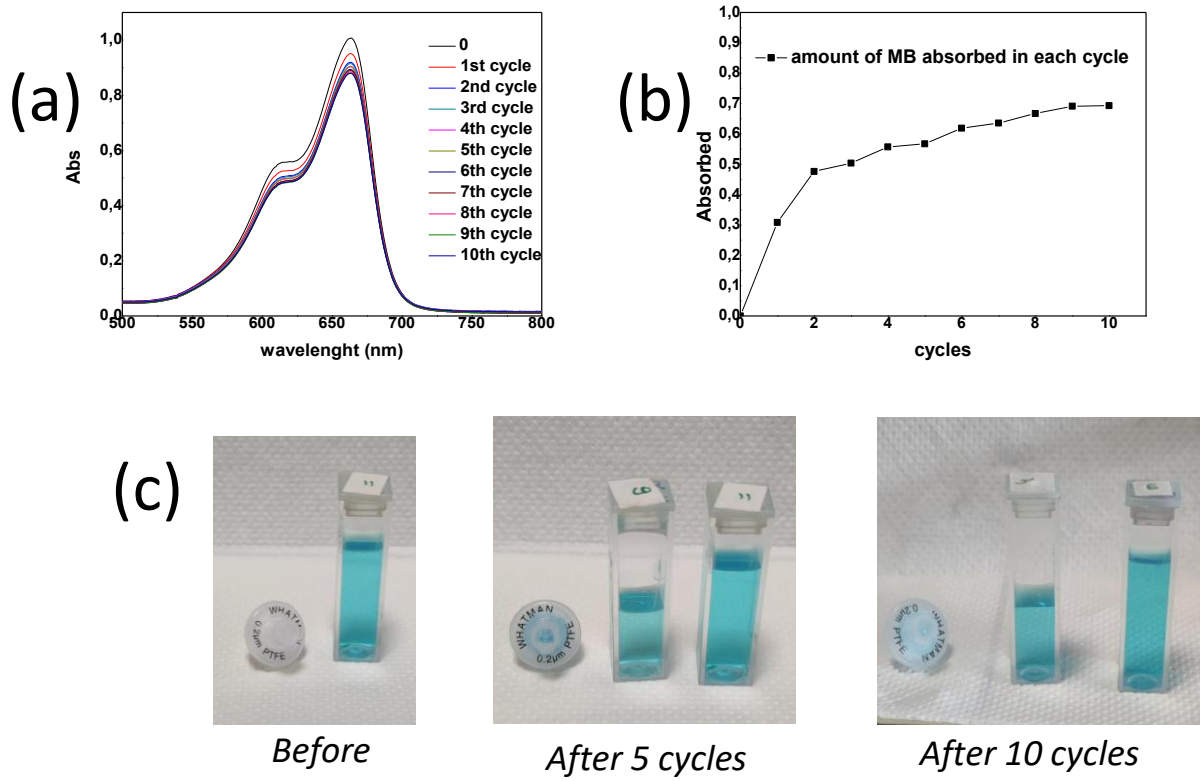

Figure S14. (a) Absorption of MB by the filter for different cycles; (b) amount of MB adsorbed by the filter in each cycle; (c) visual observation of the MB adsorption by the filter.

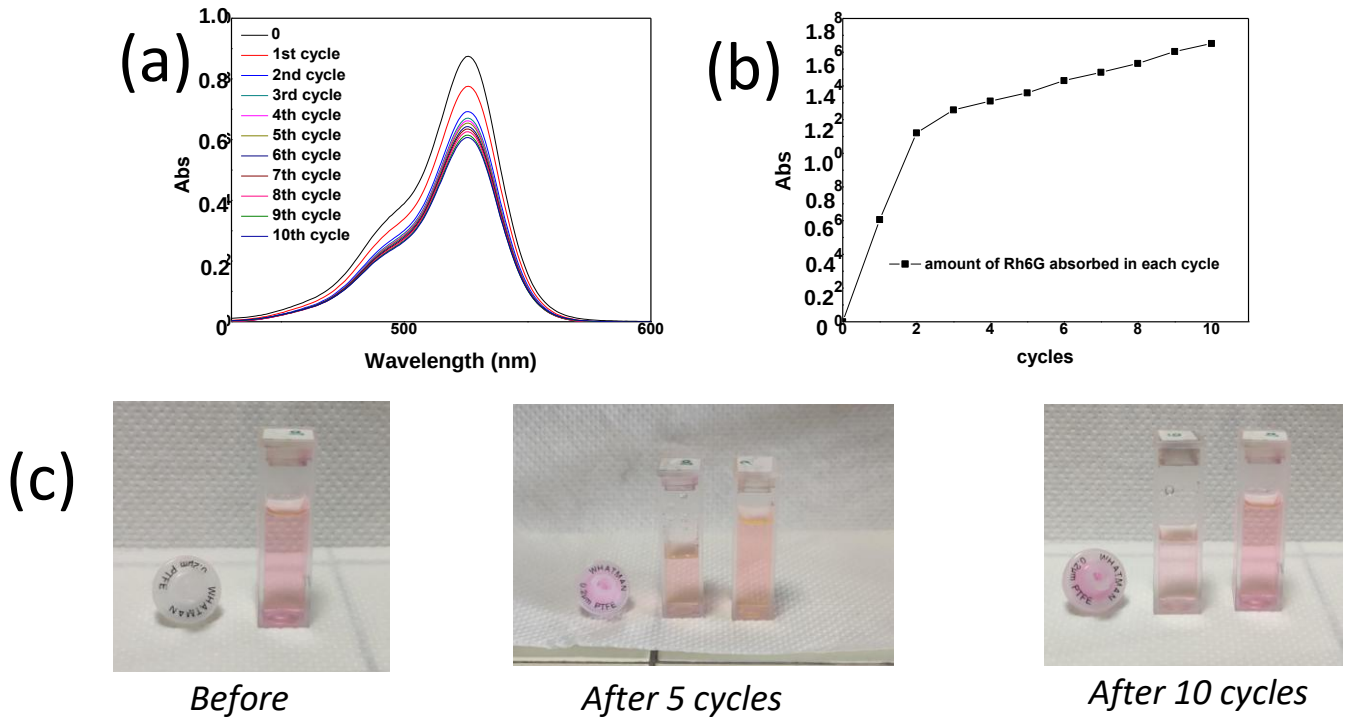

Figure S15. (a) Absorption of Rh6G by the filter for different cycles; (b) amount of Rh6G adsorbed by the filter in each cycle; (c) visual observation of the Rh6G adsorption by the filter.

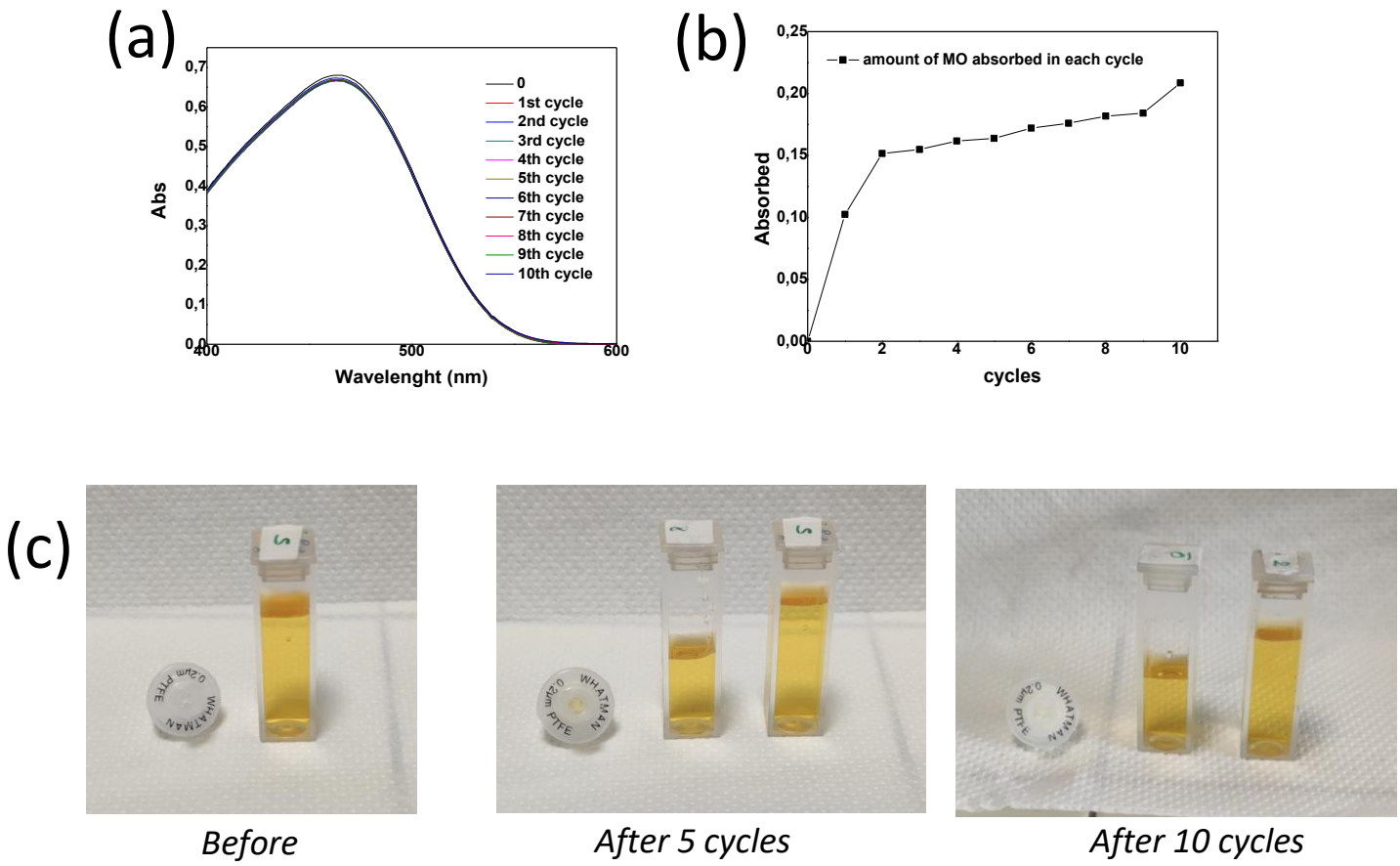

Figure S16. (a) Absorption of MO by the filter for different cycles; (b) amount of MO adsorbed by the filter in each cycle; (c) visual observation of the MO adsorption by the filter.

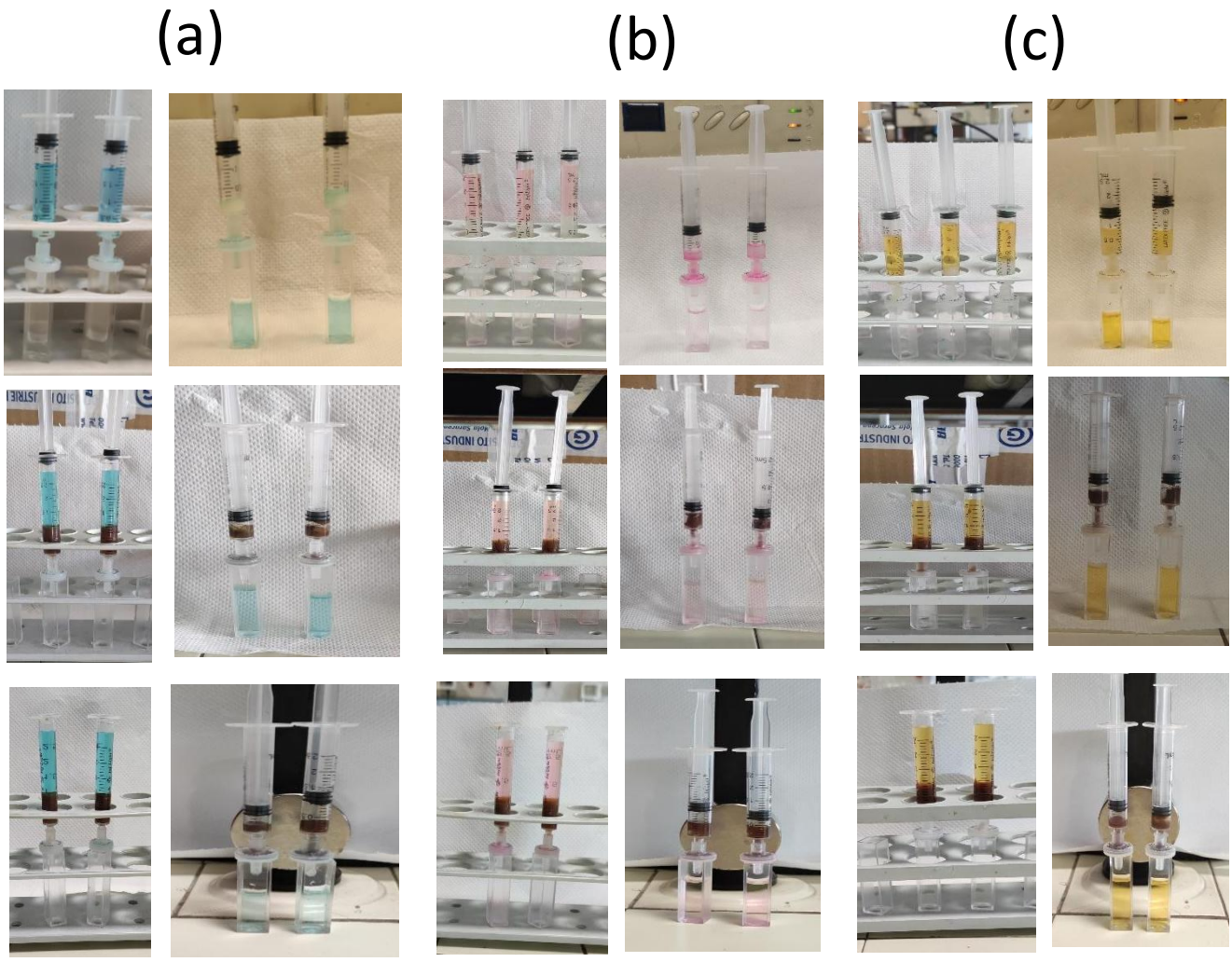

Figure S17. (a) Separation of the dyes by gel, γ-Fe_2O_3NPs@gel, and (γ-Fe_2O_3NPs@gel + mf) using the syringe with filter and external pressure for (a) MB; (b) Rh6G; (c) and MO.

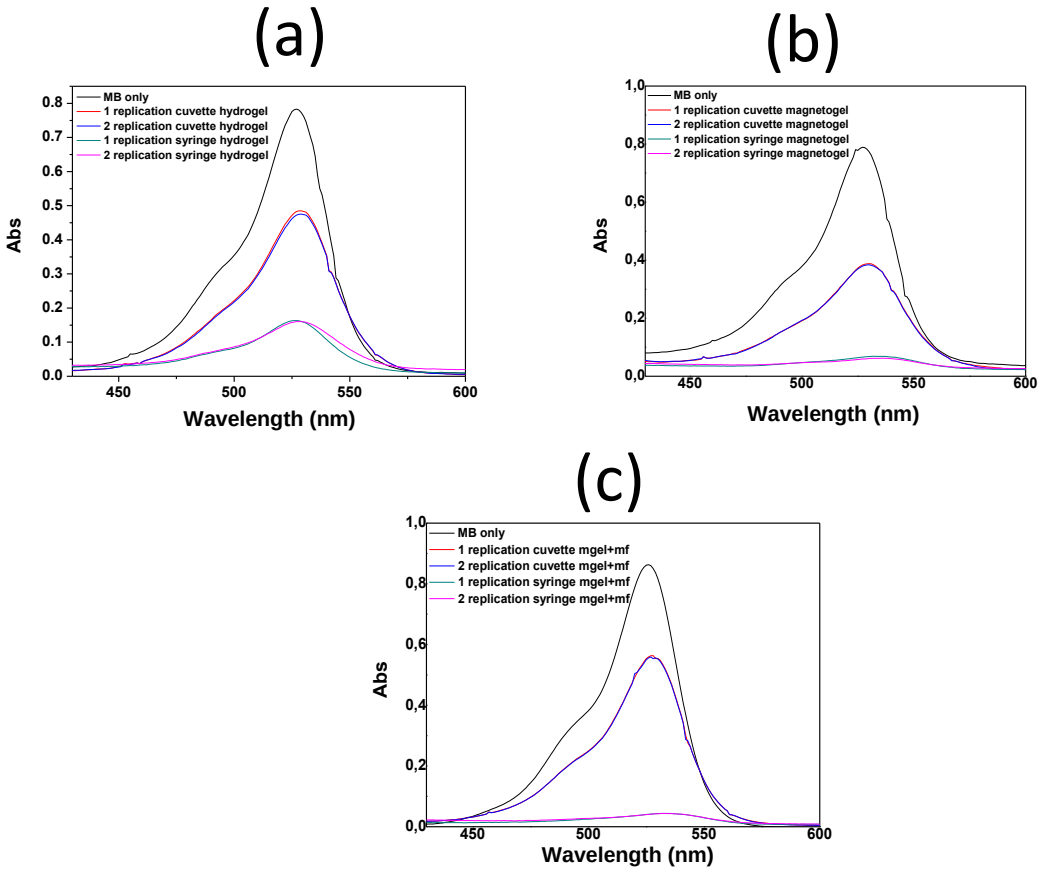

Figure S18. Comparison of the cuvette and syringe methodologies for absorption MB by (a) gel; (b) γ-Fe_2O_3NPs@gel; and (c) γ-Fe_2O_3NPs@gel + mf.

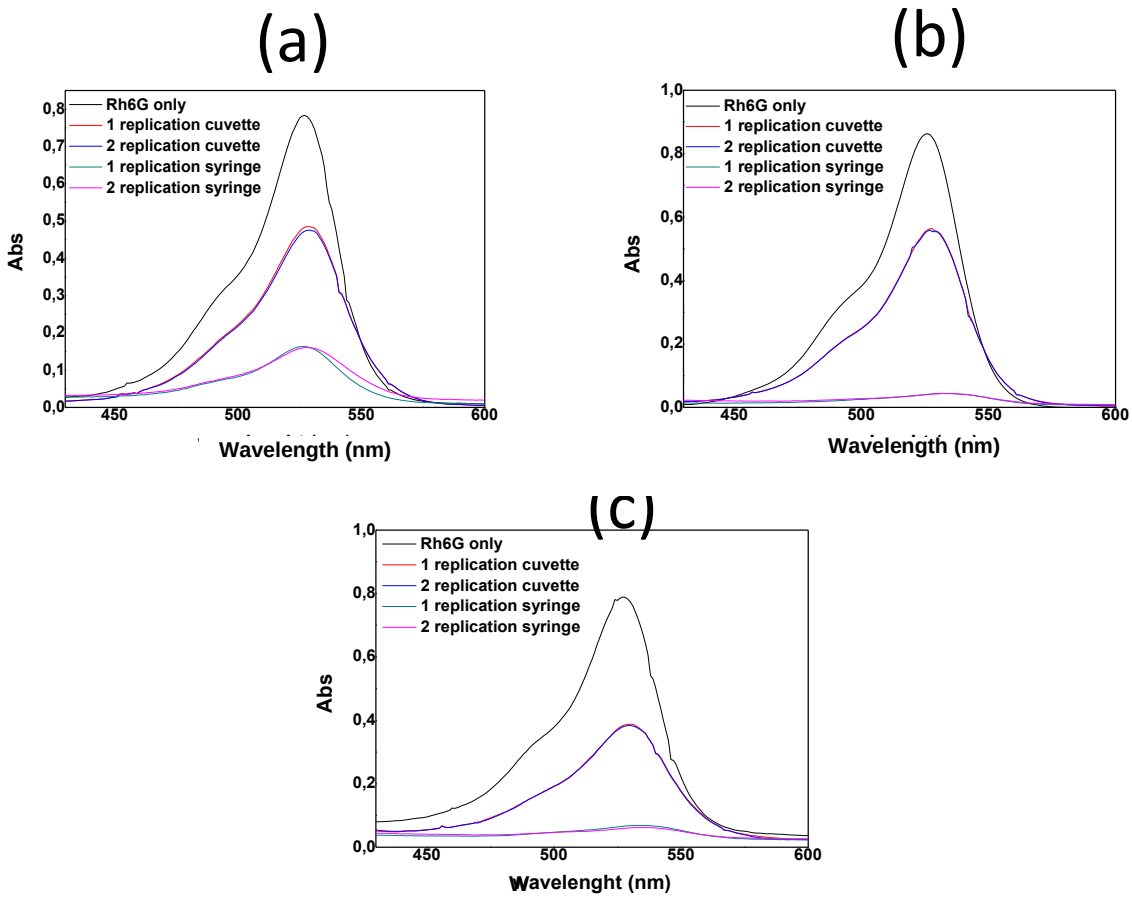

Figure S19. Comparison of the cuvette and syringe methodology for absorption Rh6G by (a) gel, (b) γ-Fe_2O_3NPs@gel, and (c) γ-Fe_2O_3NPs@gel + mf.

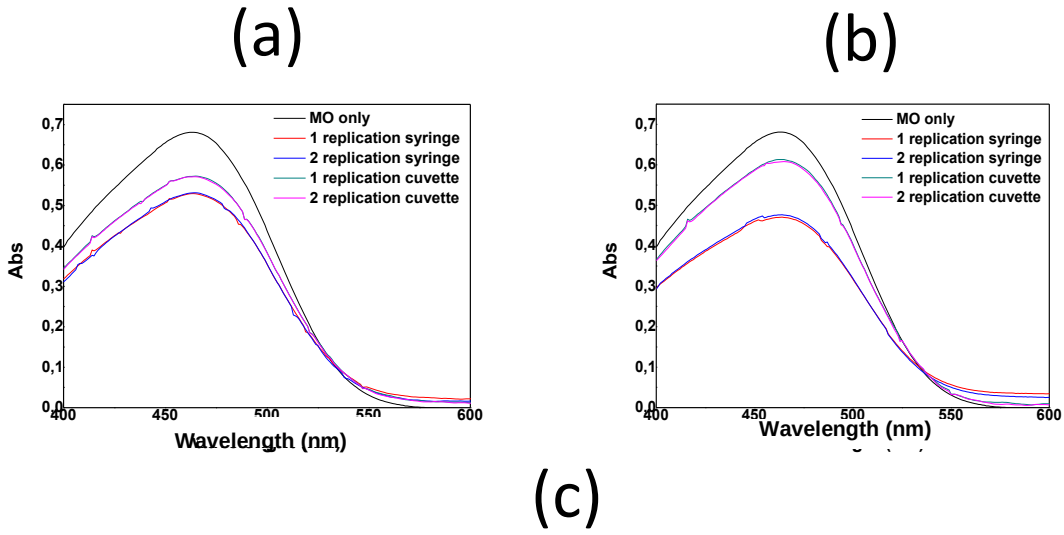

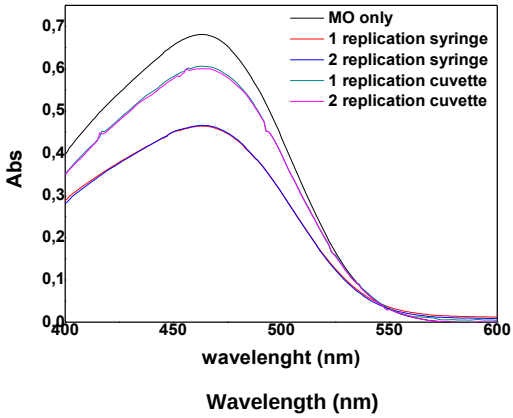

Figure S20. Comparison of the cuvette and syringe methodology for absorption MO by (a) gel; (b) γ-Fe_2O_3NPs@gel; and (c) γ-Fe_2O_3NPs@gel + mf.

Publications (2021-2024)

1- Farid Hajareh Haghighi, Roya Binaymotlagh, Paula Stefana Pintilei, Laura Chronopoulou , Cleofe Palocci, "Preparation of Peptide-Based Magnetogels for the Removal of Organic Dyes from Water", Gels, 2024, 10, 287, DOI: https://doi.org/10.3390/gels10050287.

2- Roya Binaymotlagh, Farid Hajareh Haghighi, Laura Chronopoulou , Cleofe Palocci, "Liposome@Hydrogel Composites for Controlled-Drug Delivery Applications", Gels, 2024, 10, 284, DOI: https://doi.org/10.3390/gels10040284.

3- Farid Hajareh Haghighi, Roya Binaymotlagh, Cleofe Palocci, Laura Chronopoulou, "Magnetic Iron Oxide Nanomaterials for Lipase Immobilization: Promising Industrial Catalysts for Biodiesel Production", Catalysts, 2024, 14, 336, DOI: https://doi.org/10.3390/catal14060336

4- Farid Hajareh Haghighi, Roya Binaymotlagh, Ilaria Fratoddi, Laura Chronopoulou, Cleofe Palocci, "Peptide-hydrogel nanocomposites for anti-cancer drug delivery", Gels, 2023, 9, 953, DOI: 10.3390/gels9120953.

5- Roya Binaymotlagh, Farid Hajareh Haghighi, Enea Gino Di Domenico, Francesca Sivori, Mauro Truglio, Alessandra Del Giudice, Ilaria Fratoddi, Laura Chronopoulou, Cleofe Palocci, "Biosynthesis of peptide hydrogels@titania nanoparticles composites with antibacterial properties", Gels, 2023, 9, 940, DOI: 10.3390/gels9120940.

6- Farid Hajareh Haghighi, Roya Binaymotlagh, Laura Chronopoulou, Sara Cerra, Andrea Giacomo Marrani, Francesco Amato, Cleofe Palocci, Ilaria Fratoddi, "Self-assembling peptide-based magnetogels for the removal of heavy metals from water", Gels, 2023, 9, 621, DOI: 10.3390/gels9080621.

7- Laura Chronopoulou, Roya Binaymotlagh, Sara Cerra, Farid Hajareh Haghighi, Enea Gino Di Domenico, Francesca Sivori, Ilaria Fratoddi, Silvano Mignardi, Cleofe Palocci, "Preparation of hydrogel composites using a sustainable approach for in situ silver nanoparticles formation", Materials, 2023, 16, 2134, DOI: 10.3390/ma16062134.

8- Roya Binaymotlagh, Laura Chronopoulou, Cleofe Palocci, "Peptide-Based Hydrogels: Template Materials for Tissue Engineering" Journal of Biofunctional Materials 2023, 14, 233, DOI: 10.3390/jfb14040233.

9- Farid Hajareh Haghighi, Martina Mercurio, Sara Cerra, Tommaso Alberto Salamone, Roya Binaymotlagh, Cleofe Palocci, Vincenzo Romano Spica, Ilaria Fratoddi, "Surface modification of TiO_2 nanoparticles with organic molecules and their biological applications", Journal of Materials Chemistry B, 2023, 11, 2334-2366, DOI: 10.1039/D2TB02576K.

10- Roya Binaymotlagh , Alessandra Del Giudice, Silvano Mignardi, Francesco Amato, Andrea Giacomo Marrani, Francesca Sivori, Ilaria Cavallo, Enea Gino Di Domenico, Cleofe Palocci, Laura Chronopoulou "Green In Situ Synthesis of Silver Nanoparticles-Peptide Hydrogel Composites: Investigation of Their Antibacterial Activities" Gels 2022, 8, 700, DOI: 10.3390/gels8110700.

11- Roya Binaymotlagh; Laura Chronopoulou; Farid Hajareh Haghighi; Ilaria Fratoddi; Cleofe Palocci "Peptide-Based Hydrogels: New Materials for Biosensing and Biomedical Applications" Materials 2022, 15, 5871, DOI: 10.3390/ma15175871.

References

[1] Volpi, M.; Paradiso, A.; Costantini, M.; Wojciech, S. Hydrogel-Based Fiber Biofabrication Techniques for Skeletal Muscle Tissue Engineering, *ACS Biomater. Sci. Eng.*, 2022, 8, 379, doi: 10.1021/acsbiomaterials.1c01145.

[2] Bustamante-torres, M.; Romero-fierro, D.; Arcentales-vera, B.; Palomino, K. Hydrogels Classification According to the Physical or Chemical Interactions and as Stimuli-Sensitive Materials, *Gels*, 2021, 7, 182, doi: 10.3390/gels7040182.

[3] Aswathy, S. H.; Uttamchand, N.; Inderchand, M. Commercial Hydrogels for Biomedical Applications, *Heliyon*, 2020, 6, e03719, 10.1016/j.heliyon.2020.e03719.

[4] Sikdar, P.; Uddin, M. M.; Dip, T. M.; Islam, S.; Hoque, M. S.; Dhar, A. K.; Wu, S. Recent Advances in the Synthesis of Smart Hydrogels, *Mater. Adv.*, 2021, 2, 4532, doi: 10.1039/D1MA00193K.

[5] Tang, G.; Tan, Z.; Zeng, W.; Wang, X.; Shi, C.; Liu, Y., He, H.; Chen, R.; Ye, X. Recent Advances of Chitosan-Based Injectable Hydrogels for Bone and Dental Tissue Regeneration, *Front. Bioeng. Biotechnol.*, 2020, 8, 587658, doi: 10.3389/fbioe.2020.587658.

[6] Rodríguez-Rodríguez, R.; Espinosa-Andrews, H.; Velasquillo-Martínez, C.; García-Carvajal, Z. Y. Composite Hydrogels Based on Gelatin, Chitosan and Polyvinyl Alcohol to Biomedical Applications: A Review, *Int. J. Polym. Mater. Polym. Biomater.*, 2020, 69, 1, doi: 10.1080/00914037.2019.1581780.

[7] Bustamante-Torres, M.; Romero-Fierro, D.; Arcentales-Vera, B.; Palomino, K.; Magaña, H.; Bucio, E. Hydrogels Classification According to the Physical or Chemical Interactions and as Stimuli-Sensitive Materials, *Gels*, 2021, 25, 7, 182, doi: 10.3390/gels7040182.

[8] Hajareh Haghighi, F.; Binaymotlagh, R.; Chronopoulou, L.; Cerra, S.; Marrani, A. G.; Amato, F.; Palocci, C.; Fratoddi, I. Self-Assembling Peptide-Based Magnetogels for the Removal of Heavy Metals from Water, *Gels*, 2023, 9, 8, 621, https://doi.org/10.3390/gels9080621.

[9] Catoira, M.C.; Fusaro, L.; Di Francesco, D.; Ramella, M.; Boccafoschi, F. Overview of Natural Hydrogels for Regenerative Medicine Applications, *J. Mater. Sci. Mater. Med.*, 2019, 30, 115, doi: 10.1007/s10856-019-6318-7.

[10] Gulrez, H.; Syed, K.; et al. Hydrogels: Methods of Preparation, Characterisation and Applications, Progress in Molecular and Environmental Bioengineering - From Analysis and Modeling to Technology Applications, *InTech*, 2011, doi:10.5772/24553.

[11] Binaymotlagh, R.; Chronopoulou, L.; Hajareh Haghighi, F.; Fratoddi, I.; Palocci, C. Peptide-Based Hydrogels: New Materials for Biosensing and Biomedical Applications, *Materials*, 2022, 25, 15, 5871, doi: 10.3390/ma15175871.

[12] Hauser, C. A.; Zhang, S. Designer Self-Assembling Peptide Nanofiber Biological Materials, *Chem. Soc. Rev*., 2010, **39,** 2780, doi: 10.1039/b921448h.

[13] Mandal, D.; Nasrolahi, A.; Shirazi, K. P. Self-Assembly of Peptides to Nanostructures, *Org. Biomol. Chem*., 2014, 12, 3544, doi: 10.1039/C4OB00447G.

[14] Fichman, G.; Gazit, E. Self-Assembly of Short Peptides to Form Hydrogels: Design of Building Blocks, Physical Properties and Technological Applications, *Acta Biomater.*, 2014, 10, 1671, doi: 10.1016/j.actbio.2013.08.013.

[15] Chen, J.; Zou, X. Self-Assemble Peptide Biomaterials and Their Biomedical Applications, *Bioact. Mater.*, 2019, 4, 120, doi: 10.1016/j.bioactmat.2019 01.002.

[16] Binaymotlagh, R.; Hajareh Haghighi, F.; Di Domenico, E. G.; Sivori, F.; Truglio, M.; Del Giudice, A.; Fratoddi, I.; Chronopoulou, L.; Palocci, C. Biosynthesis of Peptide Hydrogel-Titania Nanoparticle Composites with Antibacterial Properties, *Gels*, 2023, 9, 940, doi: https://doi.org/10.3390/gels9120940.

[17] Hamley, I. W. Self-Assembly, Bioactivity, and Nanomaterials Applications of Peptide Conjugates with Bulky Aromatic Terminal Groups, *ACS Applied Bio Materials*, 2023, *6*, 384, doi: 10.1021/acsabm.2c01041.

[18] Yang, Z. M. Using β-Lactamase to Trigger Supramolecular Hydrogelation. *J. Am. Chem. Soc*., 2007, 129, 266, doi: 10.1021/ja0675604.

[19] Toledano, S. R.; Williams, J.; Jayawarna, V.; Ulijn, R. V. Enzyme-Triggered Self-Assembly of Peptide Hydrogels via Reversed Hydrolysis, *J. Am. Chem. Soc.*, 2006, 128, 1070, doi: 10.1021/ja056549l.

[20] Hu, B. H.; and Messersmith, P. B. Rational Design of Transglutaminase Substrate Peptides for Rapid Enzymatic Formation of Hydrogels, *J. Am. Chem. Soc*., 2003, 125, 14298, doi: 10.1021/ja038593b.

[21] Gandhi, N. N. Applications of Lipase, *J. Am. Oil Chem. Soc*., 1997, 74, 621, doi: 10.1007/s11746-997-0194-x.

[22] Ollis, D. L.; Cheah, E.; Cygler, M.; Dijkstra, B.; Frolow, F.; Franken, S. M. et al.; The α/β Hydrolase Fold, *Protein Eng*., 1992, 5, 197, doi: 10.1093/protein/5.3.197.

[23] Mead, J. R.; Irvine, S. A.; Ramji, D. P.; Lipoprotein Lipase: Structure, Function, Regulation, and Role in Disease, *J. Mol. Med*. 2002, 80, 753, doi: 10.1007/s00109-002-0384-9.

[24] Fleming, S.; Ulijn, R.V. Design of Nanostructures Based on Aromatic Peptide Amphiphiles, *Chem. Soc. Rev.*, 2014, *43*, 8150, doi: 10.1039/C4CS00247D.

[25] Binaymotlagh, R.; Chronopoulou, L.; Palocci, C. Peptide-Based Hydrogels: Template Materials for Tissue Engineering, *J. Funct. Biomater.*, 2023, 14, 233, doi: https://doi.org/10.3390/jfb14040233.

[26] Chronopoulou, L.; Toumia, Y.; Cerroni, B.; Pandolfi, D.; Paradossi, G.; Palocci, C. Biofabrication of Genipin-Crosslinked Peptide Hydrogels and Their Use in the Controlled Delivery of Naproxen. *N. Biotechnol*. 2017, 37, 138, doi: 10.1016/j.nbt.2016.04.006.

[27] Correa, S.; Abigail K. G.; Hernandez, H. L.; Chan, D.; Yu, A. C.; Stapleton, L. M.; Eric A. Translational Applications of Hydrogels, *Chem. Rev.*, 2021, 121, 11385**,** doi: 10.1021/acs.chemrev.0c01177.

[28] Gudikandula, K.; Charya Maringanti, S. Synthesis of Silver Nanoparticles by Chemical and Biological Methods and Their Antimicrobial Properties, *J. Exp. Nanosci*., 2016, 11, 714, doi: 10.1080/17458080.2016.1139196.

[29] Griffin, S.; Masood, M.I.; Nasim, M.J.; Sarfraz, M.; Ebokaiwe, A.P.; Schafer, K.-H.; Keck, C. M.; Jacob, C. Natural Nano-Particles: A Particular Matter Inspired by Nature, *Antioxidants*, 2018, 7, E3, doi: 10.3390/antiox7010003.

[30] Li, Y.-M.; Wang, Y.-Y.; Cheng, B.-N. In-Vitro Cytotoxicity of Biosynthesized Gold Nanoparticles Against Thyroid Cancer Cell Lines, *Trop. J. Pharm. Res*., 2017, 16, 1523, doi: 10.4314/tjpr.v16i7.9.

[31] Yang, J.; Cao, W.; Rui, Y. Interactions Between Nanoparticles and Plants: Phytotoxicity and Defense Mechanisms, *J. Plant Interact*., 2017, 12, 158, doi: 10.1080/17429145.2017.1310944.

[32] Elmer, W.; White, J.C.; The Future of Nanotechnology in Plant Pathology, *Ann. Rev. Phytopathol*., 2018, 56, 111, doi: 10.1146/annurev-phyto-080417-050108.

[33] Zare, B.; Babaie, S.; Setayesh, N.; Shahverdi, A.R. Isolation and Characterization of a Fungus for Extracellular Synthesis of Small Selenium Nanoparticles, *Nanomed. J.*, 2013, 1, 14, doi: 10.7508/NMJ.2013.01.002.

[34] Tamulevičius T. Nanotechnologies in Textiles. *Materials*, 2022, 16, 1466, doi: 10.3390/ma15041466.

[35] Martínez, G.; Merinero, M.; Pérez-Aranda, M.; Pérez-Soriano, E.M.; Ortiz, T.; Begines, B.; Alcudia, A. Environmental Impact of Nanoparticles' Application as an Emerging Technology: A Review, *Materials*, 2020, 14, 166, doi: 10.3390/ma14010166.

[36] Aiello, A.; Morey, J.R.; Livi, K.J.T.; DeLong, H.C.; ElBidweihy, H.; Trulove, P.C.D.; David, P. Lignocellulose-Stabilized Iron-Palladium Nanomagnetic Biocomposites, *J. Magnet. Magnet. Mater.* 2020, 49, 165964, doi: 10.1016/j.jmmm.2019.165964.

[37] Thobakgale, L.; Ombinda-Lemboumba, S.; Mthunzi-Kufa, P. Chemical Sensor Nanotechnology in Pharmaceutical Drug Research, *Nanomaterials*, 2022, 12, 2688, doi: 10.3390/nano12152688.

[38] Joseph, T.M.; Kar Mahapatra, D.; Esmaeili, A.; Piszczyk, Ł.; Hasanin, M.S.; Kattali, M.; Haponiuk, J.; Thomas, S. Nanoparticles: Taking a Unique Position in Medicine. *Nanomaterials*, 2023, 13, 574, doi: 10.3390/nano13030574.

[39] Paluszkiewicz, P.; Martuszewski, A.; Zaręba, N.; Wala, K.; Banasik, M.; Kepinska, M. The Application of Nanoparticles in Diagnosis and Treatment of Kidney Diseases, *Int. J. Mol. Sci.*, 2021, 23, doi: 10.3390/ijms23010131.

[40] Madkour, L.H. Introduction to Nanotechnology (NT) and Nanomaterials (NMs), *Nanoelectron. Mater.*, 2019, 116, 1, doi: 10.1007/978-3-030-21621-4_1.

[41] Saleh, T.A. Nanomaterials: Classification, Properties, and Environmental Toxicities. *Environ. Technol. Innov.* 2020, 20, 101067, doi: 10.1016/j.eti.2020.101067.

[42] Nowack, B.; Bucheli, T.D. Occurrence, Behavior and Effects of Nanoparticles in the Environment. *Environ. Pollut.*, 2007, 150, 5, doi: 10.1016/j.envpol.2007.06.006.

[43] Kumar Teli, M.; Mutalik, S.; Rajanikant, G.K. Nanotechnology and Nanomedicine: Going Small Means Aiming Big, *Curr. Pharm. Des.*, 2010, 16, 1882, doi: 10.2174/138161210791208992.

[44] Bordea, I.R.; Candrea, S.; Alexescu, G.T.; Bran, S.; Băciuț, M.; Băciuț, G.; Lucaciu, O.; Dinu, C.M.; Todea, D.A. Nano-Hydroxyapatite Use in Dentistry: A Systematic Review, *Drug Metab. Rev.*, 2020, 52, 319, doi: 10.1080/03602532.2020.1758713.

[45] Ma Y., Cai F., Li Y., Chen J., Han F., Lin W. A Review of the Application of Nanoparticles in the Diagnosis and Treatment of Chronic Kidney Disease. *Bioact. Mater.* 2020;5:732, doi: 10.1016/j.bioactmat.2020.05.002.

[46]Gholizadeh, O.; Yasamineh, S.; Amini, P.; Afkhami, H.; Delarampour, A.; Akbarzadeh, S.; Karimi Matloub, R.; Zahedi, M.; Hosseini, P.; Hajiesmaeili, M.; Poortahmasebi, V. Therapeutic and Diagnostic Applications of Nanoparticles in the Management of COVID-19: A Comprehensive Overview. *Virol J.*, 2022, 19, 206, doi: 10.1186/s12985-022-01935-7.

[47] Chronopoulou, L.; Binaymotlagh, R.; Cerra, S.; Hajareh Haghighi, F.; Di Domenico, E. G.; Sivori, F.; Fratoddi, I.; Mignardi, S.; Palocci C. Preparation of Hydrogel Composites Using a Sustainable Approach for In Situ Silver Nanoparticles Formation, *Materials*, 2023, 16, 2134, doi: 10.3390/ma16062134.

[48] Ferrari, M.; Cancer Nanotechnology: Opportunities and Challenges, *Nat. Rev. Cancer*, 2005, **5**, 161, doi:10.1038/nrc1566.

[49] Duncan, R.; The Dawning Era of Polymer Therapeutics, *Nat. Rev. Drug Disc.*, 2003, **2**, 347, doi: 10.1038/nrd1088.

[50] De Jong, W. H.; Borm, P. J.; Drug Delivery and Nanoparticles: Applications and Hazards, *Int. J. Nanomedicine*, 2008, 3, 133, doi: 10.2147/ijn.s596.

[51] Herranz, F.; Almarza, E.; Rodríguez, I.; Salinas, B.; Rosell, Y.; Desco, M.; Bulte, J. W.; Ruiz-Cabello, J.; The Application of Nanoparticles in Gene Therapy and Magnetic Resonance Imaging, *Microsc. Res. Tech*. 2011, 74, 577, doi: 10.1002/jemt.20992.

[52] Lockman, P.R.; Mumper, R. J.; Khan, M. A.; Allen, D. D. Nanoparticle Technology for Drug Delivery Across the Blood-Brain Barrier, *Drug Dev. Ind. Pharm.*, 2002, 28, 1, doi: 10.1081/ddc-120001481.

[53] Binaymotlagh, R.; Hadadzadeh, H.; Farrokhpour, H.; Hajareh Haghighi, F.; Abyar, F.; Mirahmadi-Zare, S. Z. In Situ Generation of the Gold Nanoparticles-Bovine Serum Albumin (AuNPs–BSA) Bioconjugated System Using Pulsed-Laser Ablation (PLA), *Mat. Chem. Phys.*, 2016, 177, 360, doi: 10.1016/j.matchemphys.2016.04.040.

[54] Sanità, G.; Carrese, B.; Lamberti, A. Nanoparticle Surface Functionalization: How to Improve Biocompatibility and Cellular Internalization, *Front. Mol. Biosci.*, 2020, 7, doi: 10.3389/fmolb.2020.587012.

[55] Cano, A.; Ettcheto, M.; Chang, J.H.; Barroso, E.; Espina, M.; Kuhne, B.A.; Barenys, M.; Auladell, C.; Folch, J.; Souto, E.B. Dual-Drug Loaded Nanoparticles of Epigallocatechin-3-Gallate (EGCG)/Ascorbic Acid

Enhance Therapeutic Efficacy of EGCG in a APPswe/PS1dE9 Alzheimer's Disease Mice Model. *J. Control. Release,* 2019, 301, 62, doi: 10.1016/j.jconrel.2019.03.010.

[56] Cano, A.; Sánchez-López, E.; Ettcheto, M.; López-Machado, A.; Espina, M.; Souto, E.B.; Galindo, R.; Camins, A.; García, M.L.; Turowski, P. Current Advances in the Development of Novel Polymeric Nanoparticles for the Treatment of Neurodegenerative Diseases. *Nanomed.,* 2020, 15, 1239, doi: 10.2217/nnm-2019-0443.

[57] Soppimath, K.S.; Aminabhavi, T.M.; Kulkarni, A.R.; Rudzinski, W.E. Biodegradable Polymeric Nanoparticles as Drug Delivery Devices. *J. Control. Release.,* 2001, 70, 1, doi: 10.1016/S0168-3659(00)00339-4.

[58] wens III, D.E.; Peppas, N.A. Opsonization, Biodistribution, and Pharmacokinetics of Polymeric Nanoparticles. *Int. J. Pharm.,* 2006, 307, 93, doi: 10.1016/j.ijpharm.2005.10.010.

[59] Zielińska, A.; Carreiró, F.; Oliveira, A.M.; Neves, A.; Pires, B.; Venkatesh, D.N.; Durazzo, A.; Lucarini, M.; Eder, P.; Silva, A.M.; Santini, A.; Souto, E.B. Polymeric Nanoparticles: Production, Characterization, Toxicology and Ecotoxicology. *Molecules,* 2020, 25, 3731, doi: 10.3390/molecules25163731.

[60] Alam, M.W.; Qurashi, A. Metal Chalcogenide Quantum Dots for Hybrid Solar Cell Applications. In: Qurashi A, ed. Metal Chalcogenide Nanostructures for Renewable Energy Applications. Massachusetts: Scrivener Publishing LLC, 2014, 233, doi: 10.1002/9781119008934.ch10.

[61] Wang, H.; Zhang, F; Wen, H.; Shi, W.; Huang, Q.; Huang, Y. Tumor- and Mitochondria-Targeted Nanoparticles Eradicate Drug Resistant Lung Cancer Through Mitochondrial Pathway of Apoptosis. *J. Nanobiotechnology.* 2020, 18, 8, doi: 10.1186/s12951-019-0562-3.

[62] Bhatti, R.; Shakeel, H.; Malik, K.; Qasim, M.; Khan, M.A.; Ahmed, N.; Jabeen, S. Inorganic Nanoparticles: Toxic Effects, Mechanisms of Cytotoxicity and Phytochemical Interactions, *Adv. Pharm. Bull*., 2022, 12, 757, doi: 10.34172/apb.2022.077.

[63] Mazur, F.; Bally, M.; Städler, B.; Chandrawati, R. Liposomes and Lipid Bilayers in Biosensors. *Adv. Colloid. Interface Sci.,* 2017, 249, 88, doi: 10.1016/j.cis.2017.05.020.

[64] Wang, G.; Li, R.; Parseh, B.; Du, G. Prospects and Challenges of Anticancer Agents' Delivery via Chitosan-Based Drug Carriers to Combat Breast Cancer: A Review. *Carbohydr. Polym.* 2021, 268, 118192, doi: 10.1016/j.carbpol.2021.118192.

[65] Man, F.; Gawne, P.J.; de Rosales, R.T.M. Nuclear Imaging of Liposomal Drug Delivery Systems: A Critical Review of Radiolabelling Methods and Applications in Nanomedicine, *Adv. Drug Delivery Rev.*. 2019, 143, 134, doi: 10.1016/j.addr.2019.05.012.

[66] Mirzavi, F.; Barati, M.; Soleimani, A.; Vakili-Ghartavol, R.; Jaafari, M.R.; Soukhtanloo, M. A. Review on Liposome-Based Therapeutic Approaches Against Malignant Melanoma, *Int. J. Pharm.,* 2021, 599, 120413, doi: 10.1016/j.ijpharm.2021.120413.

[67] Zenze, M.; Daniels, A.; Singh, M. Denmers as Modifiers of Inorganic Nanoparticles for Therapeutic Delivery in Cancer, *Pharmaceutics*, 2023, 15, 398, doi: 10.3390/pharmaceutics15020398.

[68] Altammar, K. A. A Review on Nanoparticles: Characteristics, Synthesis, Applications, and Challenges, *Front Microbiol*, 2023, 14, 1155622, doi: 10.3389/fmicb.2023.1155622.

[69] Barillo, D. J.; Marx, D. E. Silver in Medicine: a Brief History BC 335 to Present. *Burns.,* 2014, 40, S3, doi: 10.1016/j.burns.2014.09.009.

[70] Asgary, V.; Shoari, A.; Baghbani-Arani, F.; Sadat Shandiz, S. A.; Khosravy, M. S.; Janani, A.; et al., Green Synthesis and Evaluation of Silver Nanoparticles as Adjuvant in Rabies Veterinary Vaccine. *Int. J. Nanomedicine,* 2016, 11, 3597, doi: 10.2147/IJN.S109098. eCollection 2016.

[71] Xu, L.; Wang, Y. Y.; Huang, J.; Chen, C.Y.; Wang, Z.X.; Xie, H. Silver Nanoparticles: Synthesis, Medical Applications and Biosafety, *Theranostics*, 2020, 10, 8996, doi: 10.7150/thno.45413.

[72] Deshpande, L. M.; Chopade, B. A. Plasmid Mediated Silver Resistance in Acinetobacter baumannii, *Biometals,* 1994, 7, 49, doi: 10.1007/BF00205194.

[73] Klaus, T.; Joerger, R.; Olsson, E.; Granqvist, C-G. Silver-Based Crystalline Nanoparticles, Microbially Fabricated. *Proc. Natl. Acad. Sci. India. Sect. B. Biol. Sci.,* 1999, 96, 13611, doi: 10.1073/pnas.96.24.13611.

[74] Abbaszadegan, A.; Ghahramani, Y.; Gholami, A.; Hemmateenejad, B.; Dorostkar, S.; Nabavizadeh, M. et al. The Effect of Charge at the Surface of Silver Nanoparticles on Antimicrobial Activity Against Gram-Positive and Gram-Negative Bacteria: A Preliminary Study, *J. Nanomater.,* 2015, 16, 53, https://doi.org/10.1155/2015/720654.

[75] Hamedi, S.; Ghaseminezhad, M.; Shokrollahzadeh, S.; Shojaosadati, S. A.; Controlled Biosynthesis of Silver Nanoparticles Using Nitrate Reductase Enzyme Induction of Filamentous Fungus and Their Antibacterial Evaluation, *Artif. Cells Nanomed. Biotechnol.,* 2017, 45, 1588, doi: 10.1080/21691401.2016.1267011.

[76] Haseeb, M.; Khan, M. S.; Baker, A.; Khan, I.; Wahid, I.; Jaabir, M. M. Anticancer and Antibacterial Potential of MDR *Staphylococcus aureus* Mediated Synthesized Silver Nanoparticles, *Biosci. Biotech. Res. Comm.,* 2019, 12, 26, doi: http://dx.doi.org/10.21786/bbrc/12.1/4.

[77] Saratale, G. D.; Saratale, R. G.; Benelli, G.; Kumar, G.; Pugazhendhi, A.; Kim, D-S; et al., Anti-Diabetic Potential of Silver Nanoparticles Synthesized with *Argyreia nervosa* Leaf Extract High Synergistic Antibacterial Activity with Standard Antibiotics Against Foodborne Bacteria, *.J Clust. Sci.,* 2017, 28, 1709, doi:10.1007/s10876-017-1179-z.

[78] Yin, I. X.; Zhang, J.; Zhao, I. S.; Mei, M. L.; Li, Q.; Chu, C. H. The Antibacterial Mechanism of Silver Nanoparticles and Its Application in Dentistry. *Int. J. Nanomedicine*, 2020, 15, 2555, doi: 10.2147/IJN.S246764.

[79] Benjamin, L. O.; Francesco, S. Antibacterial Activity of Silver Nanoparticles: A Surface Science Insight, *Nano Today*, 2015, 10, 339, doi: 10.1016/j.nantod.2015.04.002.

[80] Lee, S.H.; Rho, W.-Y.; Park, S.J.; Kim, J.; Kwon, O.S.; Jun, B.-H. Multifunctional Self-Assembled Monolayers via Microcontact Printing and Degas-Driven Flow Guided Patterning, *Sci. Rep.*, 2018, 8, 16763, doi: 10.1038/s41598-018-35195-9.

[81] Millstone, J. E.; Hurst, S. J.; Métraux, G. S.; Cutler, J. I.; Mirkin. C. A. Colloidal Gold and Silver Triangular Nanoprisms, *Small.,* 2009, 5, 646, doi: 10.1002/smll.200801480.

[82] Ouay, B. L.; Stellacci, F. Antibacterial activity of silver nanoparticles: A Surface Science Insight, *Nano Today,* 2015, 10, 339, doi: 10.1016/j.nantod.2015.04.002.

[83] Sun, Y.; Mayers, B.; Herricks, T.; Xia, Y. Polyol Synthesis of Uniform Silver Nanowires: A Plausible Growth Mechanism and the Supporting Evidence, *Nano Lett.,* 2003, 3, 955, doi: 10.1021/nl034312m.

[84] Chen, D.; Qiao, X.; Qiu, X.; Chen, J. Synthesis and Electrical Properties of Uniform Silver Nanoparticles for Electronic Applications, *J. Mater. Sci.,* 2009, 44, 1076, doi: 10.1007/s10853-008-3204-y.

[85] Lee, S. H.; Jun, B. H. Silver Nanoparticles: Synthesis and Application for Nanomedicine, *Int. J. Mol. Sci*., 2019 20, 865, doi: 10.3390/ijms20040865.

[86] Mokhena T.C., Luyt A.S. Electrospun Alginate Nanofibres Impregnated with Silver Nanoparticles: Preparation, Morphology and Antibacterial Properties. *Carbohydr. Polym.,* 2017, 304, doi: 10.1016/j.carbpol.2017.02.068.

[87] Gudikandula, K.; Vadapally, P.; Singara Charya, M. A. Biogenic Synthesis of Silver Nanoparticles From White Rot Fungi: Their Characterization and Antibacterial Studies, *OpenNano.,* 2017, 2, 64, doi: 10.1016/j.onano.2017.07.002.

[88] Burdușel, A.C.; Gherasim, O.; Grumezescu, A. M.; Mogoantă, L.; Ficai, A.; Andronescu, E. Biomedical Applications of Silver Nanoparticles: An Up-to-Date Overview. *Nanomaterials*, 2018, 8, 681, doi: 10.3390/nano8090681.

[89] Zhang, X.; Zhi-Guo, L.; Wei, S.; Sangiliyandi, G. Silver Nanoparticles: Synthesis, Characterization, Properties, Applications, and Therapeutic Approaches, *Int. Jour. Molec. Sci.,* 2016, 17, 1534, https://doi.org/10.3390/ijms17091534.

[90] Amendola, V.; Meneghetti, M. Laser Ablation Synthesis in Solution and Size Manipulation of Noble Metal Nanoparticles. *Phys. Chem. Chem. Phys.* 2009;11, 3805, doi: 10.1039/b900654k.

[91] Iravani, S.; Korbekandi, H.; Mirmohammadi, S.V.; Zolfaghari, B. Synthesis of Silver Nanoparticles: Chemical, Physical and Biological Methods, *Res. Pharm. Sci.,* 2014, 9, 385, PMID: 26339255.

[92] Chugh, H.; Sood, D.; Chandra, I.; Tomar, V.; Dhawan, G.; Chandra, R. Role of Gold and Silver Nanoparticles in Cancer Nanomedicine, *Artif. Cell. Nanomed. Biotechnol.,* 2018, 46, 1210, doi: 10.1080/21691401.2018.1449118.

[93] Lee, S. H.; Jun, B. H. Silver Nanoparticles: Synthesis and Application for Nanomedicine, *Int. J. Mol. Sci*. 2019, 20, 865. doi: 10.3390/ijms20040865.

[94] Kumar, A.; Vemula, P. K.; Ajayan, P.M.; John, G. Silver-Nanoparticle-Embedded Antimicrobial Paints Pased on Vegetable Oil, *Nat. Mater.,* 2008, 7, 236, doi: 10.1038/nmat2099.

[95] Klaus-Joerger, T.; Joerger, R.; Olsson, E.; Granqvist, C.-G. Bacteria as Workers in the Living Factory: Metal-Accumulating Bacteria and Their Potential for Materials Science, *Trends. Biotechnol.,* 2001, 19, 15, doi: 10.1016/S0167-7799(00)01514-6.

[96] Arokiyaraj, S.; Vincent, S.; Saravanan, M.; Lee, Y.; Oh, Y.K.; Kim, K.H. Green Synthesis of Silver Nanoparticles Using *Rheum palmatum* Root Extract and Their Antibacterial Activity Against *Staphylococcus aureus* and *Pseudomonas aeruginosa*, *Artif. Cells Nanomed. Biotechnol.,* 2016, 45, 372, doi: 10.3109/21691401.2016.1160403.

[97] Gurunathan, S.; Kalishwaralal, K.; Vaidyanathan, R.; Venkataraman, D.; Pandian, S. R.; Muniyandi, J.; Hariharan, N.; Eom, S.H. Biosynthesis, Purification and Characterization of Silver Nanoparticles Using *Escherichia coli*, *Colloids Surf. B Biointerfaces,* 2009, 74, 328, doi: 10.1016/j.colsurfb.2009.07.048.

[98] Kalimuthu, K.; Babu, R.S.; Venkataraman, D.; Bilal, M.; Gurunathan, S. Biosynthesis of Silver Nanocrystals by *Bacillus licheniformis*, *Colloid Surface B.,* 2008, 65, 150, doi: 10.1016/j.colsurfb.2008.02.018.

[99] Shankar, S. S.; Ahmad, A.; Sastry, M. Geranium Leaf Assisted Biosynthesis of Silver Nanoparticles, *Biotechnol. Prog.,* 2003, 19, 1627, doi: 10.1021/bp034070w.

[100] Ahmed, A-A.; Hamzah, H.; Maaroof, M. Analyzing Formation of Silver Nanoparticles from the Filamentous Fungus *Fusarium oxysporum* and Their Antimicrobial Activity, *Turk J Biol.,* 2018, 42, 54, doi: 10.3906/biy-1710-2.

[101] Alassali, A.; Cybulska, I.; Brudecki, G. P.; Farzanah, R.; Thomsen, M. H. Methods for Upstream Extraction and Chemical Characterization of Secondary Metabolites from Algae Biomass, *Adv. Tech. Biol. Med.*, 2016, 1, doi: 10.4172/2379-1764.1000163.

[102] Gurunathan, S.; Han, J.; Park, J. H.; Kim, J. H. A Green Chemistry Approach for Synthesizing Biocompatible Gold Nanoparticles, *Nanoscale Res. Lett.,* 2014, 9, 248, doi: 10.1186/1556-276X-9-248.

[103] Meshram, S. M.; Bonde, S. R.; Gupta, I. R.; Gade, A. K.; Rai, M. K. Green Synthesis of Silver Nanoparticles Using White Sugar, *IET Nanobiotechnol*., 2013, 7, 28, doi: 10.1049/iet-nbt.2012.0002.

[104] Tu, N. T. T.; Vo, T. L.; Ho, T. T.; Dang, K. T.; Le, V. D.; Minh, P. N.; Dang, C. H.; Tran, V. T.; Dang, V. S.; Chi, T. T. K.; Vu-Quang, H.; Fajgar, R.; Nguyen, T. L.; Doan, V. D.; Nguyen, T. D. Silver Nanoparticles Loaded on Lactose/Alginate: In Situ Synthesis, Catalytic Degradation, and pH-Dependent Antibacterial Activity, *Beilstein J. Nanotechnol*., 2023, 14, 781, doi: 10.3762/bjnano.14.64.

[105] Sharma, Diksha & Rakshana, D & Balakrishnan, Raj Mohan & PonnanEttiyappan, JagadeeshBabu, One Step Synthesis of Silver Nanowires Using Fructose as a Reducing Agent and its Antibacterial and Antioxidant Analysis. *Mat. Res. Exp*. 2019, 6, 075050, doi:10.1088/2053-1591/ab170a.

[106] Saxena, A.; Tripathy, R. M.; Singh, R. P. Biological Synthesis of Silver Nanoparticles by Using onion (*Allium cepa*) Extract and Their Antibacterial Activity, *Dig. J. Nanomater. Biostruct.,* 2010, **5**, 427, doi: 10.5829/idosi.wasj.2015.33.06.9525.

[107] Eteraf-Oskouei, T.; Najafi, M. Traditional and Modern Uses of Natural Honey in Human Diseases: A Review, *Iran J. Basic. Med. Sci*., 2013, 16, 731, PMCID: PMC3758027.

[108] Kiran, G.; Singh, R. P.; Ashutosh, P. et al., Photocatalytic Antibacterial Performance of TiO_2 and Ag-Doped TiO_2 Against *S. aureus*. *P. aeruginosa* and *E. coli*, *Beilstein J. Nanotechnol.*, 2013, 4, 345, doi: 10.3762/bjnano.4.40.

[109] Saraschandraa, N.; Pavithrab, M.; Sivakumar, A. Antimicrobial Applications of TiO_2 Coated Modified Polyethylene (HDPE) Films, *Arch. Appl. Sci. Res.*, 2013, 5, 189.

[110] Chen, X.; Mao, S. S. Titanium Dioxide Nanomaterials: Synthesis, Properties, Modifications and Applications, *Chem. Rev.*, 2007, 107, 2891, doi: 10.1021/cr0500535.

[111] Nadtochenko, V.; Denisov, N.; Sarkisov, O. et al. Laser Kinetic Spectroscopy of the Interfacial Charge Transfer Between Membrane Cell Walls of *E. coli* and TiO_2 , *J. Photochem. Photobiol. A: Chem.*, 2006, 181, 401, doi: 10.1016/j.jphotochem.2005.12.028.

[112] Shah, M. S. A.; Nag, M.; Kalagara, T. et al. Silver on PEG-PU-TiO_2 Polymer Nanocomposite Films; An Excellent System for Antibacterial Applications, *Chem. Materials*, 2008, 20, 2455, doi: 10.1021/cm7033867.

[113] Fujishima, A.; Rao, T. N.; Tryk, D. A. Titanium Dioxide Photocatalysis, *J. Photochem. Photobiol. C: Photochem. Rev.*, 2000, 1, 1, doi: 10.1016/S1389-5567(00)00002-2.

[114]Shiraishi, Y.; Hirai, T. Selective Organic Transformations on Titanium Oxide-Based Photocatalysts, *J. Photochem. Photobiol. C: Photochem. Rev.*, 2008, 9, 157, doi: 10.1016/j.jphotochemrev.2008.05.001.

[115] Cho, K.; Park, J.; Osaka, T.; *et al*. The Study of Antimicrobial Activity and Preservative Effects of Nanosilver Ingredient, *Electrochim. Acta*, 2005, 51, 956, doi: 10.1016/j.electacta.2005.04.071.

[116] Dedman, C. J.; King, A. M.; Christie-Oleza J. A.; Davies, G.-L. Environmentally Relevant Concentrations of Titanium Dioxide Nanoparticles Pose Negligible Risk to Marine Microbes, *Environ. Sci.: Nano*, 2021, 8, 1236, doi: 10.1039/D0EN00883D.

[117] Chang, H.; Wang, Q.; Meng, X.; Chen, X.; Deng, Y.; Li, L.; Yang, Y.; Song G.; Jia, H. Effects of Nano-Titanium Dioxide on Calcium Homeostasis *In Vivo* and *In Vitro*: A Systematic Review and Meta-Analysis, *Chem. Res. Toxicol*., 2022, 35, 1435, doi: 10.1080/15376516.2022.2124137.

[118] Sargazi, S.; ER, S.; Sacide Gelen, S.; Rahdar, A.; Bilal, M.; Arshad, R.; Ajalli, N.; Farhan Ali Khan M.; Pandey, S. A Comprehensive Review of Inorganic Sonosensitizers for Sonodynamic Therapy, *J. Drug Delivery Sci. Technol*., 2022, 75, 103605, doi: 10.3390/ijms241512001.

[119] Rodrı´guez-Barajas, N.; Anaya-Esparza, M. L.; Villagra´n-de la Mora, Z.; Sa´nchez-Burgos A. J.; Pe´rez-Larios, A. Anticancer Agents Derived from Cyclic Thiosulfonates: Structure-Reactivity and Structure-Activity Relationships, *Adv. Anticancer Agents Med. Chem.*, 2022, 22, 2241, doi: 10.1002/cmdc.202200165.

[120] Javed, R.; Ul Ain, N.; Gul, A.; Arslan Ahmad, M.; Guo, W.; Ao Q.; Tian, S. Diverse Biotechnological Applications of Multifunctional Titanium Dioxide Nanoparticles: An Up-to-Date Review, *IET Nanobiotechnol*., 2022, 16, 171, doi: 10.1049/nbt2.12085.

[121] Valeriani, F.; Margarucci, L. M.; Romano Spica, V. Recreational Use of Spa Thermal Waters: Criticisms and Perspectives for Innovative Treatments, *Int. J. Environ. Res. Public Health*, 2018, 15, 2675, doi: 10.3390/ijerph15122675.

[122] Margarucci, L. M.; Romano Spica, V.; Gianfranceschi G.; Valeriani, F. Untouchability of Natural Spa Waters: Perspectives for Treatments Within a Personalized Water Safety Plan, *Environ. Int*., 2019, 133, 105095, doi: 10.1016/j.envint.2019.105095.

[123] Bertel, L.; Miranda, D.A.; García-Martín, J.M. Nanostructured Titanium Dioxide Surfaces for Electrochemical Biosensing, *Sensors*, 2021, 21, 6167, doi: 10.3390/s21186167.

[124] Karbowniczek, J. E.; Ura D. P.; Stachewicz, U. Nanoparticles Distribution and Agglomeration Analysis in Electrospun Fiber Based Composites for Desired Mechanical Performance of Poly(3-hydroxybuty-rate-co-3-Hydroxyvalerate (PHBV) Scaffolds with Hydroxyapatite (HA) and Titanium Dioxide (TiO_2) Towards Medical Applications, *Composites, Part B*, 2022, 241, 110011, doi: 10.1016/j.compositesb.2022.110011.

[125] Chang, H.; Wang, Q.; Meng, X.; Chen, X.; Deng, Y.; Li, L.; Yang, Y.; Song G.; Jia, H. *Chem. Res. Toxicol*., 2022, 35, 1435, doi: 10.1021/acs.chemrestox.1c00402.

[126] Ziental, D.; Czarczynska-Goslinska, B.; Mlynarczyk, D.; Glowacka-Sobotta, A.; Stanisz, B.; Goslinski, T.; Sobotta, L. Titanium Dioxide Nanoparticles: Prospects and Applications in Medicine, *Nanomat*. 2020, 10. 387, doi: 10.3390/nano10020387.

[127] Youssef, Z.; Vanderesse, R.; Colombeau, L.; Baros, F.; Roques-Carmes, T.; Frochot, C.; Wahab, H.; Toufaily, J.; Hamieh, T.; Acherar, S.; et al., The Application of Titanium Dioxide, Zinc Oxide, Fullerene, and Graphene Nanoparticles in Photodynamic Therapy, *Cancer Nanotechnol.*, 2017, 8, 6, doi: 10.1186/s12645-017-0032-2.

[128] Xu, J.; Sun, Y.; Huang, J.; Chen, C.; Liu, G.; Jiang, Y.; Zhao, Y.; Jiang, Z. Photokilling Cancer Cells Using Highly Cell-Specific Antibody-TiO_2 Bioconjugates and Electroporation, *Bioelectrochemistry*, 2007, 71, 217, doi: 10.1016/j.bioelechem.2007.06.001.

[129] Feng, X.; Zhang, S.; Wu, H.; Lou, X. A Novel Folic Acid-Conjugated TiO_2-SiO_2 Photosensitizer for Cancer Targeting in Photodynamic Therapy, *Colloids Surf. B Biointerfaces*, 2015, 125, 197, doi: 10.1016/j.colsurfb.2014.11.035.

[130] Guiot, C.; Spalla, O. Stabilization of TiO_2 Nanoparticles in Complex Medium through a pH Adjustment Protocol, *Environ. Sci. Technol.*, 2013, 47, 1057, doi: 10.1021/es3040736.

[131] Xu, F. Review of Analytical Studies on TiO_2 Nanoparticles and Particle Aggregation, Coagulation, Flocculation, Sedimentation, Stabilization, *Chemosphere.*, 2018, 212, 662, doi: 10.1016/j.chemosphere.2018.08.108.

[132] Gupta, V.K.; Gupta, B.; Rastogic, A.; Agarwald, S.; Nayaka, A. A Comparative Investigation on Adsorption Performances of Mesoporous Activated Carbon Prepared From Waste Rubber Tire and Activated Carbon for a Hazardous Azo Dye–Acid Blue, *J. Hazard. Mater*., 2011, 113, 186, 891, https://doi.org/10.1016/j.jhazmat.2010.11.091.

[133] Byrne, J.A.; Eggins, B.R.; Brown, N.M.D.; McKinney, B.; Rouse, M. Immobilisation of TiO_2 Powder for the Treatment of Polluted Water, *App. Catal. B Environ*. 1998, 17, 25, https://doi.org/10.1016/S0926-3373(97)00101-X.

[134] De Oliveira, R. C.; de Foggi, C. C.; Teixeira, M. M.; Da Silva, M. D. P.; Assis, M.; Francisco, E. M. et al., Mechanism of Antibacterial Activity Via Morphology Change of α-$AgVO_3$: Theoretical and Experimental Insights, *ACS Appl. Mater, Interfaces*, 2017, 9, 11472, doi: 10.1021/acsami.7b00920.

[135] Gilbertson, L. M.; Albalghiti, E. M.; Fishman, Z. S.; Perreault, F.; Corredor, C.; Posner, J. D.; et al., Shape-Dependent Surface Reactivity and Antimicrobial Activity of Nano-Cupric Oxide, *Environ. Sci. Technol.*, 2016, 50, 3975, doi: 10.1021/acs.est.5b05734.

[136] He, Z.; Cai, Q.; Fang, H.; Situ, G.; Qiu, J.; Song, S.; et al. Photocatalytic Activity of TiO_2 Containing Anatase Nanoparticles and Rutile Nanoflower Structure Consisting of Nanorods, *J. Environm. Sci*. 2013, 25, 2460, doi: 10.1016/S1001-0742(12)60318-0.

[137] Sarkar, D.; Ghosh, C. K.; Chattopadhyay, K. K. Morphology Control of Rutile TiO_2 Hierarchical Architectures and Their Excellent Field Emission Properties, *Cryst. Eng. Comm*., 2012, 14, 2683, doi: 10.1039/c2ce06392a.

[138] Burda, C.; Chen, X.; Narayanan, R.; El-Sayed, M. A. Chemistry and Properties of Nanocrystals of Different Shapes, *Chem. Rev*., 2005, 105, 1025, doi: 10.1021/cr030063a.

[139] Ma, W.; Li, J.; Liu, Y.; Ren, X.; Gu, Z. G.; Xie, Z.; et al. Preparation and Characterization of Excellent Antibacterial TiO_2/N-Halamines Nanoparticles. *Colloids Surf. A: Physicochem. Eng*., 2016, 506, 284, doi: 10.1016/j.colsurfa.2016.06.055.

[140] López de Dicastillo, C.; Guerrero Correa, M. B.; Martínez, F.; Streitt, C.; José Galotto, M. Antimicrobial Effect of Titanium Dioxide Nanoparticles, *Intech Open*., 2021, doi: 10.5772/intechopen.90891.

[141] Chen, W. J.; Tsai, P. J.; Chen, Y. C. Functional Fe_3O_4/TiO_2 Core/Shell Magnetic Nanoparticles as Photokilling Agents for Pathogenic Bacteria, *Small*, 2008, 4, 485, doi: 10.1002/smll.200701164.

[142] Liu, Z; Zhang, M.; Han, X.; Xu, H.; Zhang, B.; Yu, Q.; et al. TiO_2 Nanoparticles Cause Cell Damage Independent of Apoptosis and Autophagy by Impairing the ROS-Scavenging System in *Pichia pastoris*. *Chemico-Biological Interactions*, 2016, 252, 9, doi: 10.1016/j.cbi.2016.03.029.

[143] Podporska-Carroll, J.; Panaitescu, E.; Quilty, B.; Wang, L.; Menon, L.; Pillai, S. C. Antimicrobial Properties of Highly Efficient Photocatalytic TiO_2 Nanotubes, *Appl. Catal*., 2015, 176-177, 70, doi: 10.1016/j.apcatb.2015.03.029.

[144] Yuan, Y.; Ding, J.; Xu, J.; Deng, J.; Guo, J. TiO_2 Nanoparticles Co-Doped with Silver and Nitrogen for Antibacterial Application, *J. Nanosci. Nanotechnol*., 2010, 10, 4868, doi: 10.1166/jnn.2010.2225.

[145] Wu, B.; Huang, R.; Sahu, M.; Feng, X.; Biswas, P.; Tang, Y. J. Bacterial Responses to Cu-doped TiO_2 Nanoparticles. *Sci. Total Environ*., 2010, 408, 1755, doi: 10.1016/j.scitotenv.2009.11.004.

[146] Tsuang, Y. H.; Sun, J. S.; Huang, Y. C.; Lu, C. H.; Chang, W. H. S.; Wang, C. C. Studies of Photokilling of Bacteria Using Titanium Dioxide Nanoparticles, *Artificial Organs*., 2008, 32, 167, doi: 10.1111/j.1525-1594.2007.00530.x.

[147] Verdier, T.; Coutand, M.; Bertron, A.; Roques, C. Antibacterial Activity of TiO_2 Photocatalyst Alone or in Coatings on *E. coli*: The Influence of Methodological Aspects, *Coatings*, 2014, 4, 670, doi: 10.3390/coatings4030670.

[148] Kaladhar Reddy, A.; Kambalyal, P. B.; Shanmugasundaram, K.; Rajesh, V.; Donthula, S.; Patil, S. R. Comparative Evaluation of Antimicrobial Efficacy of Silver, Titanium Dioxide and Zinc Oxide Nanoparticles Against *Streptococcus* mutans. *Pesquisa Brasileira Em Odontopediatria e Clinica Integrada*, 2018, 18, 1, doi: 10.4034/PBOCI.2018.181.88.

[149] Kiwi, J.; Rtimi, S. Mechanisms of the Antibacterial Effects of TiO_2-FeO_x Under Solar or Visible Light: Schottky Barriers Versus Surface Plasmon Resonance, *Coatings*, 2018, 8, 391, doi: 10.3390/coatings8110391.

[150] Hao, R.; Xing, R.; Xu, Z.; Hou, Y.; Gao, S.; Sun, S. Synthesis, Functionalization, and Biomedical Applications of Multifunctional Magnetic Nanoparticles, *Adv. Mater.*, 2010, 22, 2729, doi:10.1002/adma.201000260.

[151] Wu, L.; Mendoza-Garcia, A.; Li, Q.; Sun, S. Organic Phase Syntheses of Magnetic Nanoparticles and Their Applications, *Chem. Rev.*, 2016, 116, 10473, doi:10.1021/acs.chemrev.5b00687.

[152] Thorat, N. D.; Bohara, R. A.; Noor, M. R.; Dhamecha, D.; Soulimane, T.; Tofail, S. A. M. Effective Cancer Theranostics with Polymer Encapsulated Superparamagnetic Nanoparticles: Combined Effects of Magnetic Hyperthermia and Controlled Drug Release, *ACS Biomater. Sci. Eng.*, 2017, 3, 1332, doi:10.1021/acsbiomaterials.6b00420.

[153] Zhu, K.; Ju, Y.; Xu, J.; Yang, Z.; Gao, S.; Hou, Y. Magnetic Nanomaterials: Chemical Design, Synthesis, and Potential Applications, *Acc. Chem. Res.*, 2018, 51, 404, doi:10.1021/acs.accounts.7b00407.

[154] Zhang, Q.; Yang, X.; Guan, J. Applications of Magnetic Nanomaterials in Heterogeneous Catalysis. *ACS Appl. Nano Mater.* 2019, 2, 4681, doi:10.1021/acsanm.9b00976.

[155] Kefeni, K. K.; Msagati, T. A. M.; Mamba, B. B. Ferrite Nanoparticles: Synthesis, Characterisation and Applications in Electronic Device, *Mater. Sci. Eng. B*, 2017, 215, 37, doi:10.1016/j.mseb.2016.11.002.

[156] Babes, L.; Denizot, B.; Tanguy, G.; Le Jeune, J. J.; Jallet, P. Synthesis of Iron Oxide Nanoparticles Used as MRI Contrast Agents: a Parametric Study. *J. Colloid Interf. Sci.* 1999, 212, 474, doi:10.1006/jcis.1998.6053.

[157] Ali, A.; Shah, T.; Ullah, R.; Zhou, P.; Guo, M.; Ovais, M.; Tan, Z.; Rui, Y. Review on Recent Progress in Magnetic Nanoparticles: Synthesis, Characterization, and Diverse Applications, *Front Chem*., 2021, 9, 629054, doi: 10.3389/fchem.2021.629054.

[158] Sandeep Kumar, V. Magnetic Nanoparticles-Based Biomedical and Bioanalytical Applications, *J. Nanomed. Nanotechol.*, 2013, 4, e130, doi:10.4172/2157-7439.1000e130.

[159] Indira, T.; Lakshmi, P. Magnetic Nanoparticles–A Review, *Int. J. Pharm. Sci. Nanotechnology*, 2013, 1035, https://doi.org/10.37285/ijpsn.2010.3.3.1.

[160] Mosayebi, J.; Kiyasatfar, M.; Laurent, S. Synthesis, Functionalization, and Design of Magnetic Nanoparticles for Theranostic Applications, *Adv. Healthc. Mater.*, 2017, 6, 1700306, doi:10.1002/adhm.201700306.

[161] Roy, K.; Roy, I. Therapeutic Applications of Magnetic Nanoparticles: Recent Advances, *Mater. Adv.*, 2022, 3, 7425, doi: 10.1039/D2MA00444E.

[162] Kimberly M. C.; Yunfeng, L.; Tonghua, Z.; Jingjing, Z.; Gary, M. P.; Vijay, J. Water Decontamination Using Iron and Iron Oxide Nanoparticles, *Nanotechnology Applications for Clean Water*, 2009, 347, doi:10.1016/B978-0-8155-1578-4.50033-0.

[163] Tang, S. C.N.; Lo, I. M. C. Magnetic Nanoparticles: Essential Factors for Sustainable Environmental Applications, *Water Res.*, 2013, 47, 2613, doi: 10.1016/j.watres.2013.02.039.

[164]Aryal, R.; Vigneswaran, S.; Kandasamy, J.; Naidu, R. Urban Stormwater Quality and Treatment, *Korean J. Chem. Eng*., 2010, 27, 1343, https://doi.org/10.1007/s11814-010-0387-0.

[165] McCoy, T. M.; Brown, P.; Eastoe, J.; Tabor, R. F. Noncovalent Magnetic Control and Reversible Recovery of Graphene Oxide Using Iron Oxide and Magnetic Surfactants, *App. Mater. Interfaces*, 2014, 7, 2124, https://doi.org/10.1021/am508565d.

[166] Anza-vhudziki, M.; Kamika, I.; Maggy, N. Nanoscale Development and its Application in Multidisciplinary Area: An African Perspective, *Afr. J. Biotechnol*., 2017, 16, 193, doi: 10.5897/AJB2016.15254.

[167] Maity, D.; Agrawal, D.C. Synthesis of Iron Oxide Nanoparticles Under Oxidizing Environment and Their Stabilization in Aqueous and Non-aqueous Media, *J. Magn. Magn. Mater.*, 2007, 308, 46, doi: 10.1016/j.jmmm.2006.05.001.

[168] Zhang, L.; He, R.; Gu, H.C. Oleic Acid Coating on the Monodisperse Magnetite Nanoparticles, *Appl. Surf. Sci*., 2006, 253, 2611, doi: 10.1016/j.apsusc.2006.05.023.

[169] Zhou, Y.T.; Nie, H.L.; Branford-White, C.; He, Z.Y.; Zhu, L.M. Removal of Cu^{2+} from Aqueous Solution by Chitosan-Coated Magnetic Nanoparticles Modified with α-Ketoglutaric Acid, *J. Colloid Interface Sci.*, 2009, 330, 29, doi: 10.1016/j.jcis.2008.10.026.

[170] Yantasee, W., Warner, C.L.; Sangvanich, T.; Addleman, R.S.; Carter, T.G.; Wiacek, R.J.; Fryxell, G.E.; Timchalk, C.; Warner, M.G. Removal of Heavy Metals from Aqueous Systems with Thiol Functionalized Superparamagnetic Nanoparticles, *Environ. Sci. Technol.*, 2007, 41, 5114, doi: 10.1021/es0705238.

[171] Chronopoulou, L.; Di Nitto, A.; Papi, M.; Parolini, O.; Falconi, M.; Teti, G.; Muttini, A.; Lattanzi, W.; Palmieri, V.; Ciasca, G. Biosynthesis and Physico-Chemical Characterization of High Performing Peptide Hydrogels@Graphene Oxide Composites, *Colloids Surf. B Biointerfaces*, 2021, 207, 111989, doi: 10.1016/j.colsurfb.2021.111989.

[172] Chronopoulou, L.; Daniele, M.; Perez, V.; Gentili, A.; Gasperi, T.; Lupi, S.; Palocci, C. A Physico-Chemical Approach to the Study of Genipin Crosslinking of Biofabricated Peptide Hydrogels, *Process Biochem*., 2018, 70, 110, doi: 10.1016/j.procbio.2018.04.005.

[173] Bonsignore, G.; Patrone, M.; Martinotti, S.; Ranzato, E. "Green" Biomaterials: The Promising Role of Honey, *J. Funct. Biomater*., 2021, 12, 72, doi: 10.3390/jfb12040072.

[174] Seferji, K.A.; Susapto, H.H.; Khan, B.K.; Rehman, Z.U.; Abbas, M.; Emwas, A.-H.; Hauser, C.A.E. Green Synthesis of Silver-Peptide Nanoparticles Generated by the Photoionization Process for Anti-Biofilm Application, *ACS Appl. Bio Mater*., 2021, 4, 8522, doi: 10.1021/acsabm.1c01013.

[175] Briggs, D.; Seah, M.P. Practical surface analysis, auger and X-ray Photoelectron Spectroscopy, *In Practical Surface Analysis*, 1990, https://doi.org/10.1002/jctb.280530219.

[176] Prieto, P.; Nistor, V.; Nouneh, K.; Oyama, M.; Abd-Lefdil, M.; Díaz, R. XPS Study of Silver, Nickel and Bimetallic Silver–Nickel Nanoparticles Prepared by Seed-Mediated Growth, *Appl. Surf. Sci*., 2012, 258, 8807, doi:10.1016/J.APSUSC.2012.05.095.

[177] Chronopoulou, L.; Di Nitto, A.; Papi, M.; Parolini, O.; Falconi, M.; Teti, G.; Muttini, A.; Lattanzi, W.; Palmieri, V.; Ciasca, G. Biosynthesis and Physico-Chemical Characterization of High Performing Peptide Hydrogels@Graphene Oxide Composites, *Colloids Surf. B Biointerfaces*, 2021, 207, 111989, doi: 10.1016/j.colsurfb.2021.111989.

[178] Yadollahi, M.; Farhoudian, S.; Namazi, H. One-pot Synthesis of Antibacterial Chitosan/Silver Bio-Nanocomposite Hydrogel Beads as Drug Delivery Systems, *Int. J. Biol. Macromol.*, 2015, 79, 37, doi: 10.1016/j.ijbiomac.2015.04.032.

[179] Kurhade, S.T.; Momin, M.; Khanekar, P.; Mhatre, S. Novel Biocompatible Honey Hydrogel Wound Healing Sponge for Chronic Ulcers, *Int. J. Drug Deliv.*, 2014, 5, 353, doi: 10.12968/jowc.2016.25.6.364.

[180] Elyamny, S.; Eltarahony, M.; Abu-Serie, M.; Nabil, M.M.; Kashyout, A.E.-H.B. One-Pot Fabrication of Ag @Ag_2O Core–Shell Nanostructures for Biosafe Antimicrobial and Antibiofilm Applications, *Sci. Rep*., 2021, 11, 22543, doi: 10.1038/s41598-021-01687-4.

[181] Di Domenico, E.G.; Oliva, A.; Guembe, M. The Current Knowledge on the Pathogenesis of Tissue and Medical Device-Related Biofilm Infections, *Microorganisms*, 2022, 10, 1259, doi: 10.3390/microorganisms10071259.

[182] Karthikeyan, C.; Jayaramudu, T.; Núñez, D.; Jara, N.; Opazo-Capurro, A.; Varaprasad, K.; Kim, K.; Yallapu, M.M.; Sadiku, R. Hybrid Nanomaterial Composed of Chitosan, Curcumin, ZnO and TiO_2 for Antibacterial Therapies, *Int. J. Biol. Macromol*., 2023, 242, 124814, doi: 10.1016/j.ijbiomac.2023.124814.

[183] Xu, Y.; Wei, M.-T.; Ou-Yang, H.D.; Walker, S.G.; Wang, H.Z.; Gordon, C.R.; Guterman, S.; Zawacki, E.; Applebaum, E.; Brink, P.R. Exposure to TiO_2 Nanoparticles Increases Staphylococcus aureus Infection of HeLa Cells, *J. Nanobiotechnol*., 2016, 14, 34, doi: 10.1186/s12951-016-0184-y.

[184] Azizi-Lalabadi, M.; Ehsani, A.; Divband, B.; Alizadeh-Sani, M. Antimicrobial Activity of Titanium Dioxide and Zinc Oxide Nanoparticles Supported in 4A Zeolite and Evaluation the Morphological Characteristic, *Sci. Rep*., 2019, 9, 17439. doi: 10.1038/s41598-019-54025-0.

[185] Shang, C.; Bu, J.; Song, C. Preparation, Antimicrobial Properties under Different Light Sources, Mechanisms and Applications of TiO_2 : A Review, *Materials*, 2022, 15, 5820, doi:10.3390/ma15175820.

[186] Yang, F.; Liu, S.-L.; Xu, Y.; Walker, S.G.; Cho, W.; Mironava, T.; Rafailovich, M. The Impact of TiO_2 Nanoparticle Exposure on Transmembrane Cholesterol Transport and Enhanced Bacterial Infectivity in HeLa Cells, *Acta Biomater*., 2021, 135, 606, doi: 10.1016/j.actbio.2021.08.012.

[187] Ahn, T.; Kim, J. H.; Yang, H.-M.; Lee, J. W.; Kim, J.-D. Formation Pathways of Magnetite Nanoparticles by Coprecipitation Method. *J. Phys. Chem. C*, 2012, 116, 6069, doi: 10.1021/jp211843g.

[188] Patnaik, P. Handbook of Inorganic Chemicals; McGraw-Hill: New York, NY, USA, 2003; Volume 529.

[189] Patnaik, P. Handbook of Inorganic Chemicals; McGraw-Hill: New York, NY, USA, 2003; Volume 529.

[190] Cerra, S.; Carlini, L.; Salamone, T. A.; Hajareh Haghighi, F.; Mercurio, M.; Pennacchi, B.; Sappino, C.; Battocchio, C.; Nottola, S.; Matassa, R.; Fratoddi, I. Noble Metal Nanoparticles Networks Stabilized by Rod-Like Organometallic Bifunctional Thiols. *ChemistrySelect*, 2023, 8, e202300874, doi:10.1002/slct.202300874.

[191] Gutiérrez, L.; de la Cueva, L.; Moros, M.; Mazarío, E.; de Bernardo, S.; de la Fuente, J. M.; Morales, M. P.; Salas, G. Aggregation Effects on the Magnetic Properties of Iron Oxide Colloids. *Nanotechnology*, 2019, 30, 112001, doi. 10.1088/1361-6528/aafbff.

[192] Harris, L. A.; Goff, J. D.; Carmichael, A. Y.; Riffle, J. S.; Harburn, J. J.; St. Pierre, T. G.; Saunders, M. Magnetite Nanoparticle Dispersions Stabilized with Triblock Copolymers. *Chem. Mater.*, 2003, 15, 1367, doi: 10.1021/cm020994n.

[193] Pardoe, H.; Chua-Anusorn, W.; Pierre, T. G. S.; Dobson, J. Structural and Magnetic Properties of Nanoscale Iron Oxide Particles Synthesized in the Presence of Dextran or Polyvinyl Alcohol. *J. Magn. Magn. Mater*., 2001, 225, 41, doi: 10.1016/S0304-8853(00)01226-9.

[194] Di Corato, R.; Espinosa, A.; Lartigue, L.; Tharaud, M.; Chat, S.; Pellegrino, T.; Ménager, C.; Gazeau, F.; Wilhelm, C. Magnetic Hyperthermia Efficiency in the Cellular Environment for Different Nanoparticle Designs. *Biomaterials*, 2014, 35, 6400, doi: 10.1016/j.biomaterials.2014.04.036.

[195] Nahar, Y.; Rahman, M. A.; Hossain, M. K.; Sharafat, M. K.; Karim, M. R.; Elaissari, A.; Ochiai, B.; Ahmad, H.; Rahman, M. M. A Facile One-Pot Synthesis of Poly(Acrylic Acid)-Functionalized Magnetic Iron Oxide Nanoparticles for Suppressing Reactive Oxygen Species Generation and Adsorption of Biocatalyst. *Mater. Res. Express*, 2020, 7, 16102, doi: 10.1088/2053-1591/ab5be1.

[196] Rutnakornpituk, M.; Puangsin, N.; Theamdee, P.; Rutnakornpituk, B.; Wichai, U. Poly (Acrylic Acid)-Grafted Magnetic Nanoparticle for Conjugation with Folic Acid. *Polymer*, 2011, 52, 987, doi: 10.1016/j.polymer.2010.12.059.

[197] Jain, N.; Wang, Y.; Jones, S. K.; Hawkett, B. S.; Warr, G. G. Optimized Steric Stabilization of Aqueous Ferrofluids and Magnetic Nanoparticles. *Langmuir*, 2010, 26, 4465, doi: 10.1021/la903513v.

[198] Lin, C.-L.; Lee, C.-F.; Chiu, W.-Y. Preparation and Properties of Poly(Acrylic Acid) Oligomer Stabilized Superparamagnetic Ferrofluid. *J. Colloid Interface Sci.*, 2005, 291, 411, doi: 10.1016/j.jcis.2005.05.023.

[199] Chronopoulou, L.; Lorenzoni, S.; Masci, G.; Dentini, M.; Togna, A. R.; Togna, G.; Bordi, F.; Palocci, C. Lipase-Supported Synthesis of Peptidic Hydrogels. *Soft Matter*, 2010, 6, 2525, doi: 10.1039/C001658F.

[200] Jubb, A. M.; Allen, H. C. Vibrational Spectroscopic Characterization of Hematite, Maghemite, and Magnetite Thin Films Produced by Vapor Deposition. *ACS Appl. Mater. Interfaces*, 2010, 2, 2804, doi: 10.1021/am1004943.

[201] Yadav, B. Sen; Singh, R.; Vishwakarma, A. K.; Kumar, N. Facile Synthesis of Substantially Magnetic Hollow Nanospheres of Maghemite (γ-Fe_2O_3) Originated from Magnetite (Fe_3O_4) via Solvothermal Method. *J. Supercond. Nov. Magn.* 2020, 33, 2199, doi: 10.1007/s10948-020-05481-7.

[202] Chamritski, I.; Burns, G. Infrared-and Raman-Active Phonons of Magnetite, Maghemite, and Hematite: A Computer Simulation and Spectroscopic Study. *J. Phys. Chem. B*, 2005, 109, 4965, doi: 10.1021/jp048748h.

[203] Kirwan, L. J.; Fawell, P. D.; van Bronswijk, W. In Situ FTIR-ATR Examination of Poly(Acrylic Acid) Adsorbed onto Hematite at Low PH. *Langmuir*, 2003, 19, 5802, doi: 10.1021/la027012d.

[204] Testa-Anta, M.; Ramos-Docampo, M. A.; Comesaña-Hermo, M.; Rivas-Murias, B.; Salgueiriño, V. Raman Spectroscopy to Unravel the Magnetic Properties of Iron Oxide Nanocrystals for Bio-Related Applications. *Nanoscale Adv.*, 2019, 1, 2086, doi: 10.1039/C9NA00064J.

[205] De Faria, D. L. A.; Venâncio Silva, S.; De Oliveira, M. T. Raman Microspectroscopy of Some Iron Oxides and Oxyhydroxides. *J. Raman Spectrosc*., 1997, 28, 873, doi: 10.1002/(SICI)1097-4555.

[206] Murli, C.; Song, Y. Pressure-Induced Polymerization of Acrylic Acid: A Raman Spectroscopic Study. *J. Phys. Chem. B*, 2010, 114, 9744, doi: 10.1021/jp1034757.

[207] de Faria, D. L. A.; Lopes, F. N. Heated Goethite and Natural Hematite: Can Raman Spectroscopy Be Used to Differentiate Them? *Vib. Spectrosc*., 2007, 45, 117, doi: 10.1016/j.vibspec.2007.07.003.

[208] Guo, C.; Hu, Y.; Qian, H.; Ning, J.; Xu, S. Magnetite (Fe_3O_4) Tetrakaidecahedral Microcrystals: Synthesis, Characterization, and Micro-Raman Study. *Mater. Charact*., 2011, 62, 148, doi: 10.1016/j.matchar.2010.10.016.

[209] Shebanova, O. N.; Lazor, P. Raman Study of Magnetite (Fe_3O_4): Laser-induced Thermal Effects and Oxidation. *J. Raman Spectrosc.*, 2003, 34, 845, doi: 10.1002/jrs.1056.

[210] Slavov, L.; Abrashev, M. V; Merodiiska, T.; Gelev, C.; Vandenberghe, R. E.; Markova-Deneva, I.; Nedkov, I. Raman Spectroscopy Investigation of Magnetite Nanoparticles in Ferrofluids. *J. Magn. Magn. Mater*., 2010, 322, 1904, doi: 10.1016/j.jmmm.2010.01.005.

[211] Grosvenor, A. P.; Kobe, B. A.; Biesinger, M. C.; McIntyre, N. S. Investigation of Multiplet Splitting of Fe2p XPS Spectra and Bonding in Iron Compounds. *Surf. Interface Anal*., 2004, 36, 1564, doi: 10.1002/sia.1984.

[212] Biesinger, M. C.; Payne, B. P.; Grosvenor, A. P.; Lau, L. W. M.; Gerson, A. R.; Smart, R. S. C. Resolving Surface Chemical States in XPS Analysis of First Row Transition Metals, Oxides and Hydroxides: Cr, Mn, Fe, Co and Ni. *Appl. Surf. Sci*., 2011, 257, 2717, doi: 10.1016/j.apsusc.2010.10.051.

[213] Gupta, R. P.; Sen, S. K. Calculation of Multiplet Structure of Core *p*-Vacancy Levels. *Phys. Rev. B*, 1974, 10, 71, doi: 10.1103/PhysRevB.10.71.

[214] Gupta, R. P.; Sen, S. K. Calculation of Multiplet Structure of Core *p*-Vacancy Levels. II. *Phys. Rev. B*, 1975, 12, 15, doi: 10.1103/PhysRevB.12.15.

[215] Dong, J.; Ozaki, Y.; Nakashima, K. Infrared, Raman, and Near-Infrared Spectroscopic Evidence for the Coexistence of Various Hydrogen-Bond Forms in Poly(Acrylic Acid). *Macromolecules*, 1997, 30, 1111, doi: 10.1021/ma960693x.

[216] Sharif Sh., M.; Golestani Fard, F.; Khatibi, E.; Sarpoolaky, H. Dispersion and Stability of Carbon Black Nanoparticles, Studied by Ultraviolet–Visible Spectroscopy. *J. Taiwan Inst. Chem. Eng.*, 2009, 40, 524, doi: 10.1016/j.jtice.2009.03.006.

[217] Safaei, Y.; Aminzare, M.; Golestani-Fard, F.; Khorasanizadeh, F.; Salahi, E. Suspension Stability of Titania Nanoparticles Studied by UV-VIS Spectroscopy Method. *Iran. J. Mater. Sci. Eng*., 2012, 9, 62, ISSN 1735-0808.

[218] Salzmann, C. G.; Chu, B. T. T.; Tobias, G.; Llewellyn, S. A.; Green, M. L. H. Quantitative Assessment of Carbon Nanotube Dispersions by Raman Spectroscopy. Carbon, 2007, 45, 907, doi: 10.1016/j.carbon.2007.01.009.

[219] Horia, F.; Easawi, K.; Khalil, R.; Abdallah, S.; El-Mansy, M.; Negm, S. Optical and Thermophysical Characterization of Fe_3O_4 Nanoparticle. *IOP Conf. Ser. Mater. Sci. Eng.*, 2020, 956, 12016, doi: 10.1088/1757-899X/956/1/012016.

[220] Jung, H.; Schimpf, A. M. Photochemical Reduction of Nanocrystalline Maghemite to Magnetite. *Nanoscale*, 2021, 13, 17465, doi: 10.1039/D1NR02973H.

[221] Sutherland, T. I.; Sparks, C. J.; Joseph, J. M.; Wang, Z.; Whitaker, G.; Sham, T. K.; Wren, J. C. Effect of Ferrous Ion Concentration on the Kinetics of Radiation-Induced Iron-Oxide Nanoparticle Formation and Growth. *Phys. Chem. Chem. Phys*., 2017, 19, 695, doi: 10.1039/C6CP05456K.

[222] Heinrich, C. A.; Seward, T. M. A Spectrophotometric Study of Aqueous Iron(II) Chloride Complexing from 25 to 200°C. *Geochim. Cosmochim. Acta*, 1990, 54, 2207, doi: 10.1016/0016-7037(90)90046-N.

[223] Zhao, R.; Pan, P. A Spectrophotometric Study of Fe(II)-Chloride Complexes in Aqueous Solutions from 10 to 100°C. *Can. J. Chem.*, 2001, 79, 131, doi: 10.1139/v01-001.

[224] Po, H. N.; Sutin, N. Stability Constant of the Monochloro Complex of Iron(II). *Inorg. Chem*., 1968, 7, 621, doi: 10.1021/ic50061a053.

[225] Kulshrestha, A.; Sharma, S.; Singh, K.; Kumar, A. Magnetoresponsive Biocomposite Hydrogels Comprising Gelatin and Valine Based Magnetic Ionic Liquid Surfactant as Controlled Release Nanocarrier for Drug Delivery. *Mater. Adv.*, 2022, 3, 484, doi: 10.1039/D1MA00758K.

[226] Gils, P. S.; Ray, D.; Sahoo, P. K. Designing of Silver Nanoparticles in Gum Arabic Based Semi-IPN Hydrogel. *Int. J. Biol. Macromol*., 2010, 46, 237, doi: 10.1016/j.ijbiomac.2009.12.014.

[227] Nagaraja, K.; Krishna Rao, K. S. V; Zo, S.; Soo Han, S.; Rao, K. M. Synthesis of Novel Tamarind Gum-Co-Poly(Acrylamidoglycolic Acid)-Based PH Responsive Semi-IPN Hydrogels and Their Ag Nanocomposites for

Controlled Release of Chemotherapeutics and Inactivation of Multi-Drug-Resistant Bacteria. *Gels*, 2021, 7, 237, doi: 10.3390/gels7040237.

[228] Jayaramudu, T.; Raghavendra, G. M.; Varaprasad, K.; Sadiku, R.; Ramam, K.; Raju, K. M. Iota-Carrageenan-Based Biodegradable Ag^0 Nanocomposite Hydrogels for the Inactivation of Bacteria. *Carbohydr. Polym*., 2013, 95, 188, doi: 10.1016/j.carbpol.2013.02.075.

[229] Veloso, S. R. S.; Martins, J. A.; Hilliou, L.; O. Amorim, C.; Amaral, V. S.; Almeida, B. G.; Jervis, P. J.; Moreira, R.; Pereira, D. M.; Coutinho, P. J. G.; Ferreira, P. M. T.; Castanheira, E. M. S. Dehydropeptide-Based Plasmonic Magnetogels: A Supramolecular Composite Nanosystem for Multimodal Cancer Therapy. *J. Mater. Chem. B*, 2020, 8, 45, doi: 10.1039/C9TB01900F.

[230] Carvalho, A.; Gallo, J.; Pereira, D. M.; Valentão, P.; Andrade, P. B.; Hilliou, L.; Ferreira, P. M. T.; Bañobre-López, M.; Martins, J. A. Magnetic Dehydrodipeptide-Based Self-Assembled Hydrogels for Theragnostic Applications. *Nanomaterials*, 2019, 9, 541, doi: 10.3390/nano9040541.

[231] Nagireddy, N. R.; Yallapu, M. M.; Kokkarachedu, V.; Sakey, R.; Kanikireddy, V.; Pattayil Alias, J.; Konduru, M. R. Preparation and Characterization of Magnetic Nanoparticles Embedded in Hydrogels for Protein Purification and Metal Extraction. *J. Polym. Res*., 2011, 18, 2285, doi: 10.1007/s10965-011-9642-2.

[232] Jørgensen, C. K.; De Verdier, C.-H.; Glomset, J.; Sörensen, N. A. Studies of Absorption Spectra. IV. Some New Transition Group Bands of Low Intensity. *Acta Chem. Scand*., 1954, 8, 1502, doi: 10.3891/acta.chem.scand.08-1502.

[233] Nonkumwong, J.; Ananta, S.; Srisombat, L. Effective Removal of Lead(II) from Wastewater by Amine-Functionalized Magnesium Ferrite Nanoparticles. *RSC Adv*., 2016, 6, 47382, doi: 10.1039/C6RA07680G.

[234] Li, Z.; Li, Y.; Chen, C.; Cheng, Y. Magnetic-Responsive Hydrogels: From Strategic Design to Biomedical Applications. *J. Control. Release*, 2021, 335, 541, doi:10.1016/j.jconrel.2021.06.003.

[235] Marey, A.; Ahmed, D. F. Batch Adsorption Studies of Natural Composite Hydrogel for Removal of Co(II) Ions. *J. Appl. Membr. Sci. Technol*., 2022, 26, 13, doi: 10.11113/amst.v26n3.244.

[236] Low, K. S.; Lee, C. K.; Liew, S. C. Sorption of Cadmium and Lead from Aqueous Solutions by Spent Grain. *Process Biochem*., 2000, 36, 59, doi: 10.1016/S0032-9592(00)00177-1.

[237] Ho, Y. S.; McKay, G. A Comparison of Chemisorption Kinetic Models Applied to Pollutant Removal on Various Sorbents. *Process Saf. Environ. Prot*., 1998, 76, 332, doi: 10.1205/095758298529696.

[238] Zhang, W.; Hu, L.; Hu, S.; Liu, Y. Optimized Synthesis of Novel Hydrogel for the Adsorption of Copper and Cobalt Ions in Wastewater. *RSC Adv*., 2019, 9, 16058, doi: 10.1039/C9RA00227H.

[239] Lawrance, G.A. Leaving Groups on Inert Metal Complexes with Inherent or Induced Lability. In Advances in Inorganic Chemistry; Academic Press: Cambridge, MA, USA, 1989; Volume 34, pp. 145, ISBN 0898-8838.

[240] Facchi, D. P.; Cazetta, A. L.; Canesin, E. A.; Almeida, V. C.; Bonafé, E. G.; Kipper, M. J.; Martins, A. F. New Magnetic Chitosan/Alginate/Fe_3O_4@SiO_2 Hydrogel Composites Applied for Removal of Pb(II) Ions from Aqueous Systems. *Chem. Eng. J.*, 2018, 337, 595, doi: 10.1016/j.cej.2017.12.142.

[241] Yao, G.; Bi, W.; Liu, H. PH-Responsive Magnetic Graphene Oxide/Poly(NVI-Co-AA) Hydrogel as an Easily Recyclable Adsorbent for Cationic and Anionic Dyes. *Colloids Surfaces A Physicochem. Eng. Asp*., 2020, 588, 124393, doi: 10.1016/j.colsurfa.2019.124393.

[242] van Berkum, S.; Biewenga, P. D.; Verkleij, S. P.; van Zon, J. (Hans) B. A.; Boere, K. W. M.; Pal, A.; Philipse, A. P.; Erné, B. H. Swelling Enhanced Remanent Magnetization of Hydrogels Cross-Linked with Magnetic Nanoparticles. *Langmuir*, 2015, 31, 442, doi: 10.1021/la503390w.

[243] Saadli, M.; Braunmiller, D. L.; Mourran, A.; Crassous, J. J. Thermally and Magnetically Programmable Hydrogel Microactuators. *Small*, 2023, 19, 2207035, doi: 10.1002/smll.202207035.

[244] Liu, W.; Migdisov, A.; Williams-Jones, A. The Stability of Aqueous Nickel(II) Chloride Complexes in Hydrothermal Solutions: Results of UV–Visible Spectroscopic Experiments. *Geochim. Cosmochim. Acta*, 2012, 94, 276, doi: 10.1016/j.gca.2012.04.055.

[245] Sáenz-Trevizo, A.; Pizá-Ruiz, P.; Chávez-Flores, D.; Ogaz-Parada, J.; Amézaga-Madrid, P.; Vega-Ríos, A.; Miki-Yoshida, M. On the Discoloration of Methylene Blue by Visible Light. *J. Fluoresc*., 2019, 29, 15, doi: 10.1007/s10895-018-2304-6.

[246] Purcar, V.; Donescu, D.; Petcu, C.; Vasilescu, M. Nanostructured Hybrid Systems with Rhodamine 6G. *J. Dispers. Sci. Technol*., 2008, 29, 1233, doi: 10.1080/01932690701856915.

[247] Ruiz, C.; Vera, M.; Rivas, B. L.; Sánchez, S. A.; Urbano, B. F. Magnetic Methacrylated Gelatin-g-Polyelectrolyte for Methylene Blue Sorption. *RSC Adv.*, 2020, 10, 43799, doi: 10.1039/d0ra08188d.

[248] Yao, G.; Bi, W.; Liu, H. pH-Responsive Magnetic Graphene Oxide/Poly(NVI-co-AA) Hydrogel as an Easily Recyclable Adsorbent for Cationic and Anionic Dyes. *Colloids Surf. A Physicochem. Eng. Asp.*, 2020, 588, 124393, doi: 10.1016/j.colsurfa.2019.124393.

[249] Gang, F.; Jiang, L.; Xiao, Y.; Zhang, J.; Sun, X. Multi-Functional Magnetic Hydrogel: Design Strategies and Applications. *Nano Select*, 2021, 2, 2291, doi: 10.1002/nano.202100139.

[250] Veloso, S. R. S.; Andrade, R. G. D.; Castanheira, E. M. S. Review on the Advancements of Magnetic Gels: Towards Multifunctional Magnetic Liposome-Hydrogel Composites for Biomedical Applications. *Adv. Coll. Inter. Sci*. 2021, 288, 102351, doi: 10.1016/j.cis.2020.102351.

[251] Van Berkum, S.; Biewenga, P. D.; Verkleij, S. P.; Van Zon, J. B. A.; Boere, K. W. M.; Pal, A.; Philipse, A. P.; Erné, B. H. Swelling Enhanced Remanent Magnetization of Hydrogels Cross-Linked with Magnetic Nanoparticles. *Langmuir*, 2014, 31, 442, doi: 10.1021/la503390w.

[252] Saadli, M.; Braunmiller, D.L.; Mourran, A.; Crassous, J.J. Thermally and Magnetically Programmable Hydrogel Microactuators. *Small*, 2023, 19, 2207035, doi: 10.1002/smll.202207035.

[253] Nagireddy, N.R.; Yallapu, M.M.; Kokkarachedu, V.; Sakey, R.; Kanikireddy, V.; Pattayil Alias, J.; Konduru, M.R. Preparation and Characterization of Magnetic Nanoparticles Embedded in Hydrogels for Protein Purification and Metal Extraction. *J. Polym. Res*., 2011, 18, 2285, doi: 10.1007/s10965-011-9642-2.

[254] Sharma, G.; García-Peñas, A.; Verma, Y.; Kumar, A.; Dhiman, P.; Stadler, F.J. Tailoring Homogeneous Hydrogel Nanospheres by Facile Ultra-Sonication Assisted Cross-Linked Copolymerization for Rhodamine B Dye Adsorption. *Gels*, 2023, 9, 770, doi: 10.3390/gels9100770.

[255] Rana, H.; Anamika, A.; Sareen, D.; Goswami, S. Nanocellulose-Based Ecofriendly Nanocomposite for Effective Wastewater Remediation: A Study on its Process Optimization, Improved Swelling, Adsorption, and Thermal and Mechanical Behavior. *ACS Omega*, 2024, 9, 8904, doi: 10.1021/acsomega.3c06924.

[256] Gao, H.; Jiang, J.; Huang, Y.; Wang, H.; Sun, J.; Jin, Z.; Wang, J.; Zhang, J. Synthesis of Hydrogels for Adsorption of Anionic and Cationic Dyes in Water: Ionic Liquid as a Crosslinking Agent. *SN Appl. Sci*. 2022, 4, doi: 10.1007/s42452-022-04996-z.

[257] Chen, T.; Liu, H.; Gao, J.; Hu, G.; Zhao, Y.; Tang, X.; Han, X. Efficient Removal of Methylene Blue by Bio-Based Sodium Alginate/Lignin Composite Hydrogel Beads. *Polymers*, 2022, 14, 2917, doi: 10.3390/polym14142917.

[258] Wang, W.; Bai, H.; Zhao, Y.; Kang, S.; Yi, H.; Zhang, T.; Song, S. Synthesis of Chitosan Cross-Linked 3D Network-Structured Hydrogel for Methylene Blue Removal. *Int. J. Biol. Macromol*., 2019, 141, 98, doi: 10.1016/j.ijbiomac.2019.08.225.

[259] Wang, J.; Meng, X.; Yuan, Z.; Tian, Y.; Bai, Y.; Jin, Z. Acrylated Composite Hydrogel Preparation and Adsorption Kinetics of Methylene Blue. *Molecule*s, 2017, 22, 1824, doi: 10.3390/molecules22111824.

[260] Li, Y.; Liu, L.; Huang, W.; Xie, J.; Song, Z.; Guo, S.; Wang, E. Preparation of Peanut Shell Cellulose Double-Network Hydrogel and its Adsorption Capacity for Methylene Blue. *J. Renew. Mater*., 2023, 11, 3001, doi: 10.32604/jrm.2023.026604.

[261] Godiya, C. B.; Xiao, Y.; Lu, X. Amine Functionalized Sodium Alginate Hydrogel for Efficient and Rapid Removal of Methyl Blue in Water. *Int. J. Biol. Macromol*., 2020, *144*, 671, doi: 10.1016/j.ijbiomac.2019.12.139

[262] Fernández-Pérez, A.; Marbán, G. Visible Light Spectroscopic Analysis of Methylene Blue in Water; What Comes after Dimer? *ACS Omega*, 2020, 5, 29801, doi: 10.1021/acsomega.0c03830.

[263] Li, S.; Liu, X.; Huang, W.; Li, W.; Xia, X.; Yan, S.; Yu, J. Magnetically Assisted Removal and Separation of Cationic Dyes From Aqueous Solution by Magnetic Nanocomposite Hydrogels. *Polym. Adv. Technol.*, 2011, 22, 2439, doi.org/10.1002/pat.1782.

[264] Ludeña, M.A.; Meza, F.d.L.; Huamán, R.I.; Lechuga, A.M.; Valderrama, A.C. Preparation and Characterization of Fe_3O_4/Poly(HEMA-co-IA) Magnetic Hydrogels for Removal of Methylene Blue from Aqueous Solution. *Gels* 2024, 10, 15, doi:10.3390/gels10010015.

[265] Yuan, Z.; Wang, Y.; Han, X.; Chen, D. The Adsorption Behaviors of the Multiple Stimulus-Responsive Poly(Ethylene Glycol)-Based Hydrogels for Removal of RhB Dye. *J. Appl. Polym. Sci.*, 2015, *132*, 1, doi.org/10.1002/app.42244.

[266] Amato, F.; Motta, A.; Giaccari, L.; Di Pasquale, R.; Scaramuzzo, F.A.; Zanoni, R.; Marrani, A.G. One-Pot Carboxyl Enrichment Fosters Water-Dispersibility of Reduced Graphene Oxide: A Combined Experimental and Theoretical Assessment. *Nanoscale Adv*. 2023, 5, 893, doi: 10.1039/D2NA00771A.

[267] Chronopoulou, L.; Di Nitto, A.; Papi, M.; Parolini, O.; Falconi, M.; Teti, G.; Muttini, A.; Lattanzi, W.; Palmieri, V.; Ciasca, G. Biosynthesis and Physico-Chemical Characterization of High Performing Peptide Hydrogels@Graphene Oxide Composites. *Colloids Surf. B Biointerfaces* 2021, 207, 111989, doi:10.1016/j.colsurfb.2021.111989.

[268] Available online: www.sasview.org (accessed on 29 November 2023).

[269] Svergun, D.I. Determination of the Regularization Parameter in Indirect-Transform Methods Using Perceptual Criteria. *J. Appl. Crystallogr*. 1992, 25, 495, doi: 10.1107/S0021889892001663.

[270] Dalalibera, A.; Vilela, P.B.; Vieira, T.; Becegato, V.A.; Paulino, A.T. Removal and Selective Separation of Synthetic Dyes from Water Using a Polyacrylic Acid-Based Hydrogel: Characterization, Isotherm, Kinetic, and Thermodynamic Data. *J. Environ. Chem. Eng*. 2020, 8, 104465, doi:10.1016/j.jece.2020.104465

[271] Li, H.; Cao, X.; Zhang, C.; Yu, Q.; Zhao, Z.; Niu, X.; Sun, X.; Liu, Y.; Ma, L.; Li, Z. Enhanced Adsorptive Removal of Anionic and Cationic Dyes from Single or Mixed Dye Solutions Using MOF PCN-222. *RSC Adv*. 2017, 7, 16273, doi: https://doi.org/10.1039/C7RA01647F.

[272] Sivori, F.; Cavallo, I.; Kovacs, D.; Guembe, M.; Sperduti, I.; Truglio, M.; Pasqua, M.; Prignano, G.; Mastrofrancesco, A.; Toma, L.; et al. Role of Extracellular DNA in Dalbavancin Activity Against Methicillin-Resistant *Staphylococcus aureus* (MRSA) Biofilms in Patients with Skin and Soft Tissue Infections. *Microbiol. Spectr*. 2022, 10, 1, doi: 10.1128/spectrum.00351-22.

[273] Cavallo, I.; Sivori, F.; Truglio, M.; De Maio, F.; Lucantoni, F.; Cardinali, G.; Pontone, M.; Bernardi, T.; Sanguinetti, M.; Capitanio, B. et al. Skin Dysbiosis and Cutibacterium Acnes Biofilm in Inflammatory Acne Lesions of Adolescents. *Sci. Rep*. 2022, 12, 21104, doi: 10.1038/s41598-022-25436-3.

[274] Di Domenico, E.G.; Petroni, G.; Mancini, D.; Geri, A.; Di Palma, L.; Ascenzioni, F. Development of Electroactive and Anaerobic Ammonium-Oxidizing (Anammox) Biofilms From Digestate in Microbial Fuel Cells. *Biomed. Res. Int*. 2015, 2015, 351014, doi: 10.1155/2015/351014.

[275] Di Domenico, E.G.; Cavallo, I.; Sivori, F.; Marchesi, F.; Prignano, G.; Pimpinelli, F.; Sperduti, I.; Pelagalli, L.; Di Salvo, F.; Celesti, I.; et al. Biofilm Production by Carbapenem-Resistant *Klebsiella Pneumoniae* Significantly Increases the Risk of Death in Oncological Patients. *Front. Cell. Infect. Microbiol*. 2020, 10, 561741, doi: 10.3389/fcimb.2020.561741

[276] Ripolles-Avila, C.; Martínez Garcia, M.; Hascoët, A.-S.; Rodriguez-Jerez, J.J. Bactericidal Efficacy of UV Activated TiO_2 Nanoparticles against Gram-Positive and Gram-Negative Bacteria on Suspention, *J. Food*, 2019, 17, 408, doi: 10.1080/19476337.2019.1590461.